The Dissertation Committee for Meghan Jean Bloom Certifies that this is the approved version of the following dissertation:

Characterizing Treatment Induced Alterations of the Tumor Microenvironment Towards Optimizing Therapeutic Regimens in Cancer

Committee:

Thomas E. Yankeelov, Supervisor

Amy Brock

Anna G. Sorace

James W. Tunnell

Jack Virostko

Characterizing Treatment Induced Alterations of the Tumor Microenvironment Towards Optimizing Therapeutic Regimens in Cancer

by

Meghan Jean Bloom

Dissertation

Presented to the Faculty of the Graduate School of

The University of Texas at Austin

in Partial Fulfillment

of the Requirements

for the Degree of

Doctor of Philosophy

The University of Texas at Austin

December 2019

Dedication

To my family who have always told me I could achieve anything I set my mind to.

Acknowledgements

I would like to thank my advisor, Dr. Thomas Yankeelov, who I would not have been able to complete this work without. Throughout my time in this lab, you have always been encouraging, patient and provided me with fundamental guidance. I would like to extend this thanks to Dr. Anna Sorace and Dr. Marcelo Behar, whose mentorship was essential to the success of my projects. The entire Oncology Modeling Group has played a role in the completion of this work and I would like to thank them for their advice and support, particularly my fellow graduate students.

I want to express my gratitude to my family, especially my mother and father, for their unconditional love and encouragement. I am thankful for the support system I was raised in and continue to have as I follow my passions. I could not have accomplished what I have thus far without you.

I would also like to thank my friends, particularly my "Austin Family". All of you have been central to my success during my time at UT. Your continued uplifting words instill me with motivation and determination. Most importantly, I thank you for pulling me away from my lab work for much needed times of distraction.

Finally, I would like to thank the UT system and the biomedical engineering graduate school for providing me the opportunity to pursue this degree.

Abstract

Characterizing Treatment Induced Alterations of the Tumor Microenvironment Towards Optimizing Therapeutic Regimens in Cancer

Meghan Jean Bloom, Ph.D.

The University of Texas at Austin, 2019

Supervisor: Thomas E. Yankeelov

It is well recognized that the tumor microenvironment plays a key role in cancer initiation, progression, and response to treatment. Therapies targeted towards the tumor microenvironment are being introduced in the clinic to be administered alongside chemotherapy and radiation, however, not every patient responds to treatment. The purpose of this dissertation is to characterize modulation of the tumor microenvironment induced by targeted therapies, and build a better understanding of how to exploit these alterations to increase efficacy of developing combination treatments. Our objective is addressed in three parts. First, we quantified temporal alterations in nuclear factor kappa B signaling and downstream gene expression to a small-molecule pathway inhibitor and demonstrated the complexity of altering pathway dynamics for therapeutic gain. Secondly, we characterized changes in innate immune cell infiltration in human epidermal growth factor receptor 2 positive (HER2+) breast cancer after targeted antibody treatment and identified mechanisms of vascular alterations and windows of reduced immune suppression. Lastly, we quantified the effects of radiation and targeted

antibody therapy in HER2+ breast cancer and elucidated a potential to reduce radiation dose in this combination regimen. Collectively, the results presented provide valuable insight of how the tumor microenvironment can dictate treatment response and the potential to modulate the tumor microenvironment to enhance therapeutic efficacy.

Table of Contents

List of Tables

List of Figures

Chapter 1: Introduction

1.1 MOTIVATION

In 2000, Hanahan and Weinberg identified six characteristics that defined a cell as cancerous. The underlying focus of these characteristics was that cancer is a genetic disease and the instability of the genome of the cancer cell leads to tumor progression [1]. In addition to genomic instability, scientists now recognize that the tumor microenvironment plays a critical role in cancer initiation, progression, and response to treatment [2–4]. Three crucial aspects of the tumor microenvironment modulating tumorigenesis are molecular cytokines that activate survival signaling networks, chronic angiogenesis, and tumor promoting inflammation [2].

Growth factors promoting cell proliferation are produced in normal tissues to maintain homeostasis and ensure proper cell turnover. Cancer cells can develop the ability to sustain proliferative signaling by deregulating signaling pathways and resisting apoptosis [5]. Tumors also promote chronic angiogenesis, a process largely quiescent in normal tissues. The development of new vasculature provides nutrients necessary for tumor growth. Additionally, much of this vasculature is irregular leading to areas of hypoxia which reduces tumor response to treatment [6, 7]. Thirdly, inflammation by innate immune cells can promote tumor escape by secreting cytokines that increase cancer cell proliferation and angiogenesis. Inflammatory cells also have the ability to suppress adaptive immune responses and assist in cancer immune evasion [8–10]. Efforts to combat tumor promoting factors in the microenvironment include small molecule pathway inhibitors to inhibit cancer cell proliferative signaling, anti-angiogenic therapies to reduce tumor angiogenesis, and immunotherapies aimed to strengthen a patient's immune system to attack cancer cells and evade immunosuppression [11–15].

While an increasing number of therapies targeting the tumor microenvironment are being introduced in the clinic, not every patient responds to such treatment. There have been recent efforts to better understand the tumor microenvironment and manipulate it to decrease metastatic potential and favor tumor regression [3, 16]. The overall goal of this dissertation is to quantify treatment-induced temporal changes of the tumor microenvironment to provide insight for optimizing clinical combination treatment regimens in cancer. We accomplished this goal in the three areas described below.

1.2 OBJECTIVES

1.2.1 Aim 1: Quantify temporal changes in NF-κB signaling and downstream gene expression

Small molecule approaches targeting the nuclear factor kappa B (NF-kB) pathway, a regulator of inflammation, have thus far proven unsuccessful in the clinic in part due to the complex pleiotropic nature of this network [17–19]. Downstream effects depend on multiple factors including stimulus-specific temporal patterns of NF-kB activity [17, 20]. Despite considerable advances, genome-level impact of changes in temporal NF-kB activity caused by inhibitors and their stimulus dependency remains unexplored. Temporal nuclear translocation of NF-κB was quantified from immunofluorescent images of 3T3 fibroblasts stimulated with interleukin 1 beta (IL-1β) and tumor necrosis factor alpha (TNF-α) when treated with 10-100 μM of SC-514 (inhibitor kappa B subunit beta (IKKβ) inhibitor, IC_{50} 3-12 μM). Inflammatory genes of interest were evaluated for differences in gene expression between experimental conditions through RNA TagSeq. In this section, the effects of selective perturbation on NF-κB transcriptional dynamics applicable for developing NF-κB pathway targeted drugs were evaluated.

1.2.2 Aim 2: Identify temporal changes in myeloid cell infiltration in HER2+ breast cancer

Therapy targeted to the human epidermal growth factor receptor 2 (HER2) is used in combination with cytotoxic therapy in the clinical treatment of HER2+ breast cancer. Trastuzumab, an anti-HER2 therapy, has been shown to induce vascular changes that can increase delivery of chemotherapy [21, 22]. To quantify the role of immune modulation in treatment-induced vascular changes, this aim identifies temporal changes in myeloid cell infiltration with corresponding vascular alterations in a preclinical model of HER2+ breast cancer following trastuzumab therapy. Alterations in myeloid cell types were evaluated by immunophenotyping using flow cytometry. Immunohistochemistry staining validated tumor vascular alterations coinciding with immune alterations. Additionally, inflammatory cytokine and chemokine differences were evaluated between control and treated tumors to elucidate mechanisms of immune response. This section reveals mechanistic properties of improved tumor vascularization and potential windows of reduced immune suppression in trastuzumab treated HER2+ breast cancer tumors.

1.2.3 Aim 3: Quantify the effects of combination trastuzumab and radiation therapy longitudinally in HER2+ breast cancer

Radiation is used in combination with trastuzumab as an adjuvant therapy to eliminate residual cancer cells that may be remaining in the breast tissue or chest wall [23, 24]. The use of adjuvant radiation reduces the risk of cancer returning, however; patients with HER2+ breast cancer are more likely to have a recurrence than HER2- patients [25, 26]. Studies show HER2 signaling can modulate resistance to radiation treatment, and trastuzumab may act as a radiosensitizer [27–31]. To determine if trastuzumab sensitizes breast cancer cells to radiation, treatment effects were quantified in BT474, SKBR3, and MDA-MB-231 cell lines using measurements of cell proliferation

through *in vitro* time-resolved microscopy. Furthermore, this aim shows tumor response to combination treatment in an *in vivo* mouse model of HER2+ breast cancer and reveals potential tumor microenvironmental alterations affecting tumor response.

1.3 ORGANIZATION

The remainder of this dissertation is organized as follows. In Chapter 2, the background necessary to understand the clinical significance of this work is discussed. Chapter 3 quantifies stimulus specific responses of NF-κB signal dynamics to targeted small molecule therapy and alterations in gene expression. This chapter demonstrates small molecule inhibitors acting on pathway components can alter signal dynamics in a stimulus-dependent manner and affect gene response in complex ways. Chapter 4 shows innate immune alterations in HER2+ breast cancer tumors after treatment with anti-HER2 therapy. This chapter shows correlations between immune modulation and vascular changes in HER2+ breast cancer and the potential for anti-HER2 therapy to modulate immunosuppressive components of the tumor microenvironment. Chapter 5 shows *in vitro* combination trastuzumab and radiation effects are additive, however, *in vivo* combination treatment enhances the rate of tumor regression. This chapter shows the potential of using a lesser dose of radiation when administering trastuzumab in a combination regimen. Chapters 3-5 each contain the respective study's motivations, methods, results and limitations. Finally, Chapter 6 summarizes the impact of this work and future directions.

Chapter 2: Background

2.1 NF-κB

2.1.1 NF-κB Signaling Pathway

Nuclear factor kappa B (NF-κB) is an inducible transcription factor represented by a family of five proteins—RelA (p65), RelB, c-Rel, NF-κB1 (p105/50) and NF-κB2 (p100/52). These five proteins form homo- and heterodimers that play a role in the regulation of multiple biological processes including cell proliferation, differentiation and survival [32]. The p50:p65 heterodimer is the most prevalent NF-κB dimer among cell types and widely studied in the context of pathway function and regulation in disease [32–35]. Activation of NF-κB occurs through two separate signaling pathways, canonical (classical) and non-canonical (alternative) [36]; however, recent studies provide evidence of cross-talk between the two [37, 38]. The non-canonical pathway is activated through the engagement of a small subset of tumor necrosis factor receptors and plays a role in lymphoid organogenesis and B cell maturation and survival [39]. The canonical NF-κB signaling pathway has been studied in greater detail and is activated through engagement of numerous cytokine receptors, tumor necrosis factor receptors, pattern-recognition receptors and the B and T cell receptor [32, 39]. Misregulation of both the canonical and non-canonical NF-κB pathways play a role in cancer progression [18, 34, 40].

NF-κB is held inactive in cells through inhibitor kappa B proteins (IκBs). Upon activation, a series of phosphorylation events occur, releasing NF-κB to the nucleus where gene transcription takes place [36]. An essential regulator of NF-κB nuclear translocation is the inhibitory IκB kinase (IKK) complex which consists of three subunits, IKKα, IKKβ and IKKγ [36, 41]. The IKK complex is responsible for the phosphorylation of the specific inhibitory protein sequestering NF-κB in the cytoplasm, IκBα [41]. In the

nucleus, NF-κB drives the expression of IκBα, creating one mechanism of negative feedback [42, 43]. A diverse range of stimuli activate IKK including inflammatory cytokines, growth factors, microbial pathogens and cellular stress [44]. Many of the stimuli that activate NF-κB are present in the tumor microenvironment including tumor necrosis factor alpha (TNF-α) and interleukin 1 beta (IL-1β) [45, 46].

2.1.2 NF-κB in Cancer

With NF-kB being a key modulator in cell survival and inflammation, loss of proper regulation can directly contribute to several of the hallmarks of cancer described by Hanahan and Weinberg including sustaining proliferative signaling, tumor-promoting inflammation, and avoiding immune destruction [1, 34, 47]. Regulatory feedback mechanisms are crucial for proper NF-κB control and maintaining biological homeostasis. In cancer cells, NF-κB can become constitutively activated and promote tumorigenesis. In human breast cancer specimens, activated NF-kB was found in over 80% of HER2+ samples [48]. In a preclinical human xenograft model of colorectal cancer, Sakamoto *et al.* found evidence of constitutive NF-κB activation in 40% of tissue samples [49]. Loss of negative feedback has been shown to occur through genetic mutations in the NF- κB pathway. For example, Bredel *et al.* found deletions of at least one copy of the inhibitor protein IκBα in 24.2% of glioblastoma patient samples (N = 219) [50]. Several studies show frequent mutations in IκBα in malignant cells in Hodgkin's lymphoma, where upregulation of NF- κB is consistently observed [51–53].

Chronic NF-κB activation promotes cell proliferation and prevents apoptosis, driving cancer cells towards metastasis. For example, NF-κB upregulation has been linked with increased cell proliferation and metastatic potential in hormone receptor negative (estrogen and progesterone) cell lines [54, 55]. NF- κB encodes for many genes

that suppress apoptotic responses including the inhibitor of apoptosis (IAP) protein, c-IAP2 [56]. c-IAP2 prevents apoptosis induced by effector caspases [57]. Furthermore, NF-κB activity in cancer cells can lead to chemotherapy and radiation resistance, partly through the encoding of the multidrug resistance protein 1 [58–60].

2.1.3 NF-κB as a Therapeutic Target

NF-κB has been explored as a therapeutic target in cancer for many years [61–63]. Inhibiting NF-κB activation in cancer cells to enhance tumor regression in preclinical studies shows promising results. Two preclinical mouse models of breast cancer treated with an NF-κB inhibitor had greater decrease in tumor size over two months than control tumors [64]. There is also evidence targeting NF- κB could improve therapeutic response to chemotherapy. *In vitro*, NF-κB inhibition enhanced the cytotoxicity of doxorubicin by increasing apoptosis of osteosarcoma cancer cell [65]. However, no therapies directly targeted to the NF-κB pathway have successfully made it to the clinic.

NF-κB activation is not only present in cancer cells but also in innate and adaptive immune cells present in the tumor microenvironment. Although NF-κB promotes tumor escape when activated in cancer cells, it can promote anti-tumor immunity by stimulating T cell activation [66, 67]. In a preclinical mouse model, impairment of NF-κB activation led to decrease in CD8+ (cytotoxic) T cell response to pathogens [68]. Another study showed mice with inhibited NF-κB signaling downstream of the T cell receptor (murine fibrosarcoma) were unable to reject tumors compared to mice with functioning NF-κB signaling pathways [40]. On the contrary, NF-κB activation has been shown to promote macrophage polarization towards an immunosuppressive phenotype and inhibiting NF-κB pathway function in macrophages promotes tumor regression [69, 70]. NF-κB can

have conflicting roles in cancer progression depending on the cell of interest, therefore defining a target cell phenotype is an important consideration when developing NF-κB pathway inhibitors.

2.2 HER2+ Breast Cancer

2.2.1 HER2

Human epidermal growth factor receptor 2 positive (HER2+) breast cancer is characterized by overexpression of the HER2/neu receptor [71]. HER2 is a transmembrane receptor tyrosine kinase that normally is expressed on epithelial cells in the breast, but when overexpressed in breast cancer cells, HER2 drives proliferation and survival [72, 73]. HER2 is part of the epidermal growth factor receptor family which includes three other HER receptors (HER1, HER3, and HER4). HER2 signaling is activated through dimerization with one of the other ligand bound HER family members. Upon dimerization, pro-survival signaling pathways are activated including phosphoinositide-3-kinase/protein kinase B/mammalian target of rapamycin (PI3K/Akt/mTOR) and Ras/Raf/mitogen-activated protein kinase (MAPK) pathways [74, 75]. HER2 overexpression appears in 15-20% of breast cancer cases [71]. Patients with HER2+ status have a three times higher risk of recurrence and five times higher risk of metastasis than HER2- patients [26, 76]. Metastasis to the brain, a particularly difficult site to treat, is also more likely in HER2+ patients [77, 78]. Furthermore, less than half of patients achieve a pathological complete response in the neoadjuvant setting [79, 80].

2.2.2 Targeting HER2 in the Clinic

Several targeted therapies are FDA approved for use in the clinic in combination with cytotoxic therapy to mediate the effects of HER2 overexpression in breast cancer

cells. Lapatinib (trade name Tykerb, Novartis, Basal, Switzerland) was the first receptor tyrosine kinase inhibitor approved for the treatment of HER2+ breast cancer in 2007 [81]. It is a small molecular therapy that targets both the epidermal growth factor receptor and HER2 tyrosine kinase domains [11]. Trastuzumab (trade name Herceptin, Genentech, South San Francisco, CA) is a humanized monoclonal antibody targeted against the extracellular domain IV of HER2. It inhibits downstream signaling reducing cell growth, promotes HER2 internalization and degradation, and attracts immune cells to tumors through antibody-dependent cellular cytotoxicity [23, 82, 83]. Pertuzumab (trade name Perjeta, Genentech, South San Francisco, CA) is also a humanized monoclonal antibody targeted to HER2, but binds to the extracellular domain II of HER2. Pertuzumab prevents downstream signaling by preventing HER2 dimerization [84]. Ado-trastuzumab emtansine (T-DM1) (trade name Kadcyla, Genentech, South San Francisco, CA) is an antibody-drug conjugate approved for use in patients that have previously been treated with trastuzumab and chemotherapy and have either metastatic or residual disease [85]. It consists of trastuzumab conjugated to a derivative of mertansine, which is a cytotoxic anti-microtubule agent. After T-DM1 binds to HER2, the receptor and T-DM1 are endocytosed and the cytotoxic agent causes cell cycle arrest and apoptosis [86].

Trastuzumab, in addition to chemotherapy, is the first line of targeted treatment used in the clinic, although, depending on the stage at diagnosis and previous treatment received, other treatment plans may be used. Adding pertuzumab to trastuzumab and chemotherapy improved overall survival among patients with unresectable metastatic disease and when used in combination with trastuzumab in the adjuvant setting [87, 88]. In patients who received neoadjuvant chemotherapy with trastuzumab and had residual invasive disease after surgery, adjuvant T-DM1 significantly lowered the risk of recurrence compared to trastuzumab [89]. Lapatinib (as well as other tyrosine kinase

inhibitors [90]) is approved for treatment of metastatic HER2+ breast cancer. It does not perform superior than trastuzumab in the clinic, but it can cross the blood brain barrier and can be a part of combination treatment for patients with brain metastasis [91, 92] .

2.3 TUMOR INFILTRATING MYELOID CELLS

2.3.1 Types and Functions

Myeloid cells are a subset of leukocytes derived from hematopoietic stem cells in the bone marrow that are a part of the innate immune system [93, 94]. Subsets of myeloid cells include macrophages and dendritic cells and monocyte derived suppressor cells (MDSCs). Myeloid cells circulate through the body and are recruited when tissue is damaged or a foreign substance is present [95]. They can also home to tissues where they control cell turnover and maintain tissue homeostasis [96]. Myeloid cells are crucial in signaling T cells and promoting immune responses [97, 98].

When dendritic cells are activated, they are primarily an antigen presenting cell. They phagocytose antigens, digest them into peptides and generate MHC molecules to present peptides to T cells, stimulating an adaptive immune response [98, 99]. Macrophages can also phagocytose foreign substances and present antigens to T cells [100]. Macrophages can broadly be categorized into two types, M1 and M2, and can switch between these two phenotypes *in vivo* [101]. MDSCs are a heterogeneous group of immature myeloid cells which can have two phenotypes, granulocytic MDSCs (G-MDSCs) and monocytic MDSCs (M-MDSC).

2.3.2 Role in the Tumor Microenvironment

Myeloid cells in the tumor microenvironment greatly influence tumor progression and tumor response to treatment due to their critical involvement in angiogenic and

inflammatory responses [8–10]. M1 macrophages secrete pro-inflammatory cytokines and have a high antigen presentation ability which promotes T cell activation and anti-tumor responses. M1 macrophages also have been shown to stabilize tumor vasculature [102–104]. Alternatively, M2 macrophages promote immunosuppression through the secretion of interleukin 4, 10 and 13. They induce angiogenesis through secretion of VEGF and several matrix metalloproteinases and have less antigen presentation ability than M1 macrophages [103, 105]. As solid tumors progress, macrophages are often skewed toward an M2 phenotype which promotes angiogenesis and immunosuppression leading to tumor escape [102]. Like M2 macrophages, MDSC's secrete cytokines that inhibit anti-tumor immunity and promote tumor angiogenesis [106]. MDSCs can also down-regulate L-selectin on T cells; a key molecule that allows them to home to sites of damage or infection [107, 108]. Dendritic cells can enhance T cell responses to tumor cells, but only when they acquire a mature phenotype. Immature dendritic cells promote vascularization through proangiogenic cytokines such as VEGF and IL-8 [109]. Additionally, dendritic cell maturation can be prevented by immunosuppressive cytokines secreted from M2 macrophages or MDSC's [110].

2.3.3 Targeting Myeloid Cells

Increasing evidence of myeloid cell modulation of cancer progression has led to efforts in developing myeloid targeted therapies. Drug development has been focused both in modulating the type of myeloid cell in the tumor microenvironment and in enhancing myeloid antigen presentation ability. Therapies to deplete TAM density or limit recruitment in cancers where TAM density is negatively correlated with tumor regression have had preclinical success [10]. Macrophage colony stimulating factor 1 (CSF-1) is a primary regulator of macrophage differentiation and survival [111]. In a

xenograft mouse model of breast cancer, Aharinejad *et al.* showed that blocking CSF-1 reduced macrophage infiltration and tumor burden [112]. However, therapies depleting macrophage tumor infiltration have not been successful in the clinic [113, 114]. One challenge with this type of therapy is targeting macrophages only in the tumor and not depleting them systemically [10]. Alternatively, strategies are being developed to skew macrophage polarization to an M1 phenotype in the tumor microenvironment or inhibit the function of immunosuppressive M2 macrophages [115–117].

Dendritic cell immunotherapy is another emerging treatment candidate. Granulocyte macrophage colony stimulating factor (GM-CSF) is a cytokine that can increase dendritic cell differentiation and activation [118, 119]. GVAX (originally developed at the Whitehead Institute of Biomedical Research) is a vaccine used to genetically modify pancreatic cancer cells to produce GM-CSF aimed in enhancing dendritic cell maturation [120]. Current clinical trials are being conducted using GVAX as a combination immunotherapy in pancreatic cancer at Johns Hopkins University / Sidney Kimmel Cancer Center [121]. Sipuleucel-T (trade name Provenge, Dendreon Pharmaceuticals, Seal Beach, CA) was approved for the treatment of metastatic prostate cancer in 2010 [122]. This therapy extracts immature dendritic cells from the patient, incubates them with GM-CSF and fragments of a prostate specific enzyme called prostatic acid phosphatase. Dendritic cells then mature *in vitro*, away from an immunosuppressive tumor microenvironment, and are re-administered into the patient [122, 123]. DC-Vax (Northwest Biotherapeutics, Bethesda, MD) is another autologous cell therapy used to stimulate dendritic cells *in vitro* and is currently in clinical trials to assess efficacy in brain, ovarian, prostate and multiple other solid tumor cancers [124].

2.4 Radiation Therapy in HER2+ Breast Cancer

2.4.1 Radiation in the Clinic

Radiation therapy is given to breast cancer patients after a lumpectomy (surgery that removes the tumor while sparing healthy breast tissue) or mastectomy (surgery that removes the tumor and surrounding breast tissue). Almost all patients receive adjuvant radiation therapy regardless of the type of surgery they receive unless patients present with a low risk tumor (size < 2 cm and node negative) [24]. Radiation therapy is used to destroy any cancer cells that may be left in the breast tissue or chest wall after surgery and reduce the risk of locoregional recurrence. In the adjuvant setting, radiation is typically given in 2 Gy fractions, 5 days a week for about 5 weeks. Trastuzumab is administered every 3 weeks concurrently with radiation and can continue for up to a year [125]. There are recent investigations evaluating if radiation is needed to reduce recurrence in HER2+ patients, however, it is still currently used in the standard of care [126]. Clinical studies show recurrence in 5-15% of patients who receive radiation after surgery, and increase in risk is associated with tumor stage and HER2+ status [25, 26, 127].

2.4.2 Resistance and HER2

Ionizing radiation causes DNA damage through both indirect and direct effects. Direct effects are single or double-stranded breaks in cancer cell DNA caused by radiation therapy. Radiation causes indirect effects by breaking water molecules into fragments with unpaired electrons, called free radicals, which are highly reactive and can induce DNA damage [128]. The damage to DNA from radiation through either of these mechanisms can interfere with the ability of cells to properly replicate, and therefore, survive [128, 129]. The ability for cancer cells to survive radiation induced damage

depends largely on the induction of DNA repair signaling pathways. HER2+ breast cancer is reported to have an increased resistance to radiation treatment and studies show that pathways upregulated by HER2 ligand engagement can play a role in resistance [23, 27, 29]. The PI3K/Akt/mTOR, activated through ligand engagement of HER2, controls regulation of genes responsible for DNA repair mechanisms such as Fanconi anemia group D2 protein (FANDCD2) and ribonucleotide reductase (RNR) [130, 131]. PI3K/Akt/mTOR pathway transduction also activates NF-κB which transcribes for genes including cyclin B1 and cyclin D1 that regulate DNA repair mechanisms to radiation therapy [29, 58, 132]. Although evidence supports PI3K/Akt/mTOR contributing to radiation resistance in HER2+ breast cancer, determining how to target this pathway to increase efficacy of radiation therapy remains an open area of investigation [129].

Chapter 3: The Effects of IKK-beta Inhibition on Early NF-kappa-B Activation and Transcription of Downstream Genes[1]

3.1 INTRODUCTION

Nuclear factor kappa B (NF-κB) plays a key role in coordinating inflammatory responses through the regulation of genes, such as CXCL10, CCL5, and IL6, encoding pro-inflammatory cytokines, chemokines and growth factors [133–135]. Chronic inflammation promotes tumorigenesis by increasing cellular stress and DNA damage [2], and the appropriate regulation and control of NF-κB activity has long been considered a promising avenue for treating inflammatory diseases and cancer. Efforts in developing NF-κB pathway specific therapies have been largely unsuccessful due to its simultaneous influence in a vast number of physiological functions [17–19].

NF-κB is activated by a variety of extracellular stimuli including interleukin 1 beta (IL-1β) and tumor necrosis factor alpha (TNF-α), both playing roles in tumor progression and inflammation [45, 46, 136]. In resting cells, NF-κB is maintained in the cytoplasm by inhibitory kappa B (IkB) proteins [36, 137]. Upon stimulation, IκBs are phosphorylated by the IκB kinase complex (IKK), which causes its rapid degradation and releases NF-κB for nuclear translocation and subsequent control of gene transcription. IkB subunit beta (IKKβ) is one of the three kinases in IKK which is a convergence point for many NF-κB signaling pathways [36, 41]. Alterations of NF-kB signaling dynamics has been demonstrated as a function of inhibiting IKK action [138–

[1]Portions of this chapter were previously published in a peer-reviewed journal: Bloom MJ, Saksena SD, Swain GP, Behar MS, Yankeelov TE, Sorace AG. The effects of IKK-β inhibition on early NF- κB activation and transcription of downstream genes. Cellular Signalling. 2018. Bloom MJ designed and performed experiments, analyzed data, and wrote the publication.

141]. Additionally, dynamical changes of NF-κB activation have been shown to result in altered gene expression profiles [134, 138, 142]. However, the extent to which pathway perturbations effect signal dynamics and the relationship between NF-κB signaling dynamics and transcriptional output have not been fully elucidated.

In this contribution, we test the hypotheses that 1) inhibitors acting on pleiotropic pathway components can have stimulus-specific effects on signal dynamics, and 2) alterations in signal dynamics caused by small molecule inhibitors affect downstream gene transcription. To this end, we treated 3T3 fibroblasts with SC-514, an IKKβ selective inhibitor, and characterized changes in the temporal profile of NF-κB activity and corresponding gene expression in response to TNF-α or IL-1β stimulation. Taken together, the results in this study demonstrate the value of protein-specific small molecule inhibitors as tools for probing signaling pathways, and also highlight their potential for altering signal dynamics affecting gene expression as a result.

3.2 Materials and Methods

3.2.1 Cell Culture

3T3 mouse fibroblast cells were a gift from Dr. Laura Suggs (Department of Biomedical Engineering, University of Texas, Austin, TX) and were maintained in glucose-containing Dulbecco's modified Eagle's medium (DMEM, VWR International, LLC, Radnor, PA) supplemented with 10% bovine calf serum and penicillin-streptomycin (100 units/ml). One day before the stimulation experiments, cells were seeded in 8-well chambered cover glass (Cellvis, Mountain View, CA) in 200 μl of culture medium at an estimated 35,000 cells/well. Cell count was determined by the Countess II FL automated cell counter (Thermo Fisher Scientific Inc., Waltham, MA).

3.2.2 Stimulation Experiments

3T3 fibroblasts in each 8-well chamber were pretreated with culture medium containing SC-514 (0, 10, 25, 50 or 100 μM) (Selleck Chemicals, Houston, TX) 1 hour prior to stimulation. SC-514 is a selective inhibitor of IKKβ action, inhibiting IkBα phosphorylation (when treated with SC-514 above 100 μM, cell dissociation occurred). Cells were stimulated with either 1 ng/ml of IL-1β, 10 ng/ml of TNF-α, or control saline for 5, 10, 15, 20, 25, 30, 45, 60, 75, or 90 min. An initial dose response experiment for each stimuli was conducted. The lowest concentration of stimuli that achieved the fastest rate of peak NF-κB activation was chosen for each stimuli. Cells were fixed and permeabilized with 100% methanol at -20 °C for 5 min and blocked in phosphate buffered saline (PBS, Caisson Laboratories, Inc., Smithfield, UT) + 2% bovine serum albumin (BSA, Fisher Scientific International Inc., Pittsburgh, PA) for 1 hour. Cells were incubated with NF-kB-p65 antibody Alexa Fluor 488 (AF488) conjugate (Cell Signaling Technology, Beverly, MA) in PBS+2% BSA for 1 hour followed by a 5-min incubation with 4',6-diamidino-2-phenylindole (DAPI) in PBS. This experiment was replicated for each drug treatment four times at each time point. A simplified diagram of the NF-kB signaling pathway can be seen in Figure 3.1. NF-kB is activated by both IL-1β and TNF-α**.** When IL-1β and TNF-α bind to their receptors, (IL-1R and TNF-R, respectively), a series of phosphorylation events take place, eventually converging at the IKK complex which consists of three isoforms; IKKα, IKKγ, and IKKβ (Figure 3.1a). IKKβ phosphorylates an inhibitory protein IkBα, subsequently allowing NF-kB to translocate to the nucleus where gene transcription takes place (Figure 3.1b). NF-kB translocates back into the cytoplasm (Figure 3.1c) due to negative feedback in signaling.

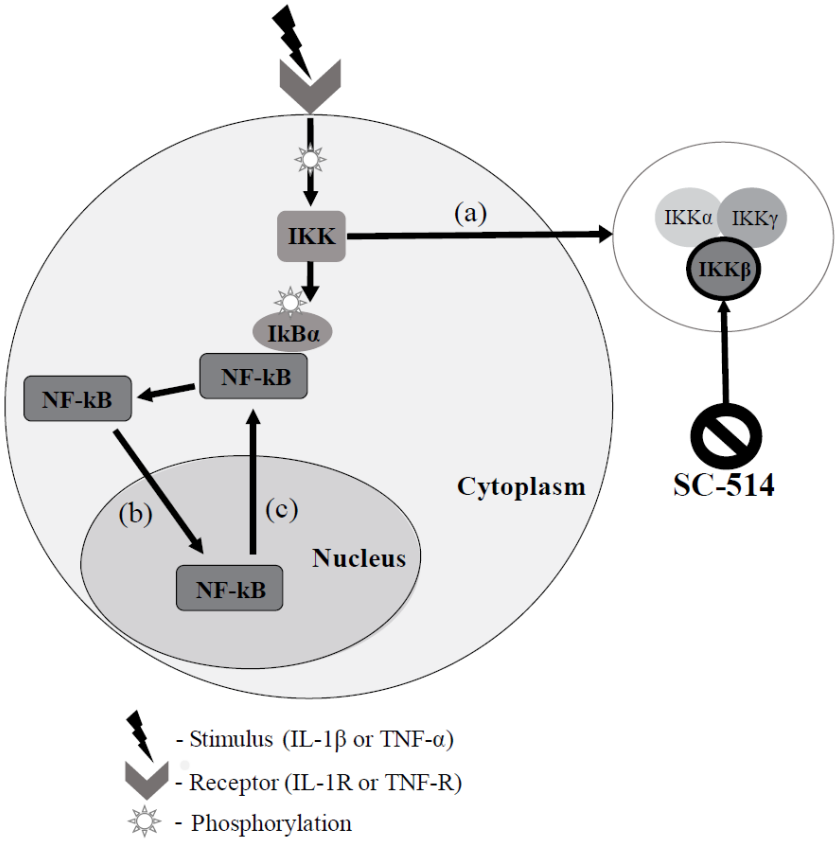

Figure 3.1: High level representation of the NF-κB signaling pathway and SC-514 mechanism of action. Stimuli IL-1β and TNF-α bind IL-1R and TNF-R, respectively, triggering downstream phosphorylation. NF-κB is sequestered in the cytoplasm by IkBα until activation of the IKK complex, which consists of three isoforms, IKKα, IKKγ, and IKKβ a). IKKβ phosphorylates IkBα, allowing NF-κB to translocate to the nucleus for gene transcription b) until eventually translocating back to the cytoplasm c). SC-514 is a selective inhibitor of IKKβ action.

3.2.3 Microscopy and Image Analysis

Cells were imaged in the green fluorescent protein (GFP) (Ex. 450-49 nm Em. 500-550 nm) and DAPI (Ex. 325-375 nm Em. 435-485 nm) channels with the Leica DMI6000 microscope (Leica Microsystems, Wetzlar, Germany) at 20X resolution. Image

analysis was performed using CellProfiler (www.cellprofiler.org). An image analysis pipeline was constructed to measure DAPI-labeled nuclei and AF488-labeled NF-kB. Specifically, raw images were first corrected for uneven illumination (vignetting) [143–145]. An illumination function was calculated using the intensity of each pixel (regular) and convex hull smoothing method of an empty field image was applied. Each image was divided with this illumination function and then background intensity was subtracted. All images were converted to grayscale. Nuclei were identified with the DAPI stain using Otsu two-class global thresholds. 'Shape' which identifies indentations on edges of touching cells was used to distinguish the number of objects in a clump. Cell boundaries were drawn using AF488-labeled NF-kB intensity, where boundaries are defined to be the dimmest points between two objects [143, 145]. The nucleus was masked from the whole cell to define the cytoplasm region. Intensity of AF488-labeled NF-kB was measured in the nucleus, cytoplasm, and whole cell. Each image was analyzed independently. Two 4.19 megapixel images were taken per well in each experiment with ~100-200 cells in view in each image. Mean fluorescent intensity was calculated for each cell and averaged together for each well. Values were normalized to the averaged time zero intensity. Images where cell boundaries could not be accurately distinguished were eliminated from analysis.

3.2.4 RNA Sample Preparation

24 hours before RNA purification, 3T3 fibroblasts were plated in a 24 well plate at 140,000 cells/well. Cells were pretreated with culture medium containing SC-514 (0, 10, 25, 50 or 100 μM) 1 hour prior to stimulation. Cells were stimulated with either 1 ng/ml of IL-1β, or 10 ng/ml of TNF-α for 15, 30, 60, 120, and 360 min. All reagents for RNA purification were part of the RNeasy Mini kit (Quiagen, Hilden, Germany). Briefly,

cells were lysed directly in the 24 well plate and homogenized by vortexing. Precipitate was formed using 70% ethanol. All samples were treated with DNase and eluted into 30 µl of RNase free water. RNA concentration and purity was determined using the Qubit 4 Fluorometer (Thermo Fisher Scientific Inc., Waltham, MA). This process was replicated for each drug treatment at each time point four times.

3.2.5 TagSeq Profiling

RNA TagSeq is a 3' Tag-based approach to full RNA sequencing that has been proven highly reliable for differential gene expression analysis in well annotated genomes [146, 147]. RNA samples were sent to the Genome Sequence and Analysis Facility at The University of Texas at Austin where libraries were constructed using a modified protocol from Lohman *et al*. [146]. Modifications from Lohman *et al*. included: i) Fragmentation of RNA was done using 5X First Strand Buffer (Takara Bio USA, Inc., Mountain View, CA) for 2.5 min ii) Titanium tag polymerase (Takara Bio USA, Inc., Mountain View, CA) was used in cDNA amplification master mix. Samples were sequenced with the Illumina HiSeq 2500 1 × 100 with an average of 3.5 x 10^6 raw reads per sample.

3.2.6 TagSeq Processing

TagSeq clipping was carried out using FASTX-Toolkit's *fastx-clipper* with parameters to remove non-template bases introduced by reverse transcriptase on the 5' end [147, 148]. Quality assurance of processed reads was done using dispersion calculations implemented in *DESeq2*. Poor quality reads due to low amounts of sample (yield < 10 Mbp) for sequencing were removed from analyses (n = 2). Reads were aligned against an assembly of cDNA sequences for the GRCm38 (mm10) assembly

genome using Bowtie2 [149]. The output of processing was a count matrix of raw reads per gene for each experimental condition.

3.2.7 Differential Gene Expression Analysis

Differential expression analyses were carried out via *DESeq2* from the Bioconductor suite of R tools [150] using count matrices generated from the processing pipeline. Normalization of reads was done by modeling read counts for each sample as following a negative binomial distribution with a mean that is proportional to the concentration of cDNA fragments from each gene scaled by a factor based on sequencing depth and library size. Expression differences were calculated by comparing coefficients in a generalized linear model (GLM) between experimental conditions. The GLM returns a coefficient matrix indicating overall expression strength of all genes in the sample and the shrunken (minimized dispersion) $\log_2$ fold change between two experimental conditions. Expression at each inhibitor concentration (25, 50, and 100 μM) for both IL-1β and TNF-α at each longitudinal time point was individually compared against the no inhibitor condition at that same time point. All code for this portion of the analysis, including visualization of results, was written in *R* statistical software [151].3.2.8 Technical Validation

3.2.7.1 RNA Sample and Sequencing

Quality assurance of all RNA samples was performed with the Qubit 4 Fluorometer (Thermo Fisher Scientific Inc., Waltham, MA) to ensure high quality (RNA IQ > 9). After library preparation, select samples were again assessed to ensure high quality using the RNA integrity number (RIN > 7) with the Bioanalyzer 2100 (Agilent, Santa Clara, CA) and that every sample was an adequate concentration. Quality

evaluation of sequence reads was performed with a FastQC report24 (MultiQC version 1.7). All samples had a Phred quality score above 30 across all bases up to 90 bp. At the end of the read (90-100 bp) where samples are known to be of lesser quality, all samples remained above 25 (Figure 3.2a). No median reached below 25 for a base and no lower quartile for any base was less than 10. The most frequently observed mean of per sequence quality scores was higher than 27 which equates to <0.2% error rate (Figure 3.2b). Two samples yielded <10 Mbp and were recommended to be removed from analyses (n = 2). See Usage Notes for sample information.

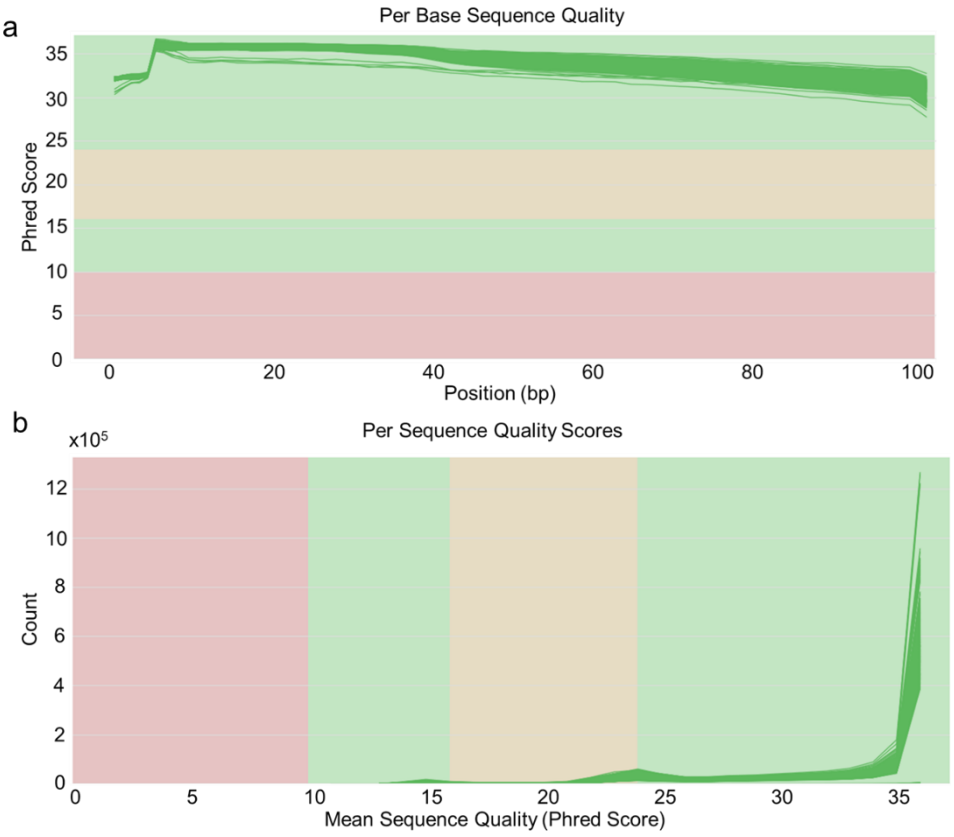

Figure 3.2: Quality assessment of sequencing data. A) Per base sequence quality scores across all samples. All scores remain above 25 for the entirety of the read. b) Per sequence quality scores across all samples. The most frequently observed mean quality was above 27.

3.2.7.2 Validation Across Replicates

Each experimental condition had four biological replicates, enabling statistical evaluation to test if the data was robust to technical errors. Principal component analysis (PCA) was applied to the log-transformed gene expression space (Figure 3.3a and 3.3b). Clusters based on biological replicate are indicated by color. Two samples which were of poor quality due to experimental error are indicated with red arrows. Silhouette analysis [152] was conducted using the Euclidean distance between points within a given condition to validate consistency within the cluster. To calculate the silhouette of a point i, $s(i)$ that lies within a cluster A, let the "within" dissimilarity metric $a(i)$ be defined as:

(1) $$a(i) = \text{average Euclidean distance of point } i \text{ to all other points in cluster } A$$

Let C be a set of all other clusters and the "between" dissimilarity metrics for point i, $d(i, C)$ be defined as:

(2) $$d(i, C) = \text{average Euclidean distance of point } i \text{ to all points in set of clusters } \mathbf{C}$$

Let $\boldsymbol{b(i)}$ represent the closest neighboring cluster where:

(3) $$b(i) = \min_{C \neq A} d(i, C)$$

The silhouette measurement, $\boldsymbol{s(i)}$ is the output of the following piecewise function:

$$(4) \qquad s(i) = \begin{cases} 1 - \dfrac{a(i)}{b(i)} & \text{if } a(i) < b(i) \\ 0 & \text{if } a(i) = b(i) \\ \dfrac{b(i)}{a(i)} - 1 & \text{if } a(i) > b(i) \end{cases}$$

Each silhouette measurement is a value between -1 and 1, where a value of 1 indicates that a given point is well defined in the current cluster. A value of 0 indicates it is equally likely to be within its current cluster and its neighbor, and a value of -1 indicates it is better classified in the neighboring cluster [152]. In our analysis, each cluster is given an average score of the silhouette measurement of all four biological replicates within the cluster. Two clusters stimulated with IL-1β resulted in negative average silhouette values (Figure 3.3a). See Table 3.1 for average silhouette values of the IL-1β stimulated condition. Three clusters stimulated with TNF-α resulted in negative average silhouette values (Figure 3.3b). See Table 3.2 for the average silhouette values of the TNF-α stimulated samples.

Sample	SC-514 Inhibitor Concentration (μM)	Time Stimulated (min)	Silhouette Value
A	0	0	0.658447206
B	0	15	-0.19131602
C	0	30	0.78628854
D	0	60	0.57103218
E	0	120	0.800524596
F	0	360	0.749030771
G	25	15	0.796277169
H	25	30	0.647351099
I	25	60	0.63901451
J	25	120	0.358714996
K	25	360	0.474729204
L	50	15	0.868830947
M	50	30	0.573739369
N	50	60	0.429798987
O	50	120	-0.571524022
P	50	360	0.58687183
Q	100	15	0.454409107
R	100	30	0.512332523
S	100	60	0.759824479
T	100	120	0.615964588
U	100	360	0.221648127

Table 3.1: Average silhouette values of IL-1β stimulated samples

Sample	SC-514 Inhibitor Concentration (μM)	Time Stimulated (min)	Silhouette Value
A	0	0	0.614813519
B	0	15	0.404275004
C	0	30	0.55997966
D	0	60	-0.202416091
E	0	120	0.781870607
F	0	360	0.675969987
G	25	15	0.816122348
H	25	30	0.026796662
I	25	60	0.154801007
J	25	120	0.335995239
K	25	360	-0.341793673
L	50	15	0.569374015
M	50	30	-0.692153301
N	50	60	0.377297193
O	50	120	0.572826577
P	50	360	0.050654947
Q	100	15	0.302729184
R	100	30	0.454443978
S	100	60	0.546283376
T	100	120	0.132332058
U	100	360	0.359292928

Table 3.2: Average silhouette values of TNF-α stimulated samples.

Dispersion on the log-transformed, non-dimensionally reduced data was calculated as the pairwise Euclidean distances between each sample represented as a vector of gene expression across all genes in the GRCm38 (mm10) genome (NCBI Assembly GCA_000001635.8). These pairwise distances were then displayed as a heatmap across samples for IL-1β stimulated samples (Fig 3.3c) and TNF-α stimulated samples (Fig 3.3d). Hierarchical clustering was also carried out to visualize clustering of biological replicates. This further corroborated statistical closeness of samples in each condition indicated by aforementioned silhouette analysis.

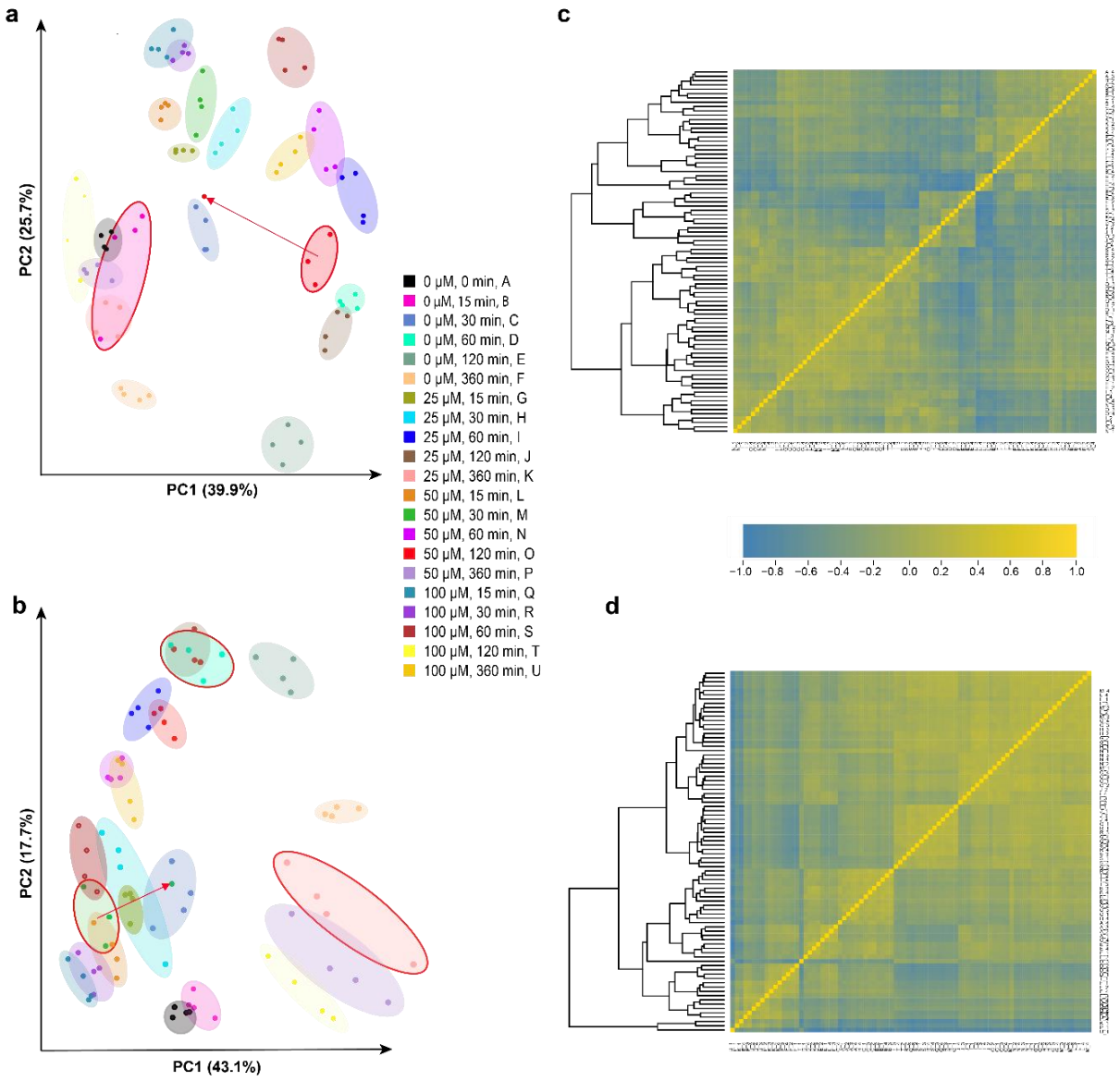

Figure 3.3: PCA and dispersion plots of RNA TagSeq data. a) PCA of IL-1β stimulated samples. b) PCA of TNF-α stimulated samples. Each color represents an experimental condition. Points represent biological replicates (n = 4 per condition). Samples determined to be of poor quality due to experimental error are indicated with red arrows. Conditions with negative average silhouette values are outlined in red. c) Heatmap representation and hierarchical clustering of dispersion statistics of IL-1β stimulated samples. d) Heatmap representation and hierarchical clustering of dispersion statistics of TNF-α stimulated samples. Gold indicates more highly correlated samples.

3.2.8 Statistical Analysis

Analyses for fluorescent images were performed with MATLAB (MathWorks Inc., Natick, MA). Error bars in Fig. 2-6 represent 95% confidence intervals. Comparison of the mean fluorescent intensity between control and inhibitor treated data sets was determined with a two-way analysis of variance test (ANOVA). A pairwise t-test was used to determine significant differences in the fold change of peak intensity values. For cell measurements from the image analysis, outlier samples were determined statistically through the Grubbs outlier test and were eliminated from the data set. Analyses for gene expression were completed in R. Standard error for the GLM coefficient based $\log_2$ fold change estimates are calculated using the curvature of each coefficient's posterior probability at the maximum of a density plot of coefficient estimates for $\log_2$ fold change. In *DESeq2*, p-values are generated using a Wald test and adjusted using Benjamini and Hochberg corrections [150].

3.2.9 Data Availability

The CellProfiler image analysis pipeline is available upon request. All processing code used in TagSeq processing including RMarkdown files containing session information used in differential expression analysis is available at https://github.com/sachitsaksena/nfkb-tag-seq.

3.2.10 Accession Numbers

Mouse genome (GRCm38 (mm10)): GCA_000001635.8

RNA TagSeq dataset deposited on NIH Sequence Read Archive: SRP163157

NCBI Gene Expression Omnibus with accession number GSE129678

3.2.11 Usage Notes

For pre-determined experimental low yield (corroborated by statistical analysis) samples 1-O-1 and 2-M-1 are recommended to remove from analyses. Removal of further samples should be done at the user's discretion.

3.3 RESULTS

3.3.1 IKKβ inhibition causes significant differences in temporal profiles of nuclear NF-κB translocation when stimulated with IL-1β

Representative images of NF-κB translocation after IL-1β stimulation at 0, 25, 45, and 90 min in three experimental conditions shown in Figure 3.4a. A difference in nuclear accumulation of NF-κB can be seen between untreated cells and cells treated with 25 μM of SC-514 at 25 and 45 min. An increased difference is apparent in cells treated with 100 μM of SC-514 and untreated cells at 25 and 45 min. At 90 min, NF-κB has cycled out of the nucleus and back into the

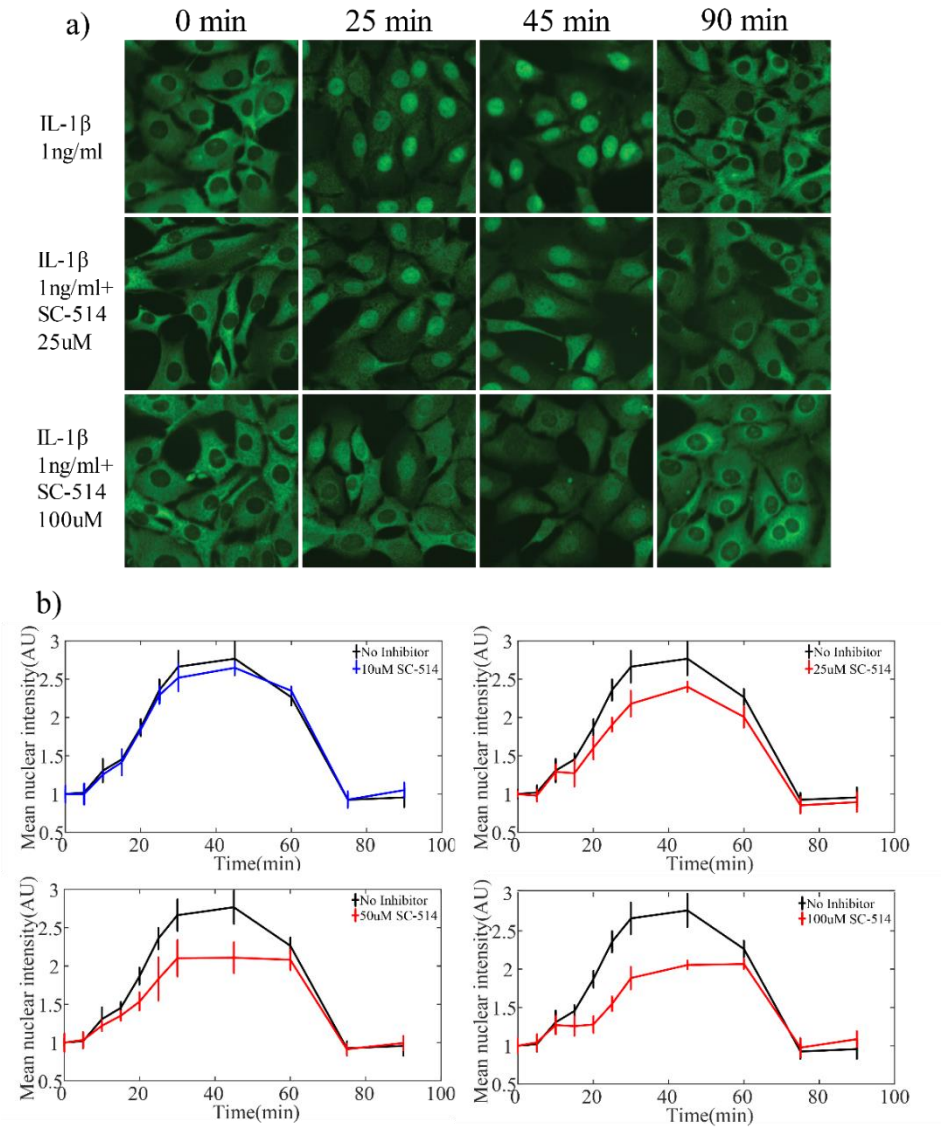

Figure 3.4: a) Representative images of NF-κB translocation over time. Row 1 shows untreated 3T3 fibroblast cells, while rows 2 and 3 display cells treated with 25 and 100 μM of SC-514, respectively. All cells were stimulated with IL-1β (1ng/ml) and fixed at 0, 25, 45, and 90 min. Visual differences in nuclear NF-κB translocation (stained green) can be seen between untreated cells and cells treated with 25 and 100 μM of SC514 at 25 and 45 min. b) Quantification of the mean nuclear NF-κB fluorescent intensity per each experimental condition. Nuclear and cytoplasmic regions were segmented from original immunofluorescence images and intensity values were averaged at each time point. Error bars represent 95% confidence intervals. A two-way analysis of variance test determined significant differences ($P < 0.05$) between time series of untreated cells and cells treated with 25, 50 and 100 μM of SC-514 (red).

cytoplasm in all experimental conditions. Statistical analyses revealed significant differences in time series between untreated cells and cells treated with 25, 50 and 100 μM of SC-514 ($P < 0.001$) (Figure 3.4b, red). Time series data of cells treated with 10 μM of SC-514 were also significantly different from cells treated with 25, 50, and 100 μM of SC-514 ($P < 0.001$) but not so when compared to untreated cells ($P = 0.224$). Significant differences were also observed between cells treated with 25 μM and those treated with 50 or 100 μM of inhibitor ($P = 0.027$ and $P < 0.001$, respectively). Significant differences were also significant between cells treated with 50 μM and 100 μM of inhibitor ($P = 0.003$). No concentration of inhibitor completely blocked nuclear translocation.

3.3.2 IKKβ inhibition causes significant differences in temporal profiles of nuclear NF-κB translocation when stimulated with TNF-α

Representative images of NF-κB translocation after TNF-α stimulation at 0, 25, 45, and 90 min in three experimental conditions are shown in Figure 3.5a. A difference in the nuclear accumulation of NF-κB can be seen between untreated cells and cells treated with 25 μM of SC-514 at 25 and 45 min. An increased difference is apparent in cells treated with 100 μM of SC-514 at 25 and 45 min. At 90 min, NF-κB has cycled out of the nucleus and back into the cytoplasm in all experimental conditions. Statistical analyses revealed significant differences in time series between untreated cells and cells treated with 10, 25, 50 and 100 μM SC-514 ($P < 0.001$) (Figure 3.5b, red). Time series data of cells treated with 10 μM of SC-514 were also significantly different from cells treated with 50 and 100 μM of SC-514 ($P = 0.012$ and $P < 0.001$, respectively). Cells treated with 25 μM and 50 μM of SC-514 had significant differences when compared to cells treated with 100 μM of inhibitor ($P < 0.001$). No significant differences were seen

between 10 µM and 25 µM conditions or 25 µM and 50 µM conditions (P = 0.585 and P = 0.091 respectively). No concentration of inhibitor completely blocked nuclear translocation.

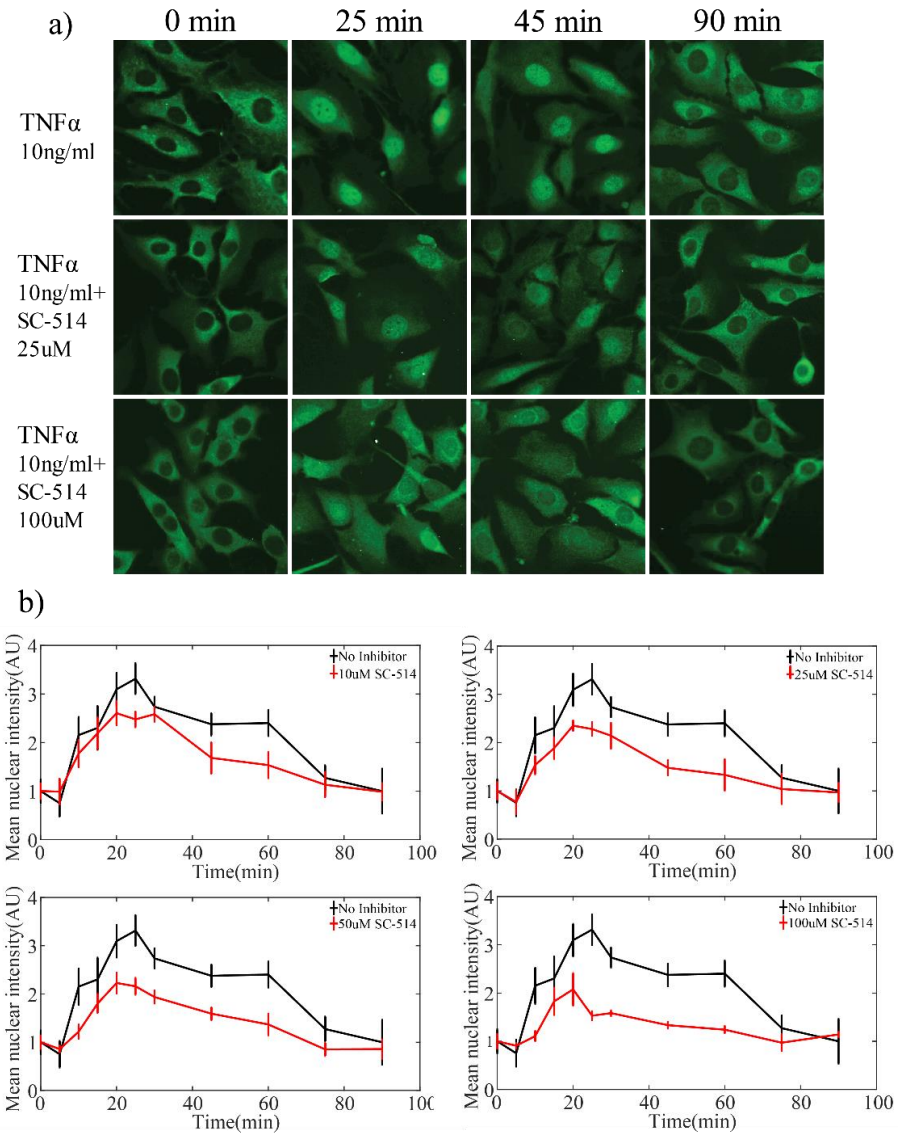

Figure 3.5: a) Representative images of NF-κB translocation over time. Row 1 shows untreated 3T3 fibroblast cells, while Rows 2 and 3 display cells treated with 25 µM and 100 µM of SC-514, respectively. All cells were stimulated with TNF-α (10 ng/ml) and fixed at 0, 25, 45, and 90 min. Visual differences in nuclear NF-κB translocation (stained green) can be seen between untreated cells and cells treated with 25 and 100 µM of SC514 at 25 and 45 min. b) Quantification of the mean nuclear NF-κB fluorescent intensity per each experimental condition. Nuclear and cytoplasmic regions were segmented from original immunofluorescence images and intensity values were averaged at each time point. Error bars represent 95% confidence intervals. A two-way analysis of variance test determined significant differences ($P < 0.05$) between time series of untreated cells and cells treated with 10, 25, 50 µM and 100 µM of SC-514 (red).

3.3.3 Degree of fold change in NF-κB nuclear translocation at peak activation is stimulus specific

The dose response for fold change in the mean NF-κB nuclear intensity at peak time points is shown in Figure 3.5. Cells stimulated with IL-1β reach peak activation at 45 min with a maximum fold change of 2.77 with no inhibitor (Figure 3.6a). There is a significant difference in intensity fold change between untreated cells and cells treated with 25 μM ($P = 0.013$) as well as 50 and 100 μM ($P < 0.001$) of SC-514 indicated with asterisks. Maximum difference in fold change is achieved with 50 μM of SC-514, reaching a fold change of 2.11, a 0.66 decrease from peak activation. There is no significant difference in peak activation between cells treated with 50 μM of inhibitor and 100 μM of inhibitor ($P = 0.554$) suggesting saturation of the inhibitor effect. Cells stimulated with TNF-α reach peak activation at 25 min with a maximum fold change of 3.31 with no inhibitor (Figure 3.6b) There is a significant difference in intensity fold change between untreated cells and cells treated with 10, 25, 50 and 100 μM ($P < 0.001$) of SC-514 indicated with asterisks. Maximum difference in fold change is achieved with 100 μM of SC-514, reaching a fold change of 1.53, a 1.78 decrease from peak activation.

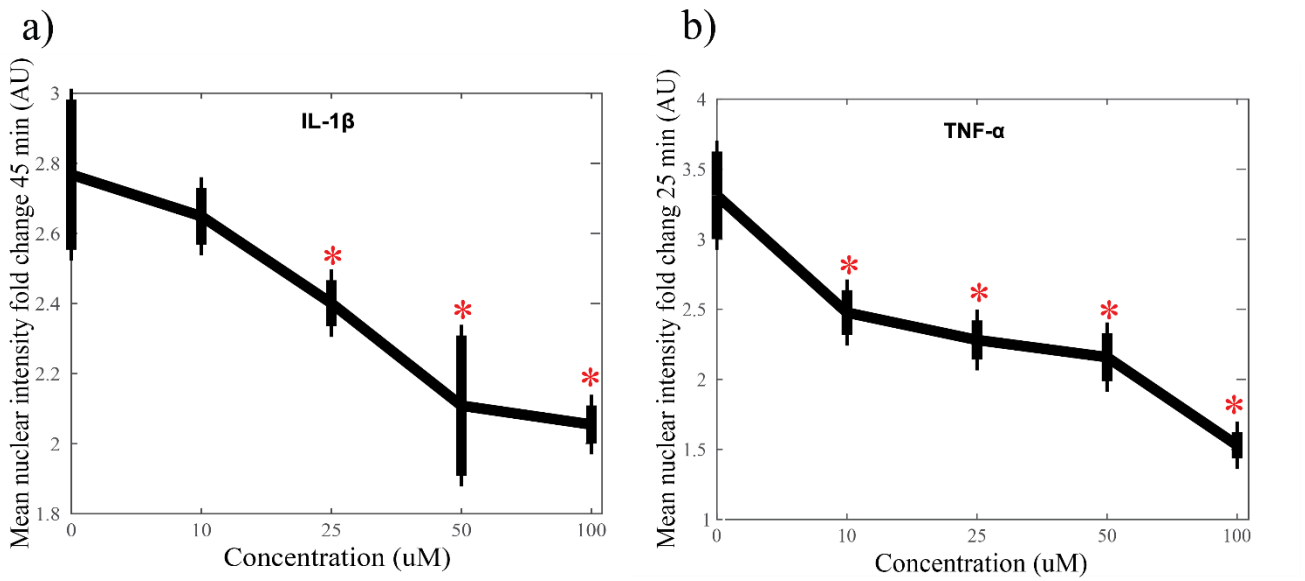

Figure 3.6: a) Mean nuclear intensity fold change of NF-κB translocation stimulated with IL-1β (1 ng/ml) at 45 min. Significant differences ($P < 0.05$) between untreated cells and cells treated with 25, 50, and 100 µM of SC-514 indicated with asterisk. The maximum fold change difference in peak activation from untreated cells was achieved with 50 µM SC-514. b) Mean nuclear intensity fold change of NF-κB translocation stimulated with TNFα (10 ng/ml) at 25 min. Significant differences ($P < 0.05$) between untreated cells and cells treated with 10, 25, 50, and 100 µM of SC-514 indicated with asterisk. Maximum fold change difference in peak activation from untreated cells achieved with 100 µM of SC-514.

3.3.4 RNA TagSeq data reveals temporal alterations in gene expression in response to stimuli

Total number of significantly ($P < 0.01$) differentially expressed genes in cells treated with 25, 50 and 100 µM of SC-514 compared to untreated cells after stimulation with IL-1β are shown in Figure 3.7. For each individual time point, the number of differentially expressed genes increases with inhibitor concentration. Log_2 fold changes in expression compared to untreated cells after stimulation with IL-1β of six inflammatory genes treated with 25, 50 and 100 µM of SC-514 are shown in Figure 3.7a. Significant differences in expression of cells treated with inhibitor from untreated cells

are shown in Figure 3.7b, red. Total number of significantly ($P < 0.01$) differentially expressed genes in cells treated with 25, 50 and 100 μM of SC-514 compared to untreated cells after stimulation with TNF-α are shown in Figure 3.8. For each individual time point, the number of differentially expressed genes increases with inhibitor concentration. Log_2 fold changes in expression compared to untreated cells after stimulation with TNF-α of six inflammatory genes treated with 25, 50 and 100 μM of SC-514 are seen in Figure 3.8a. Significant differences in expression of cells treated with inhibitor from untreated cells are shown in Figure 3.8b, red. Expression of Interleukin 1 receptor, type I (Il1r1) is downregulated in a dose dependent manner in cells stimulated with both IL-1β and TNF-α and has a consistent trend through time and between stimulation conditions. Early growth response 1 (Egr1) has a similar change in expression in both stimulation conditions, with the highest upregulation occurring at 15 and 120 min in a dose dependent manner. However, tumor necrosis factor alpha-induced protein 3 (Tnfaip3) is significantly upregulated in cells stimulated with TNF-α at 15 min which is not the case in cells stimulated with IL-1β. Cytochrome c oxidase II, mitochondrial (Cox2) and Interleukin 6 (Il6) exhibit varying degrees of up- and down- regulation through time. Particular differences in Cox2 expression between stimuli are seen at 15 min where IL-1β stimulated cells treated with 50 μM of inhibitor exhibit significant downregulation of expression while TNF-α stimulated cells do not and in expression of Il6 at 360 min where IL-1β stimulated cells treated with 25 μM exhibit an upregulation in expression and TNF-α stimulated cells do not.

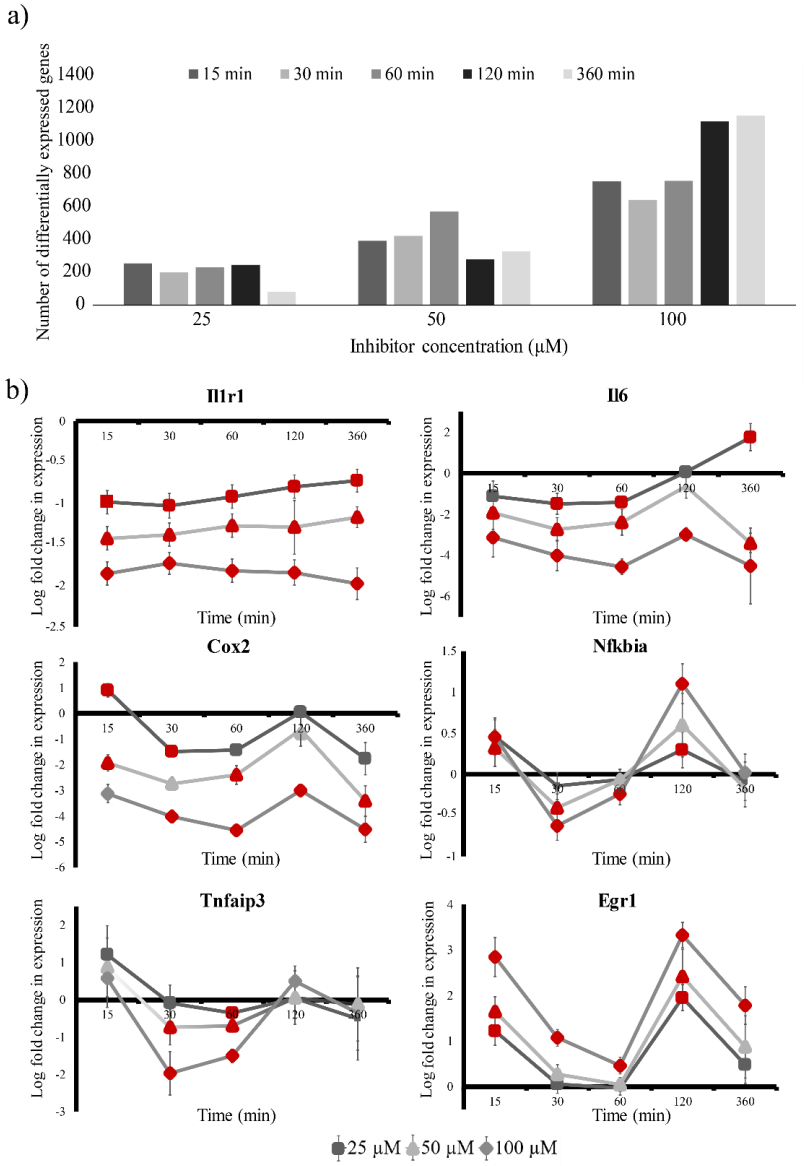

Figure 3.7: a) Total number of significantly differentially expressed genes ($P < 0.01$) in cells treated with 25, 50 and 100 µM of SC-514 compared to untreated cells at 15, 30, 60, 120, and 360 min after IL-1β (1ng/ml) stimulation. An increasing number of differentially expressed genes is seen with increasing concentration of SC-514 for each individual time point. b) Log_2 fold change in gene expression in cells treated with 25, 50 and 100 µM of SC-514 compared to untreated cells for six inflammatory genes: Il1r1, Il6, Cox2, Nfkbia, Tnfaip3 and Egr1 at 15, 30, 60, 120, and 360 min after IL-1β (1ng/ml) stimulation. Significance ($P < 0.05$) indicated in red. Note vertical axis are different for each gene.

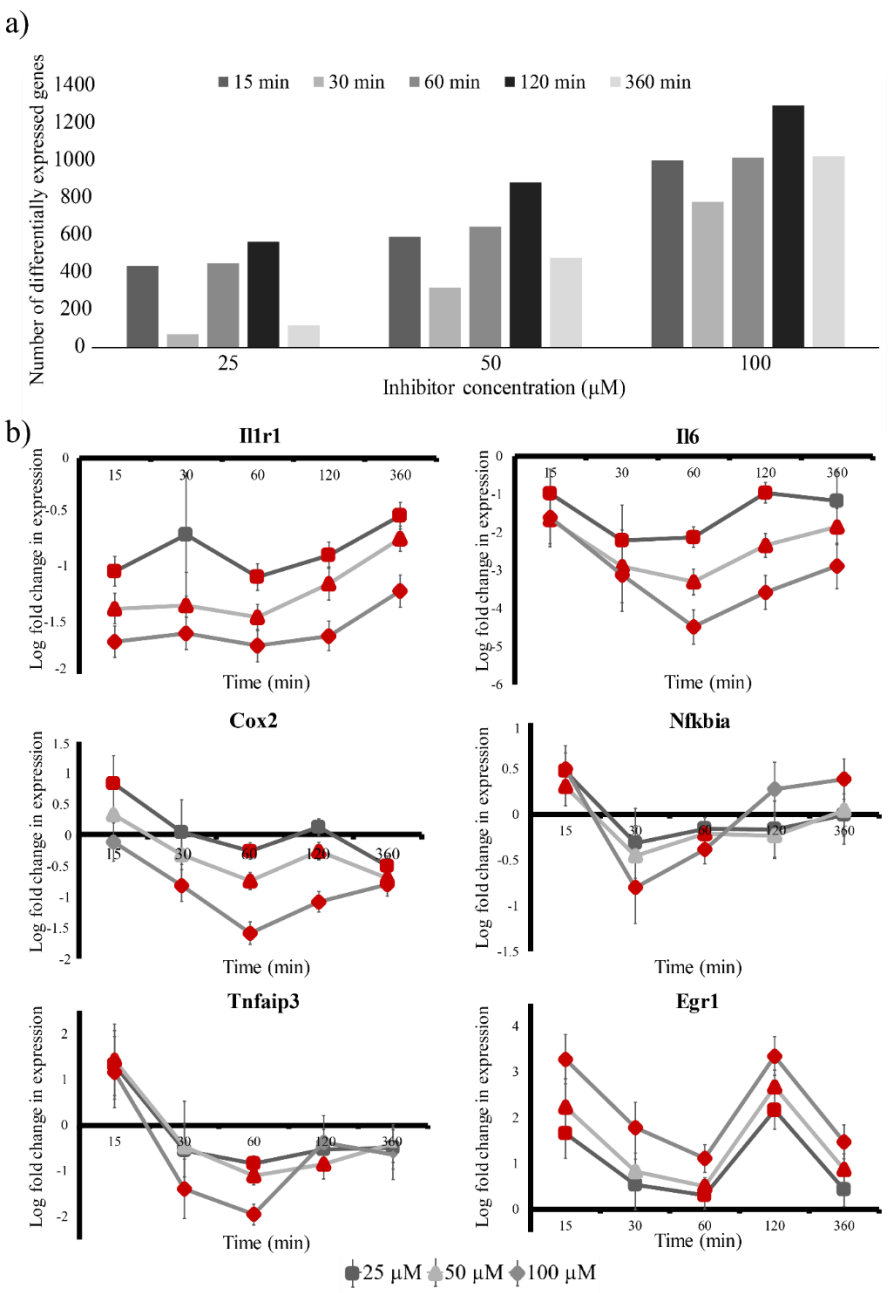

Figure 3.8: a) Total number of significantly differentially expressed genes ($P < 0.01$) in cells treated with 25, 50 and 100 µM of SC-514 compared to untreated cells at 15, 30, 60, 120, and 360 min after TNF-α (10 ng/ml) stimulation. An increasing number of differentially expressed genes is seen with increasing concentration of SC-514 for each individual time point. b) Log_2 fold change in gene expression in cells treated with 25, 50 and 100 µM of SC-514 compared to untreated cells for six inflammatory genes Il1r1, Il6, Cox2, Nfkbia, Tnfaip3 and Egr1 at 15, 30, 60, 120, and 360 min after TNF-α (10ng/ml) stimulation. Significance ($P < 0.05$) indicated in red Note vertical axis are different for each gene.

3.4 DISCUSSION

Regulation of NF-κB is a critical step in inflammatory diseases and cancer. Pathway analyses are necessary to understand NF-κB transcriptional activity to aid in the development of targeted treatments. This study quantitatively evaluated the effect of SC-514, a selective inhibitor of IKKβ, on NF-κB transcriptional activity using two stimuli, IL-1β and TNF-α. Results demonstrated significant temporal differences in NF-κB nuclear translocation between untreated cells and cells treated with various concentrations of SC-514 when stimulated with both IL-1β and TNF-α. Furthermore, this study identifies changes in inflammatory gene expression due to differing temporal profiles of NF-κB nuclear translocation of cells treated with IL-1β and TNF-α.

Protein- specific small molecules have been used to investigate signaling pathways and have proved valuable in developing targeted treatments [153]. These tools have allowed researchers to understand how specific signaling pathway perturbations alter genetic profiles and cellular function in disease states [138, 139, 153, 154]. Previous studies have shown altering upstream signaling events can effect NF-κB transcriptional activity [138–141],[155–157]. Our results corroborate this and further quantify these differences on a dose dependent level. A decrease in peak activation of NF-κB was seen even at low concentrations (i.e., 10 and 25 μM); however, there was never a complete blockade. Our results are in agreement with studies that show decreased activation of NF-κB due to perturbations of the IKK complex [155–157]; however, the timing and degree of NF-κB inhibition varies in studies depending on the cell type and stimulus [138, 158]. This demonstrates how various cells can interpret signals independently and yield

different responses [159]. Cellular function must be taken into consideration when conducting pathway analyses in targeted drug development, as one pathway of interest may be present in multiple cell types relevant to the disease state.

The results of the present study show a stimulus specific response of NF-κB activation between cells stimulated with IL-1β and TNF-α supporting preliminary studies which investigated how targeting signaling dynamics through pharmacological intervention can produce stimulus-selective responses [17]. When stimulated with IL-1β, cells exhibit peak NF-κB activation at 45 min, a significant change in temporal profile starting with concentrations of 25 μM SC-514, and a maximum decrease in peak intensity with 50 μM of SC-514. These results show SC-514 blunts, in a concentration-dependent manner the amplitude of the transient peak of NF-κB activity induced by IL-1β stimulation. Interestingly, even at the highest dose, SC-514 does not change the timing of the signal decay. When stimulated with TNF-α, cells exhibit peak NF-κB activation at 25 min, a significant change in temporal activation profile starting with 10 μM of SC-514, and maximum decrease in peak activation with 100 μM of SC-514. These results show SC-514 substantially re-modulates, in a concentration-dependent manner, the temporal dynamics of the NF-κB signal induced by TNF-α stimulation. In contrast to the IL-1β case, IKK inhibition by SC-514 seem to affect both peak amplitude as well as the decay of the signal induced by TNF-α. These findings warrant further analyses quantifying the effect of SC-514 on additional pathway molecules, including IKK itself in this specific cell type, to determine other possible factors contributing to dynamical changes.

Results from genetic sequencing yield results in agreement from others showing that manipulation of IKK leads to distinct NF-κB activation profiles and changes in gene expression profiles [134, 160], however our findings offer a further in depth analysis using longitudinal gene expression data with varying degrees of IKK inhibition in response to IL-1β and TNF-α. Overall, there is an SC-514 dose dependent trend of increasing differentially expressed genes through time. When looking at individual gene expression profiles through time, vast expression differences are observed in certain genes between experimental conditions.

Pathway perturbations can have differing effects on transcriptional activity depending on the stimuli present and is important to consider when designing therapeutic targets; in this application, especially in diseases where the inflammatory stimuli levels can vary such as cancer and rheumatoid arthritis [161, 162]. Our results not only elucidate differences in inflammatory gene expression between stimuli but also show how expression levels can change in a matter of minutes, demonstrating the need for further, highly time-resolved gene expression studies.

A limitation of this study is that analyses were performed at fixed times on populations of cells. Real time, single cell imaging data would better capture cell to cell heterogeneity and assess the signaling consequences from these differences. This study focuses specifically on NF-κB dynamical changes from IKK inhibition; monitoring pathway proteins upstream of NF-κB would offer additional insight on the mechanisms of these changes. Further studies should also investigate dynamical changes from pathway perturbations in the NF-κB network at later time scales and the differences that

arise in inflammatory gene expression. Additionally, our results would be further generalized if evaluated in other cell types. There may be differences between cell responses in the 3T3 cells used in these studies and primary cell lines. Studying the changes in signal dynamics due to pathway perturbations *in vivo* will increase biological insight of cellular behavior in disease states and prove valuable in pharmacology.

3.5 CONCLUSION

In summary, we demonstrate novel differences in early NF-κB transcriptional activity from IKKβ selective inhibition in response to IL-1β and TNF-α. Significant differences of NF-κB nuclear translocation were quantified at a high temporal resolution to both stimuli and revealed stimulus-specific responses to perturbation. Furthermore, gene expression profiles revealed an increase in significantly differentially expressed genes with increasing concentration of IKKβ inhibition. Individual inflammatory genes were up and down regulated with varying degrees calling for further analysis of specific genes of interest. This work analyzes changes in signaling and transcriptional dynamics necessary to develop effective NF-κB pathway targeted drugs and delineates the importance of pathway analyses in therapeutic design.

Chapter 4: Anti-HER2 induced myeloid cell alterations correspond with increasing vascular maturation[2]

4.1 INTRODUCTION

Approximately one in five cases of breast cancer overexpress the human epidermal growth factor receptor 2 (HER2) [71]. Patients with HER2+ breast cancer have shorter disease free survival, decreased overall survival rates, and greater metastatic potential than HER2- patients [26, 76]. The current standard-of-care therapy for HER2+ breast cancer is cytotoxic chemotherapy in combination with trastuzumab, a targeted monoclonal antibody that binds to the HER2/neu receptor. Treatment with trastuzumab induces cell cycle arrest and inhibits cancer cell proliferation [23, 163]. Trastuzumab can also downregulate the expression of HER2 by promoting receptor internalization and degradation [83]. As a secondary effect, trastuzumab has been shown to alter the characteristics of tumor-associated vessels through increasing vascular maturation and stabilization in HER2+ tumors [21, 22, 164, 165]. Such changes can subsequently enhance the efficacy of combination therapies and improve treatment response in multiple types of cancer including breast, colon and lung [21, 166, 167]. With less than half of patients responsive to neoadjuvant therapy in HER2+ breast cancer, further understanding vascular changes that have potential to enhance therapeutic response may provide a clinically translatable benefit [80].

Trastuzumab-induced vascular maturation is partly attributed to the decrease in vascular endothelial growth factor (VEGF) secretion, but the exact mechanisms have

[2]This chapter was submitted to a peer-reviewed journal: Bloom MJ, Jarrett AM, Triplett TA, Syed AK, Davis T, Yankeelov TE, Sorace AG. Anti-HER2 induced myeloid cell alterations correspond with increasing vascular maturation. Journal of Mammary Gland Biology and Neoplasia. 2019. Bloom MJ designed and performed experiments, analyzed data, and wrote the publication.

not fully been elucidated [21, 22, 164]. Clinical data evaluating progression-free survival from anti-angiogenic therapies targeting VEGF signaling pathways (such as bevacizumab) in breast cancer conflict between the United States and the European Union, but neither finds a significant improvement in overall survival rates [168–171]. One mechanism by which tumor cells can become resistant to anti-VEGF therapy is through the recruitment of pro-angiogenic, immunosuppressive myeloid cells [172, 173]. Myeloid cells are non-lymphoid immune cells that influence the development of tumor vasculature through the secretion of pro- and anti-angiogenic factors [174, 175]. When anti-VEGF therapies are administered at high doses or for a prolonged period of time, tumor vasculature is overly pruned and leads to tumor hypoxia and upregulation of hypoxia inducible factors (HIFs) [173, 176]. HIFs drive recruitment of tumor associated macrophages (TAMs), myeloid derived suppressor cells (MDSCs), and prevent maturation of dendritic cells [174, 177, 178]. Angiogenesis is then driven by myeloid cells through both VEGF dependent and independent pathways enhancing tumor progression [172, 173]. However, when tumor vasculature is normalized, tumor hypoxia decreases, and the balance of angiogenic factors in the tumor microenvironment can be restored through the reprogramming of the myeloid cell population—further stabilizing the vasculature and promoting antitumor responses [179, 180]. Both clinical and preclinical studies show that treatment with trastuzumab alters immune infiltration (including myeloid populations) in HER2+ tumors [181–183]; however, to our knowledge, a detailed immune panel in HER2+ breast cancer identifying changes in myeloid populations to trastuzumab has not been conducted.

Our previously acquired immunofluorescence data revealed an increase specifically in the macrophage population after trastuzumab treatment [183]. TAMs are a significant component of the breast tumor microenvironment and of particular interest

due to their influence in tumor progression and response to treatment [184, 185]. TAMs largely polarize towards two phenotypes, “classical” (M1) or “alternative” (M2) depending on the stimuli present in the tumor microenvironment and have been shown to either enhance (M1) or suppress (M2) anti-tumor immune responses [101, 186]. Macrophage differentiation towards the M2 phenotype are driven by interleukin 4 (IL-4) and interleukin 13 (IL-13); and promote angiogenesis by secreting VEGF, basic fibroblast growth factor, and several matrix metalloproteases (MMPs) [102, 103, 105]. Macrophages are polarized towards an M1 phenotype by lipopolysaccharide and interferon gamma (IFN-γ). They have a lower angiogenic potential than M2 macrophages and promote anti-tumor immunity through secretion of pro-inflammatory cytokines and increased antigen presentation ability [102–105].

In this study, we sought to gain insight into the mechanisms of improved tumor vascularization and heightened windows of anti-tumor immunity after administration of trastuzumab. First, we evaluated immune modulation by quantifying the number of macrophages with an M2 phenotype to an M1 phenotype following treatment in a xenograft model by flow cytometry and validated concurrent vascular alterations using quantitative histology. Finally, we identify changes in tumor cytokines and chemokines relating to immunity and angiogenesis through a multiplex immunoassay.

4.2 Materials and Methods

4.2.1 Cell Culture

BT474 breast cancer cells were purchased from ATCC (Manassas, Virginia). Cells were cultured in improved minimal essential medium (IMEM, Invitrogen, Carlsbad, CA) supplemented with 10% FBS, 1% penicillin/streptomycin, and 20 μg/mL insulin. Cells were grown at 37 °C with 5% CO_2. Cells were cultured to 70-

80% confluency and all cell counts were determined by the Countess II FL automated cell counter (Thermo Fisher Scientific Inc., Waltham, MA).

4.2.2 Animal Procedures

All procedures were approved by our institution's animal care and use committee. Female nude athymic mice (N = 56) were purchased from The Jackson Laboratory (Bar Harbor, ME) at 3-4 weeks of age. After a one-week acclimation period, mice were subcutaneously implanted with a 0.72 mg, 60-day release, 17β-estradiol pellet (Innovative Research of America, Sarasota, FL) in the nape of the neck. 24 hours later, 10^7 BT474 breast cancer cells in 100 µl serum-free IMEM media with 30% growth factor-reduced Matrigel were injected subcutaneously into the right flank of the mouse. Tumors were grown to approximately 250 mm^3 (estimated 8-10 weeks) at which point the animals were entered into the study. Animals were randomly sorted into treatment groups and administered either trastuzumab (10 mg/kg) or saline on three different days (Days 0, 3 and 6) *via* intraperitoneal (IP) injection during a week-long treatment plan. Mice were euthanized for tissue processing on days 0 (N = 5), 4 (N = 6 control, N = 6 treated) and 7. Mice taken down on Day 7 either received two total doses of treatment on Days 0 and 3 (N = 6 control, N = 5 treated) or three total doses of treatment on Days 0, 3 and 6 (N = 5 control, N = 6 treated) (Figure 4.1).

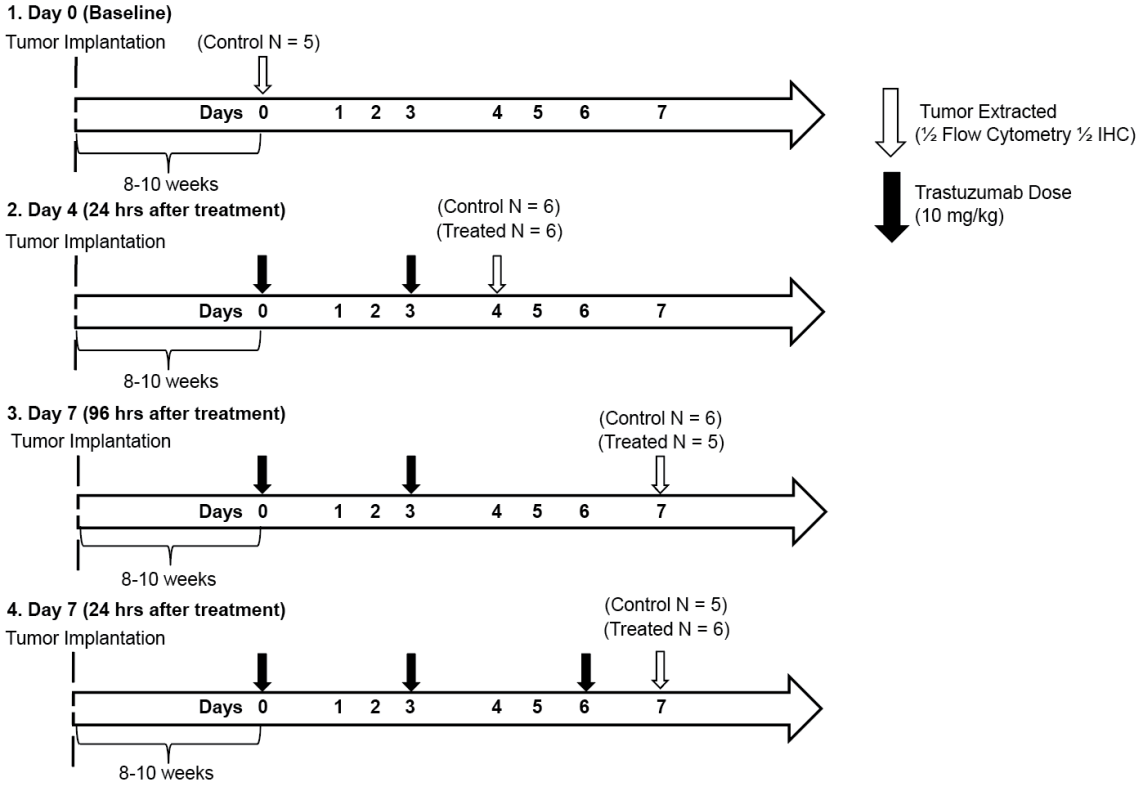

Figure 4.1: Outline of experimental procedure and treatment schedules. BT474 HER2+ tumor-bearing mice were divided into four treatment groups. Tumors were extracted from group 1 on Day 0 without treatment. Group 2 and 3 received two doses of saline (Control) or trastuzumab (Treated) on Days 0 and 3 and tumors extracted on Day 4 (group 2) and Day 7 (group 3). Group 4 received three doses of saline or trastuzumab on Days 0, 3 and 6 and had tumors extracted on Day 7.

4.2.3 Spleen Disaggregation

The spleen was excised and immediately placed on ice in RPMI 1640 serum free media (Caisson Laboratories, Smithfield, UT). All further incubation periods and reagents were at 4°C. The spleen was then homogenized to a single cell suspension and diluted in flow wash buffer (FWB, PBS + 1% FBS + 5mM EDTA). Cells were resuspended in 1× red blood cell (RBC) lysis buffer (Biolegend, San Diego, CA) for 3 minutes. The cell suspension was washed in FWB and filtered through a 70 μM strainer.

4.2.4 Tumor Disaggregation

One hour prior to mouse sacrifice, each mouse received 60 mg/kg of pimonidazole (Hypoxyprobe, Inc., Burlington, MA) in a 100 μl intravenous injection. After tumor excision, the tissue was cut at the longest cross-section and half was placed in a tissue cassette and incubated in 10% neutral buffered formalin (Fisher Scientific International Inc., Pittsburgh, PA) for 48 hours. Samples were then transferred to 70% ethanol and prepped for immunohistochemistry (IHC) staining. The other half of the tumor was cut into 2-3 mm pieces and placed in 0.15% collagenase type IV (Worthington Biochemical Corporation, Lakewood, NJ) with 5 mM Ca^2 at 1 mL/100 mg of tissue. Mechanical dissociation was performed using the gentleMACs dissociator (Miltenyi Biotec, Bergisch Gladbach, Germany). Samples were incubated while rotating at 37°C for 45 minutes. After digestion, the suspension was washed in FWB and resuspended in 3 mL of 1× RBC lysis buffer for 3 minutes on ice. Cells were washed in FWB and filtered through a 70 μM strainer.

4.2.5 Flow Cytometry

Cells harvested from the spleen were used for single color controls and multi-color staining control. Control and tumor samples were resuspended at a concentration of 10^6 cells/100 μL in FWB in round bottom polystyrene tubes. Cells were stained with the following antibody fluorophore conjugates: CD45-PerCP/Cy5.5, CD11c-Pacific Blue, CD11b-AF700, MHCII-APC/Cy7, Ly6c-BV510, Ly6g-APC, CD38-FITC (Biolegend, San Diego, CA), F480-PE/Cy7 (Tonbo Biosciences, San Diego, CA), CD206-PE (R&D Systems, Minneapolis, MN) and propidium iodide (PI, Enzo Life Sciences, Farmingdale, NY). All antibody staining took place for 30 minutes at 4°C in the dark. For all experiments, cells were acquired on the BD LSRII Fortessa flow cytometer.

Compensation and sequential gating was performed with FlowJo software (FlowJo LLC, Ashland, OR). Populations of myeloid cells that were identified included macrophages, dendritic cells, granulocytic myeloid derived suppressor cells (G-MDSC), monocytic myeloid derived suppressor cells (M-MDSC) and M0, M1 and M2 macrophage phenotypes (Figure 4.2).

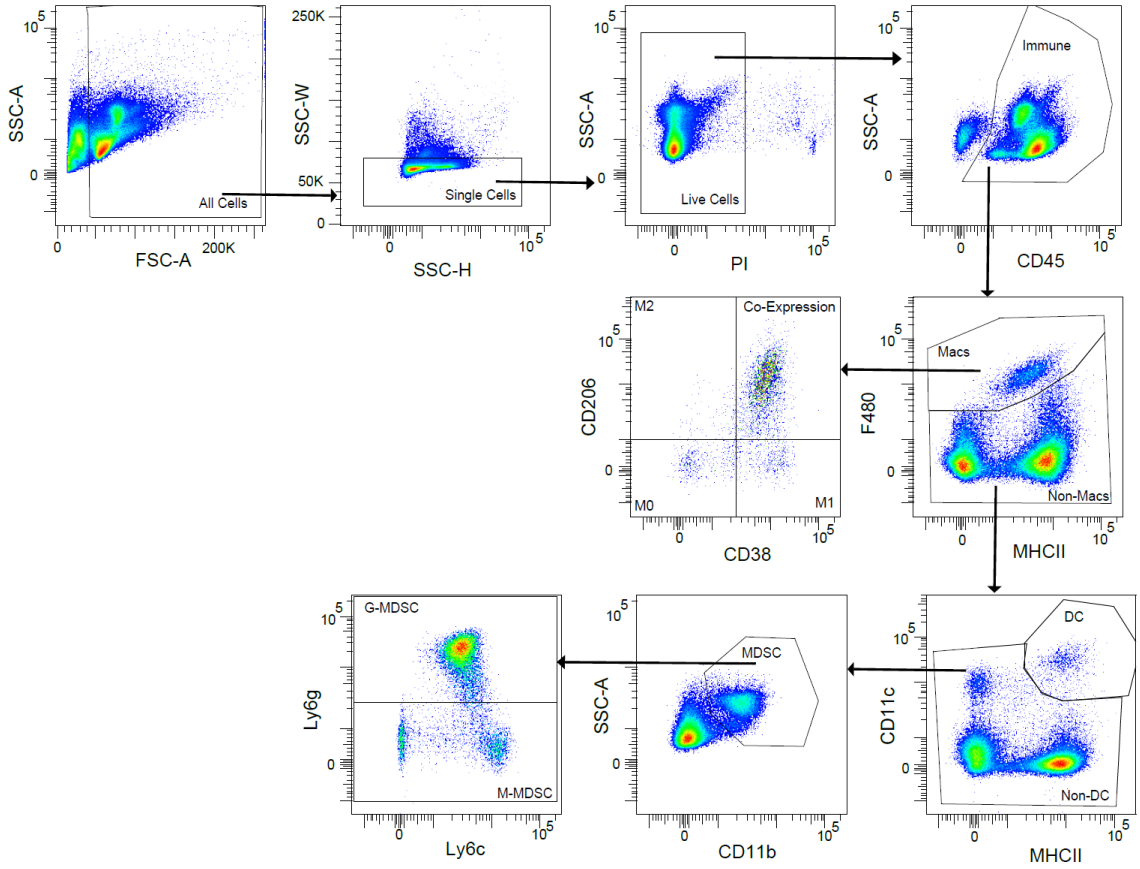

Figure 4.2: Gating strategy for all flow cytometry samples. Cell debris and cell doublets were eliminated using forward scatter (FSC) and side scatter (SSC). Live cells were identified as negative for propidium iodide signal. Immune cells were gated as CD45+. Macrophages were gated using F480+ and MHCII+. Macrophage phenotypes were identified as the following: M0 (CD38-/CD206-), M2 (CD38-/CD206+), Co-Expression (CD38+/CD206+) and M1 (CD38+/CD206-). Non-macrophages were further identified as dendritic cells (CD11c+/MHCII+). MDSC were identified as CD11b+ with Ly6g+ indicating G-MDSC, and Ly6g- indicating M-MDSC.

4.2.6 Immunohistochemistry

Formalin fixed tumor sections were embedded in paraffin. Tumors were then sliced into 4 μM sections and stained for the following: hematoxylin and eosin (H&E), mouse anti-CD31, mouse anti-α-smooth muscle actin (α-SMA, Abcam, Cambridge, UK), mouse anti-F480 (Invitrogen, Carlsbad, CA), and human anti-Ki67 (R&D Systems, Minneapolis, MN). Immuno-stained slides were scanned (20×, 0.495 μm/pixel) with the Aperio ScanScope (Leica Microsystems, Wetzlar, Germany). Automated segmentation of tissue structure was completed using custom MATLAB algorithms (MathWorks Inc., Natick, MA). All images were uniformly segmented based on thresholds determined from positive and negative controls for each stain except for regions of necrosis, which were determined manually from H&E staining. Images were registered to the corresponding H&E stained image from that sample. For registration, images were converted to grayscale. Transformations applied to images consisted of translation, rotation and scale (similarity) based on intensity differences. A viable tissue mask was defined as total tumor area minus necrotic area. Macrophage infiltration (F4/80) was defined as the percent of positive stain per viable tissue area. Microvessel density (CD31) and vascular smooth muscle coverage (α-SMA) were calculated as the number of vessels per mm^2 of tumor tissue. The vessel maturation index was evaluated as the ratio of α-SMA coverage to microvessel density [187]. To confirm treatment response, proliferation (Ki67) was defined as the percent of total tumor nuclei positively stained. All codes are available upon request.

4.2.7 Cytokine Detection Assay

Tumor bearing mice (n = 10) were treated with either three total doses of trastuzumab (10 mg/kg) or saline for 1 week on Days 0, 3 and 6. On Day 7, tumors were

excised and flash frozen with liquid nitrogen in *Optimal Cutting Temperature compound* (*Tissue*-Tek; Sakura Finetek USA). Tumors were lysed in Cell Lysis Buffer 2 (R&D Systems, Minneapolis, MN). Samples were concentrated using Pierce Protein Concentrator PES 3K (Thermo Fisher Scientific Inc., Waltham, MA), and original sample protein concentration was determined using the NanoDrop 2000 (Thermo Fisher Scientific Inc., Waltham, MA). The multiplex assay was conducted using the Bioplex 200 (BioRad Laboratories, Hercules, CA). Samples were incubated with premixed beads targeted to 12 different analytes according to the Mouse Magnetic Luminex Assay (R&D Systems, Minneapolis, MN) specifications. Protein concentrations were determined using corresponding standard curves for each analyte (Figure 4.3).

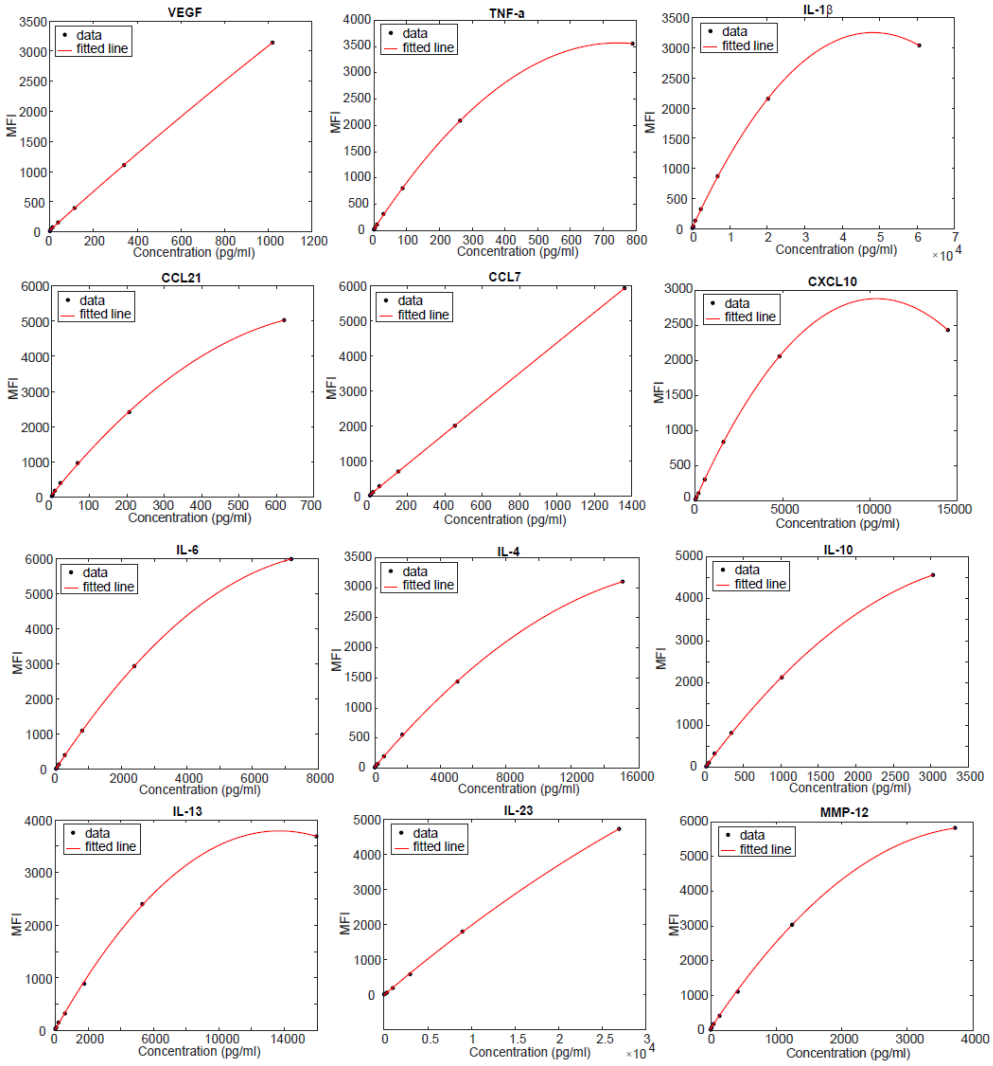

Figure 4.3: Standard curves for multiplex cytokine assay.

4.2.8 Statistical Analysis

Statistical analysis was conducted using MATLAB (MathWorks Inc., Natick, MA). Statistical differences between treatment groups of flow cytometry, immunohistochemistry, and cytokine data were determined using a nonparametric Wilcoxon rank sum test. All data is presented as mean ± standard error with $P \leq 0.05$ indicating significance. Linear regression parameters and Pearson correlation coefficients

were determined for flow cytometry and histology comparisons. Tumors were eliminated from analysis if viability was < 50% due to prolonged incubation as determined with live/dead stain in flow cytometry (N = 4), or if ≥ 4 myeloid cell populations were significant outliers (N = 3). Outliers were defined as a value more than three absolute deviations from the median.

4.3 RESULTS

4.3.1 Macrophage infiltration increases transiently after trastuzumab treatment

Flow cytometry data revealed increased tumor macrophage infiltration 24 hours after trastuzumab treatment compared to controls (Fig. 4.4a). On Day 4, 24 hours after the second dose of trastuzumab, the percent of macrophages making up the tumor-infiltrating immune cells increased from 30.52 ± 5.34% in control to 45.87 ± 2.1% in treated mice (P = 0.02). On Day 7, 96 hours after two doses of trastuzumab, no significant difference was seen between control (29.97 ± 6.63%) and treated (20.31 ± 5.3%) tumors of that group (P = 0.43). On Day 7, 24 hours following a third doses of trastuzumab, the macrophage population increased from 26.54 ± 6.54% in control tumors to 50.05 ± 5.14% in treated tumors (P = 0.03). Populations of dendritic cells (Figure 4.4b), G-MDSC (Figure 4.4c) and M-MDSC (Figure 4.4d) were quantified in all treatment groups; however, no significant differences were observed.

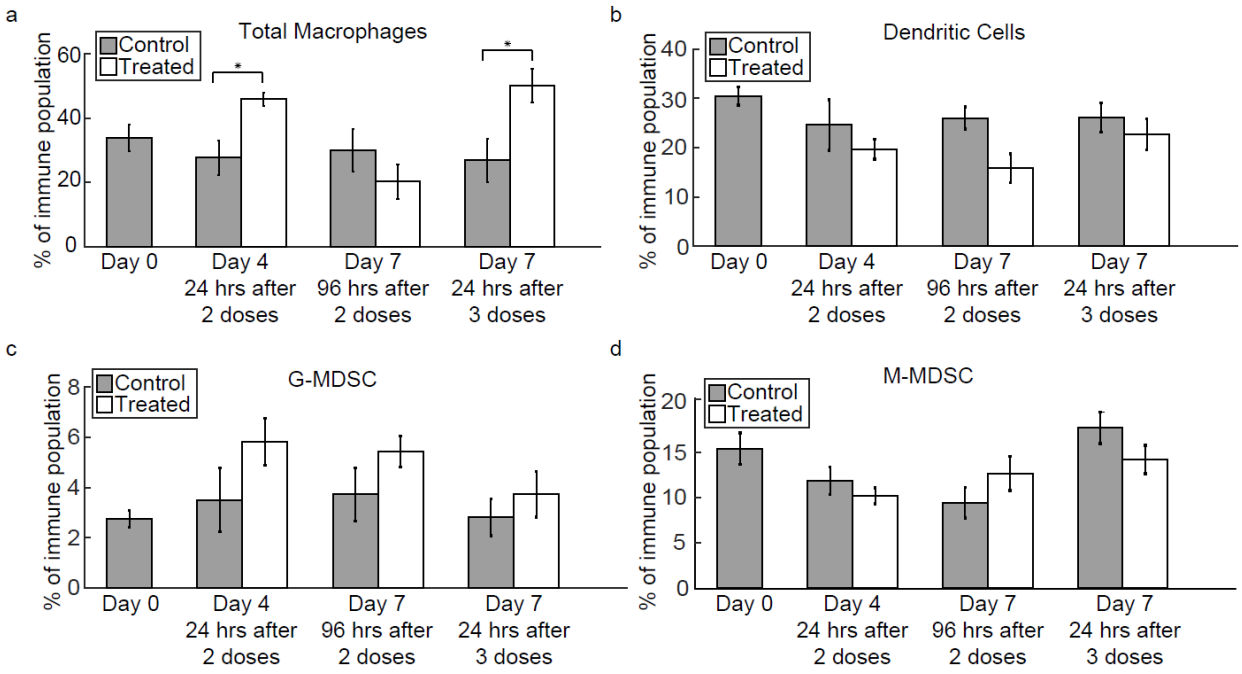

Figure 4.4: Macrophage infiltration increases 24 hours after administration of trastuzumab. a) Percent of total macrophages in the tumor immune population is shown, revealing a significant increase in macrophage infiltration on Day 4 (P = 0.02) and Day 7, 24 hours after treatment (P = 0.03) compared to control tumors. Percent of b) dendritic cells, c) G-MDSC and d) M-MDSC is shown in the tumor immune population (no significant differences were observed between control and treated tumors).

4.3.2 M1 macrophage phenotype becomes more abundant in tumors over the course of trastuzumab treatment

Representative flow cytometry data plots of changes in M0 (CD38-/CD206-), M1 (CD38+/CD206-), M2 (CD38-/CD206+) [188, 189] macrophage subtypes and co-expression (CD38+/CD206+) over the course of trastuzumab treatment are shown in Figure 4.5a. While control tumors were consistent between treatment groups, tumors co-expressing CD38 and CD206 increased on Day 4 (24 hours after a second dose of trastuzumab) from 27.1 ± 4.12% to 56.9 ± 8.82% (P = 0.02) (Figure 4.5b). No differences were seen in co-expression between control and treated tumors in the other treatment

groups. After a third dose of trastuzumab was given, the percent of M1 macrophages significantly increased from 13.38 ± 3.65% to 31.07 ± 2.9% (P = 0.02) (Figure 4.5c). There was a decrease in non-differentiated M0 macrophages on Day 4 from 45.36 ± 6.13% in control tumors to 19.03 ± 4.53% in treated tumors (P = 0.02) and on Day 7, 24 hours after treatment from 52.44 ± 9.82% to 34.08 ± 2.74% (P = 0.03) (Figure 4.5d). No significant differences were observed in the percent of M2 macrophages across treatment groups (Figure 4.5e). In control and treated spleens taken down at Day 4, there were no statistical differences between macrophage populations (Figure 4.6) that suggests this effect is tumor specific.

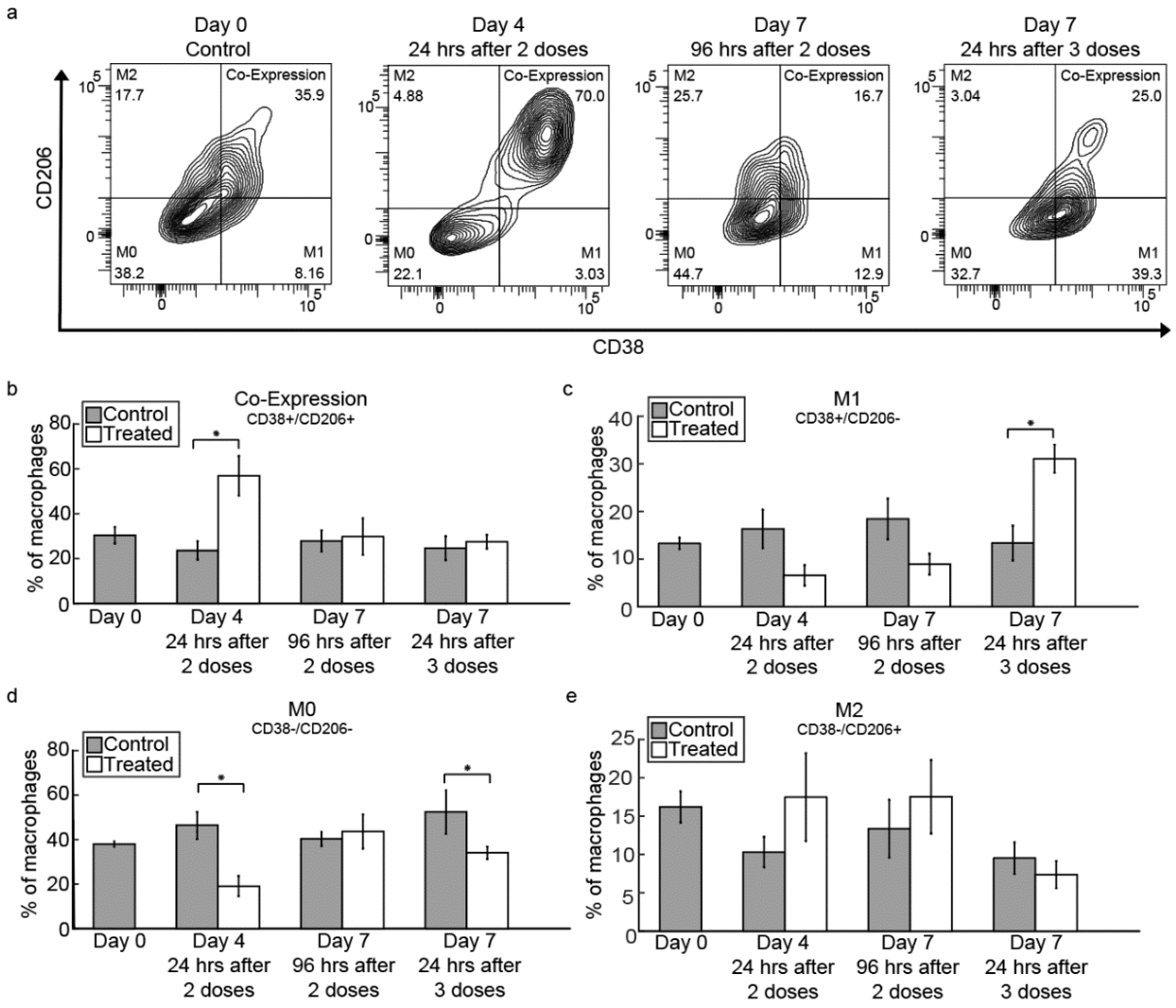

Figure 4.5: Macrophage phenotypes transition over the course of trastuzumab treatment. a) Representative flow cytometry graphs of Day 0 control tumors and Day 4 and Day 7 trastuzumab treated tumors (96 and 24 hours after treatment). Visual increases are observed in CD38+/CD206+ co-expressing macrophages on Day 4, 24 hours after treatment and CD38+/CD206- M1 macrophages on Day 7, 24 hours after trastuzumab treatment. b) Percent of macrophages co-expressing CD38 and CD206 is shown revealing a significant increase ($P = 0.02$) from control in Day 4 treated tumors, after two doses of trastuzumab. c) Percent of macrophages with an M1 phenotype (CD38+/CD206-) is shown revealing a significant increase ($P = 0.02$) in the M1 macrophage population in treated Day 7 tumors after three doses of trastuzumab. d) Percent of macrophages with a non-differentiated, M0 phenotype (CD38-/CD206-) is shown revealing a significant decrease in population observed on Day 4 ($P = 0.02$) and Day 7 ($P = 0.03$), 24 hours after treatment. e) Percent of M2 macrophages (CD38-/CD206+) (no significant differences were observed between control and treated tumors).

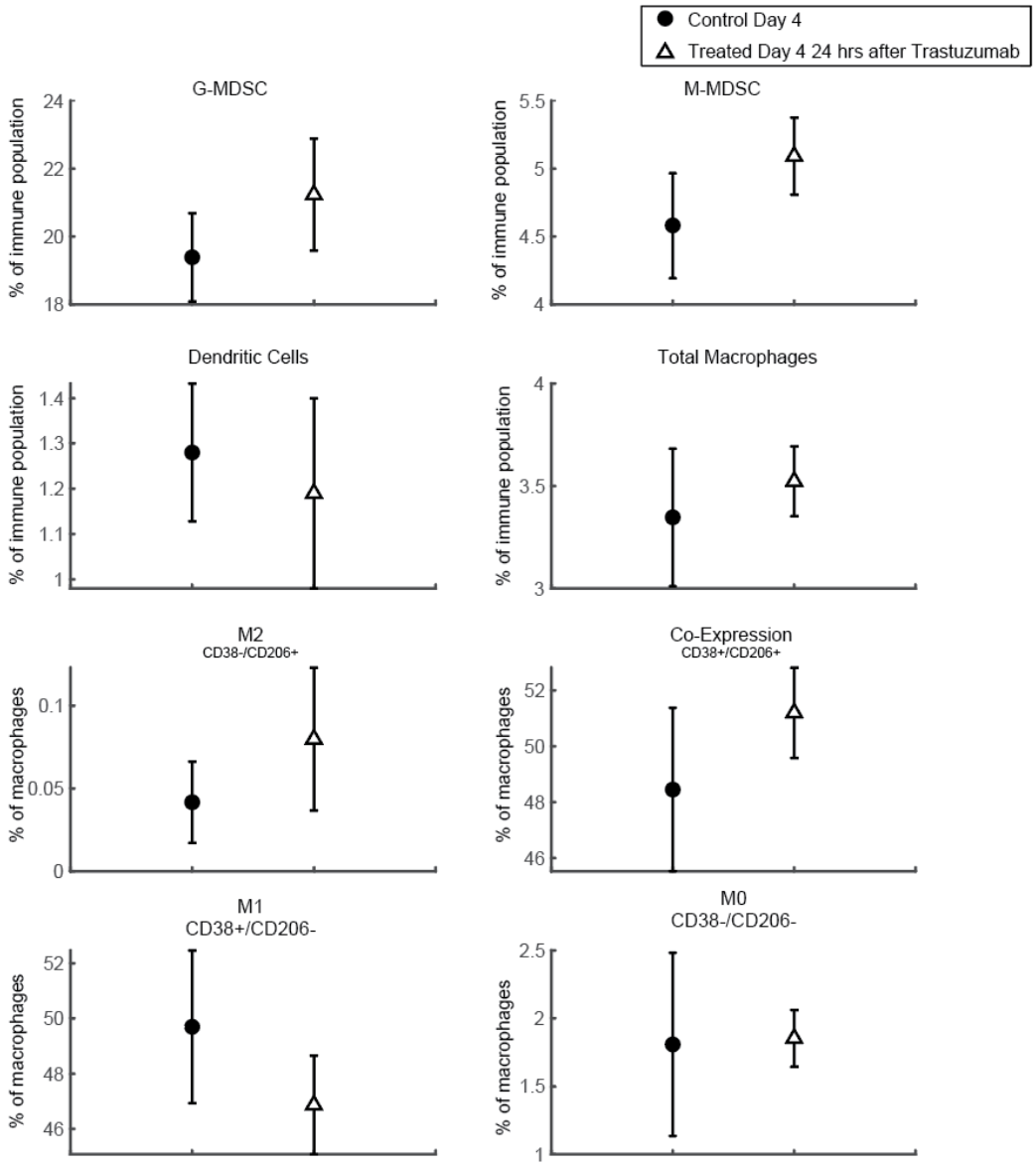

Figure 4.6: Spleens taken from control and treated mice on Day 4, 24 hours after trastuzumab treatment. No significant differences ($P > 0.05$) were observed in G-MDSC, M-MDSC, dendritic cells, macrophages, M2, Co-Expression, M1 or M0 populations. (N = 5 control, N = 4 treated).

4.3.3 Vessel maturation index increases over the course of trastuzumab treatment and correlates with increasing M1 macrophage populations

Representative images of F4/80 staining in control and treated Day 4 tumors are shown in Figure 4.7a. Comparison between percent F4/80+ cells in flow cytometry analysis and percent area F4/80+ in corresponding tumor central slices showed a significant positive linear correlation ($R = 0.35$, $P = 0.03$) (Figure 4.7b). Representative images of CD31 and α-SMA in control and treated Day 4 tumors are shown in Figure 4.8a. No significant differences in microvessel density or α-SMA coverage were observed between control and treated tumors (Figure 4.8b and 4.8c, respectively). The vessel maturation index increased on Day 7 after three doses of trastuzumab from 11.13 ± 1.90% for control tumors to 22.58 ± 3.17% for treated tumors ($P = 0.04$) (Figure 4.8d). Comparison of vessel maturation and percent M1 macrophages from flow analysis revealed a significant positive linear correlation ($R = 0.33$, $P = 0.04$) (Figure 4.8e).

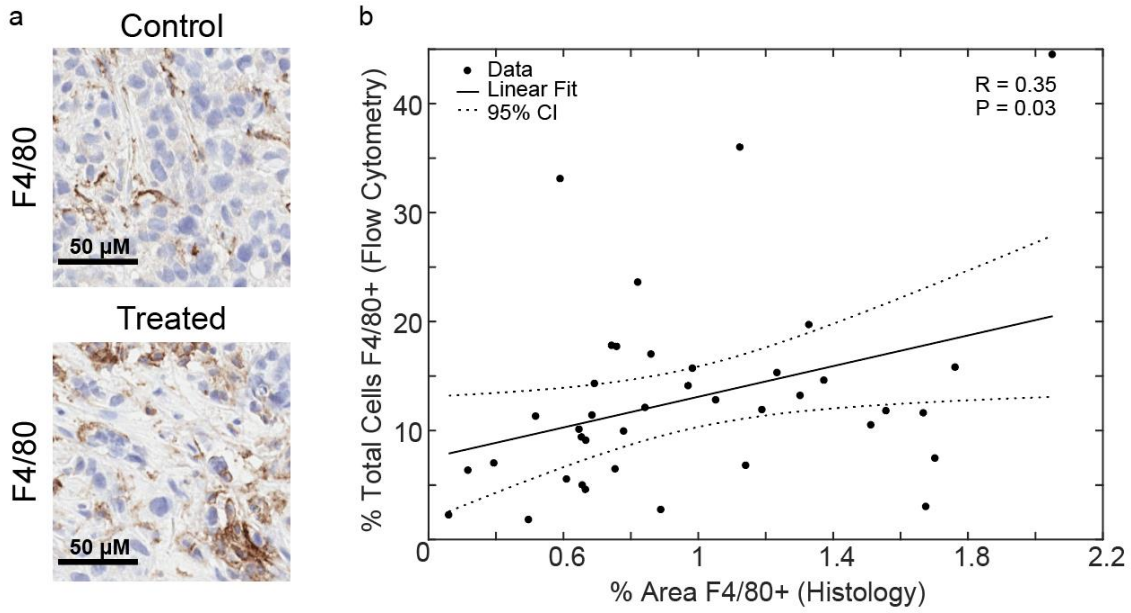

Figure 4.7: Correlation between F4/80+ determined by flow cytometry and IHC staining. a) Representative IHC stained images of F4/80 in Day 4 control (top) and trastuzumab treated (bottom) tumors. b) Linear correlation between percent of total cells F4/80+ as determined by flow cytometry and percent of total tumor area F4/80+ determined by IHC staining in the corresponding tumor central slice showing a positive linear correlation (R = 0.35, P = 0.03).

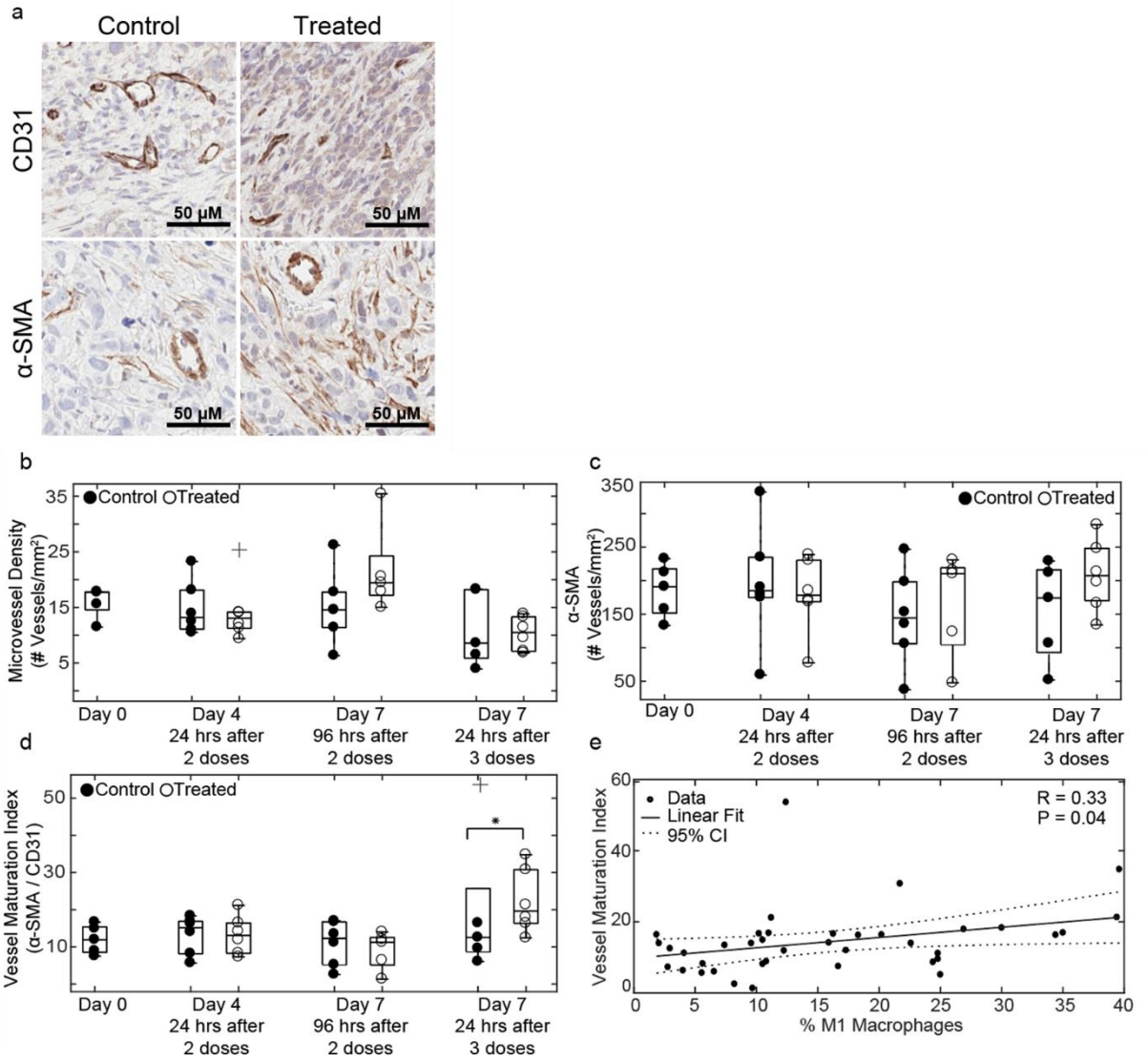

Figure 4.8: Vascular changes over the course of trastuzumab treatment positively correlate with macrophage phenotypic alterations. a) Representative images of CD31 (top) and α-SMA (bottom) in Day 4 control and trastuzumab treated tumors. b) CD31 microvessel density and c) α-SMA coverage in control and trastuzumab treated tumors (no significant differences were observed). d) Vessel maturation index as determine by ratio of α-SMA to CD31 microvessel density in control and trastuzumab treated tumors is shown, revealing a significant increase in vessel maturation index on Day 7, 24 hours after a third dose of trastuzumab (P = 0.04). e) Linear correlation between vessel maturation index and percent M1 macrophages in corresponding tumor halves as determined by flow cytometry showing a positive linear correlation (R = 033, P = 0.04).

4.3.4 Trastuzumab induced changes in inflammatory cytokines

To determine if cytokine differences were also present in tumors that displayed a higher percentage of M1 macrophages, a cytokine multiplex assay was conducted to evaluate differences between control and treated tumors on Day 7, 24 hours after being treated with three doses of trastuzumab (Figure 4.9). Treated tumors had a significant decrease in the pro-angiogenic factor VEGF-A ($P = 0.008$) and increases in pro-inflammatory cytokines TNF-α and IL-1β ($P = 0.024$ and 0.032, respectively). Significant increases in chemokines CCL21 ($P = 0.016$), CCL7, and CXCL10 ($P = 0.008$) were also seen in treated tumors compared to control. Changes in IL-6, IL-4, IL-10, IL-13, IL-23, and MMP-12 were evaluated, but no significant differences were found between control and treated tumors.

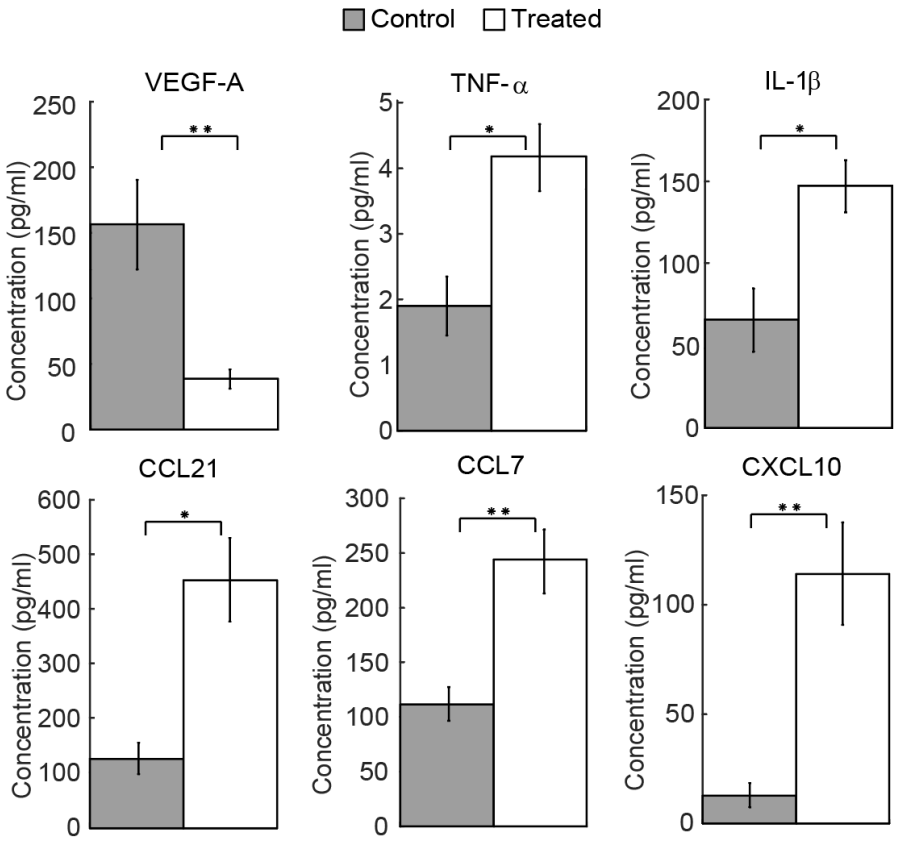

Figure 4.9: Continued trastuzumab treatment induces changes in tumor cytokine levels. Day 7 control and trastuzumab treated tumors (24 hours after three doses of treatment) were evaluated for murine VEGF-A, TNF-α, IL-1β, CCL21, CCL7, and CXCL10 cytokine levels. A significant decrease in VEGF-A (P = 0.008) was observed in treated tumors compared to control. A significant increase in TNF-α (P = 0.024), IL-1β (P = 0.032), CCL21 (P = 0.016), CCL7 and CXCL10 (P = 0.008) was observed in treated tumors compared to control

4.3.5 Validation of treatment response and necrosis in control and treated tumors

Representative images of Ki67 and H&E stains are shown in Figure 4.10a. Treatment response was confirmed in all treatment groups indicated by significant decreases in Ki67 expression (Figure 4.10b). Day 4 trastuzumab treated tumors had an average Ki67 expression of 12.41 ± 2.06% while control tumors showed 27.66 ± 2.33% ($P = 0.03$). Treated tumors taken down on Day 7 after two doses of trastuzumab had 13.77 ± 1.56% Ki67+ nuclei compared to 24.40 ± 1.34% ($P = 0.05$) in control tumors. Tumors taken down on Day 7 after three doses of trastuzumab had 19.15 ± 2.66% Ki67+ nuclei compared to 28.70 ± 2.48% ($P = 0.03$) in Day 7 control tumors. No significant differences were observed between control and treated tumors in percent necrosis (Figure 4.10c).

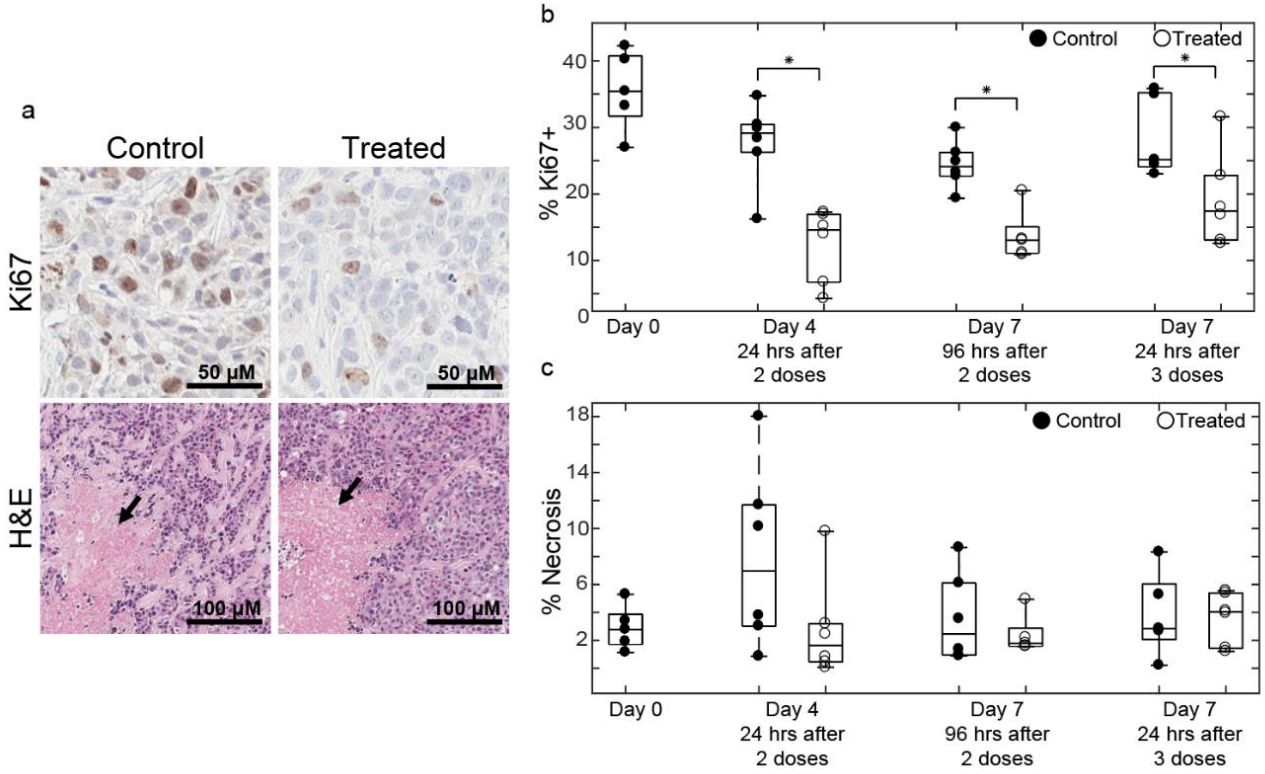

Figure 4.10 Quantitative analysis of Ki67 and necrosis in IHC stained samples. a) Representative images of Ki67 (top) in control and treated Day 4 tumors are shown. Necrotic sections from H&E (bottom) indicated with black arrow in control and treated Day 4 tumors. b) Percent nuclei Ki67+ in control and trastuzumab treated tumors. In all treatment groups, there was a significant decrease ($P \leq 0.05$) in Ki67+ nuclei, validating treatment response. c) Percent necrotic area in control and treated tumors (no significant differences were observed between control and treated tumors).

4.4 DISCUSSION

There is a well-developed field focused on exploiting vascular maturation to improve the response of cancers to therapy [166, 167, 176, 190]. Vascular maturation promoted by anti-HER2 targeted therapy with trastuzumab has been shown to enhance response to combination paclitaxel and doxorubicin chemotherapy in mouse models of breast cancer [21, 165]. Identifying underlying mechanisms of vascular changes will benefit clinical treatment regimens by elucidating methods to enhance and sustain vascular perfusion for improved drug delivery. Determining immune related mechanisms of vascular maturation could offer clinical benefit in developing combination immunotherapy treatments with trastuzumab. The present study evaluated trastuzumab induced changes of myeloid cell infiltration in a murine model of HER2+ breast cancer. Our results demonstrated continuous trastuzumab treatment alters pro-inflammatory innate immune components of the tumor microenvironment while simultaneously increasing vascular maturation.

Immunophenotyping by flow cytometry revealed a transient increase in macrophage infiltration in treatment groups that were evaluated 24 hours after administration of trastuzumab (Figure 4.4a). With continued treatment, macrophages transitioned to an M1 phenotype (Figure 4.5c). When treatment stopped for four days, macrophages reverted to phenotypes similar to those found in control tumors. The results from our study showed an increase in M1 macrophage population positively correlating with an increase in vascular maturation after persistent trastuzumab treatment (Figure 4.8e). Similarly, in a murine model of pulmonary fibrosarcoma, Rolny *et al*. showed that genetically inducing tumor production of histidine-rich glycoprotein (HRG) inhibited tumor growth and metastasis, and where HRG only sustained vascular normalization through the polarization of M1 macrophages [180]. Furthermore, Huang *et al*. found that

low dose anti-VEGF receptor 2 therapy normalized tumor vasculature and polarized TAMs towards an M1 phenotype and improved response to combination immunotherapy in mouse models of breast cancer [179]. Additional studies depleting macrophages from the system used in our study would offer further quantitative information on macrophage contribution to vascular maturation and tumor response.

The changes in cytokine profiles of trastuzumab treated tumors support the results from immunophenotyping and histological evaluation. Our study revealed a decrease in host VEGF-A and simultaneous increases in several pro-inflammatory cytokines and chemokines (Figure 4.9), which agrees with what has been previously shown [21]. VEGF-A is a key regulator of angiogenesis and decreases in VEGF-A aligns with the increase in vascular maturation evaluated by histology with continued treatment of trastuzumab (Figure 4.8d). In conjunction with an increase in total macrophage infiltration 24 hours after treatment, there was a simultaneous decrease in non-differentiated, M0 macrophages (CD38-/CD206-) (Figure 4.5d). This could in part be due to changes in inflammatory cytokines and chemokines in the tumor microenvironment (Figure 4.9). M1 macrophages secrete increased amounts of TNF-α and IL-1β over M2 or M0 macrophages [101]. With continued treatment of trastuzumab, by Day 7 we see an increase in M1 macrophages (Figure 4.5c) and increases in TNF-α and IL-1β (Figure 4.9). Chemotaxis is induced differently in M1 and M2 macrophages. In this study, CXCL10, CCL21 and CCL7 were both upregulated in trastuzumab treated tumors. Others have found CXCL10 and CCL21 to induce chemotaxis specifically in M1 macrophages [191, 192]. Studies show CCL7 can induce chemotaxis in both M1 and M2 macrophages [192, 193]. Although the changes in cytokines of the tumor microenvironment support the observed changes in macrophage phenotypes, many of the molecules can have both pro- and anti- tumor effects. Additional studies are needed to

fully understand the underlying mechanisms cytokine treatments have to skew the inflammatory and angiogenic potential of tumors.

In the clinic, TAMs are being investigated as prognostic and diagnostic biomarkers [10, 194, 195]. In several cancers, including breast, TAM density correlates with worse overall survival rates [10, 196]; however, TAM phenotypes can influence response to treatment. A recent study conducted in patients with stage II colon cancer showed that patients with a high M2/M1 (CD206+/CD68+) macrophage ratio were more likely to benefit from adjuvant chemotherapy than patients with a low M2/M1 ratio, who did not show any clinical benefit—therefore, identifying a subset of patients that would not need additional treatment following surgery [197]. Clinical trials with therapies inhibiting tumor macrophage recruitment to solid tumors have not been successful in showing improved tumor response [113, 114]. Ongoing preclinical and clinical work is being done in identifying drug targets that can reprogram immunosuppressive macrophages [115–117]. This study shows preliminary evidence that trastuzumab, already used in the clinic to treat HER2+ breast cancer, has the potential to repolarize M2 macrophages towards an M1 phenotype.

A limitation of this study is that mice were taken down at fixed time points and measurements could not be made longitudinally in the same animal. However, our methods allowed for an extensive immunophenotyping panel and simultaneous analyses of vascularity from central slice immunohistochemistry staining. Noninvasive imaging, such as immuno-PET imaging, is an alternative method that could give more finely time resolved data of immune infiltration after treatment, although it would only allow for measurement of one target at a time and may lack the spatial resolution required to fully assess immune response.

Although a xenograft model was used in this study, murine macrophages do respond to trastuzumab (primarily through the FcγIV receptor [198]) and no significant differences in macrophage quantities or phenotypes were observed between spleens of Day 4 control and treated mice, showing immune response was directly tumor associated (Supplementary Fig. S3). The results from this study motivate future research in mouse models with intact (or humanized immune systems) to further characterize trastuzumab induced immune infiltration. Determining effective markers to distinguish M1/M2 macrophage phenotypes is an active area of research [199, 200]. Two other markers considered for this study were inducible nitric oxide synthase (iNOS, M1 expressed) and early growth response protein 2 (Egr2, M2 expressed) [199]. The distribution of macrophage phenotypes in Day 0 control spleens did not differ using iNOS and Egr2 from using CD38 and CD206, and the latter were chosen for this study. Computational methods that analyze multidimensional flow cytometry data could be used in the future to analyze a panel with several macrophage markers to identify further phenotype subsets (i.e. M2a, M2b, M2c).

4.5 Conclusion

In summary, this study identified novel differences in myeloid cell infiltration between control and trastuzumab treated tumors. With continued treatment, TAMs polarized to a pro-inflammatory M1 phenotype and increased macrophage transitioning correlated with increased vascular maturation. Previous studies show increases in therapeutic efficacy when optimizing trastuzumab combination dosing regimens with cytotoxic therapy. This study offers preliminary evidence of immune mechanisms of vascular maturation and the potential for trastuzumab to reprogram an immunosuppressive tumor microenvironment, specifically by polarizing macrophages

towards an M1 phenotype. Further longitudinal assessments of trastuzumab induced immune changes may identify optimal combination regimens with immunotherapy and have potential to enhance clinical outcomes in breast cancer.

Chapter 5: Quantifying the Effects of Combination Trastuzumab and Radiation Therapy in HER2+ Breast Cancer

5.1 INTRODUCTION

Human epidermal growth factor receptor 2 (HER2) positive breast cancer is characterized by overexpression of the HER2/neu receptor and represents 15-20% of annual breast cancer cases [71]. Trastuzumab, a monoclonal antibody targeted to the HER2 receptor, is used clinically in both neoadjuvant and adjuvant standard-of-care treatment and is often combined with radiation in the adjuvant setting to eliminate residual disease and prevent recurrence [23, 163, 201]. Preclinical studies have shown that overexpression of HER2 is a contributing factor to radiation resistance, and treatment with anti-HER2 therapy could potentially act as a radiosensitizer [27–31]. However, HER2+ patients still have a greater chance of recurrence than patients with HER2- status [26]. Thus, there is a need to further investigate optimizing the use of trastuzumab and radiation in a combination treatment regimen.

One mechanism by which HER2 overexpression promotes tumorigenesis is through inhibition of apoptosis by upregulation of the phosphatidylinositol 3'-kinase–protein kinase B–mammalian target of rapamycin (PI3K/AKT/mTOR) pathway. Trastuzumab blocks PI3K/AKT/mTOR pathway signaling, causing cell cycle arrest and inducing cancer cell death [202]. Studies from Guo *et al.* and Liang *et al.* found that combination trastuzumab sensitizes HER2+ breast cancer cells to radiation therapy *in vitro*, and that the upregulation of PI3K/AKT pathway may be specifically involved in radioresistance in HER2+ breast cancer [27, 29]. Additionally, breast tumors can become hypoxic due to the irregular and tortuous vasculature which increases radioresistance [203–205]. Breast cancer cells exposed to chronic hypoxia can develop lower levels of reactive oxygen species which prevents stabilization of DNA damage caused by radiation

and enhances cell survival [206, 207]. Godet *et al.* showed that breast cancer cells with lower reactive oxygen species levels due to chronic hypoxia exposure *in vivo* had a higher potential to invade surrounding tissue and were four times more likely to metastasize [207]. Previous results in HER2+ breast cancer have revealed that treatment with trastuzumab can increase tumor oxygenation in a pre-clinical mouse model through stabilization of tumor blood vessels [208]. Although there has been investigation into the potential radiosensitization ability of trastuzumab in breast cancer, studies lack longitudinal data and fail to quantify sensitization over time, reducing clinical relevance. Furthermore, the effects of the sequence of therapies has not been systematically investigated [209].

Common *in vitro* approaches for evaluating cell response to radiation therapy include end point analyses such as the 3-[4,5-dimethylthiazolyl-2]-2,5-diphenyltetrazolium bromide (MTT) assay or the clonogenic assay. Results evaluating cell viability after treatment can largely vary depending on the end time point chosen [210]. However, these methods lack the ability to longitudinally observe cell response which is critical in determining underlying changes in cell physiology during therapy [211]. This study will use the IncuCyte Live-Cell Analysis System (Essen Bioscience, Ann Arbor, MI) which delivers real-time data of cellular responses and has been shown to be accurate in analyzing changes in breast cancer cell proliferation through time [212].

This contribution has three goals 1) investigate the effects of radiation and trastuzumab *in vitro*, 2) quantify the effects of radiation and trastuzumab combination therapy longitudinally *in vitro*, and 3) test the hypothesis that trastuzumab sensitizes HER2+ breast cancer to radiation therapy in an *in vivo* model of HER2+ breast cancer. Quantifying the synergy between trastuzumab and radiation over time has the potential to

elucidate optimal combination regimens and decrease the amount of therapy needed to achieve rumor control or eradication.

5.2 MATERIALS AND METHODS

5.2.1 Cell Culture

BT474 cells were maintained in improved minimal essential medium (IMEM, Invitrogen, Carlsbad, CA) supplemented with 10% FBS, 1% penicillin/streptomycin, and 20 μg/mL of insulin. SKBR3 cells were cultured in McCoy's 5A medium (ATCC, Manassas, VA) supplemented with 10% FBS and 1% penicillin/streptomycin. MDA-MB-231 cells were maintained in Dulbecco's Modified Eagle's Medium (Thermo Fisher Scientific Inc., Waltham, MA) supplemented with 5% FBS and 200 μg/mL of G418. All cells were grown at 37 °C with 5% CO_2. Cells were cultured to 70-80% confluency and cell counts were determined with the Countess II FL automated cell counter (Thermo Fisher Scientific Inc., Waltham, MA).

5.2.2 Western Blot Evaluation of HER2 Expression and Quantification

BT474, SKBR3 and MDA-MB-231 breast cancer cells were washed with ice cold phosphate buffered saline and lysed for 10 minutes on ice with radioimmunoprecipitation assay buffer (RIPA) buffer supplemented with protease inhibitor (Roche Applied Science, Indianapolis, IN). Lysates were centrifuged at 13,400 g for 20 minutes at 4° C and collected for bicinchoninic acid (BCA) protein quantification assay *via* the Nanodrop 2000c spectrophotometer (Thermo Fisher Scientific, Waltham, MA). For each cell line, 20 μg of protein was prepared in a solution of sodium dodecyl sulfate (SDS) and β-mercaptoethanol and boiled for 5 minutes at 95° C. Samples were run on a NuPAGE Bis-Tris gel and transferred to a polyvinylidene fluoride (PVDF) membrane. The membrane

was blocked in 5% dry milk in tris-buffered saline (TBST), probed with horseradish peroxidase (HRP) conjugated mouse anti-human β-actin overnight at 4° C and developed with the Amersham ECL western blot detection system (GE healthcare, Buckinghamshire, UK) for one minute at room temperature. Membranes were developed in the absence of light and visualized with an SRX-101A Medical Film Processor (Konica Minolta Medical and Garphic, Inc., Shanghai, China). The membrane was incubated in stripping buffer for 15 minutes, washed with TBST and probed with Rabbit anti-human HER2/ErbB2 primary antibody (Cell Signaling Technology, Danvers, MA) for 2 hours at room temperature. The membrane was washed, incubated with HRP conjugated goat anti-rabbit IgG secondary antibody (Cell Signaling Technology, Danvers, MA) for 1 hour at room temperature. After a final wash, the membrane was redeveloped and visualized for HER2 expression. Quantification of bands was conducted with the Image Studio Lite program, version 5.0 (LI-COR Biosciences, Lincoln, NE, USA). HER2 expression was normalized to β-actin expression for quantification.

5.2.3 Transfection of Breast Cancer Cell Lines

Enhanced green fluorescent protein (EGFP) expressing BT474 and MDA-MB-231 cells were a gift from Dr. Amy Brock at The University of Texas at Austin. SKBR3 cells were transfected to express EGFP through a Sleeping Beauty Transposon System. An EGFP plasmid was obtained and cloned into a Sleeping Beauty compatible vector, psDBbi-Neo (Addgene, Cambridge, MA, plasmid #60525). Co-transfection of the psDBbi-Neo vector and the pCMV (CAT) T7-SB100 (Addgene, Cambridge, MA, plasmid #34879) Sleeping Beauty transposase was used to introduce the EGFP plasmid into the SKBR3 cell line through Lipofectamine LTX (Thermo Fisher Scientific, Waltham, MA). Following transfection, cells were cultured in their respective media

supplemented with 200 μg/mL geneticin for four weeks to select for positively transfected cells. Fluorescence activated cell sorting was used to separate cells based on fluorescent expression, and the top 25% of EGFP expressing cells were used in experiments. The pCMV (CAT)T7-SB100 plasmid was a gift from Dr. Zsuzsanna Izsvak [213] and the pSBbie-Neo was a gift from Dr. Eric Kowarz [214].

5.2.4 *In Vitro* Treatment Experiments

5.2.4.1 Experiment 1: Order of dosing

BT474-GFP cells were plated in 96-well plates at 5,000 cells/well. 24 hours later (Day 0), plates were placed in the IncuCyte S3 Live-Cell Analysis System (Essen BioScience, Ann Arbor, MI) and whole-well imaged every six hours with phase contrast and green channels (excitation 440-480, emission 504-544) for one week. Single agent trastuzumab treatment groups were treated with trastuzumab (0.1 ng/ml) from 0 to 48 hours (group 1), 24-72 hours (group 2) or 48-96 hours (group 3). For single agent radiation treatment groups, cells were treated with radiation (10 Gy) at 24 hours with the CellRad Dedicated Benchtop Cell Irradiator (Faxitron, Tucson, AZ). For combination treatment groups, cells received trastuzumab (0.1 ng/ml) before, with, or after radiation treatment (10 Gy) as detailed in Figure 5.1a. Each treatment group has 24 wells of replicates. The experiment was performed three times.

5.2.4.2 Experiment 2: Quantifying radiation + trastuzumab combination effects

BT474-GFP, SKBR3-GFP or MDA-MB-231-GFP cells were plated in 96-well plates at 5,000 cells/well. 24 hours later (Day 0), cells were treated with either 0.1% saline, trastuzumab (0.1 ng/ml), or radiation (5 or 10 Gy) for control and single agent treatment groups. Combination groups received both trastuzumab (0.1 ng/ml) and

radiation (5 or 10 Gy) on Day 0 (Figure 5.1b). Plates were placed in the IncuCyte S3 Live-Cell Analysis System (Essen BioScience, Ann Arbor, MI) and whole-well imaged every six hours with phase contrast and green channels (excitation 440-480, emission 504-544) for one week. Each treatment group has 30 wells of replicates. Experiments were performed three times.

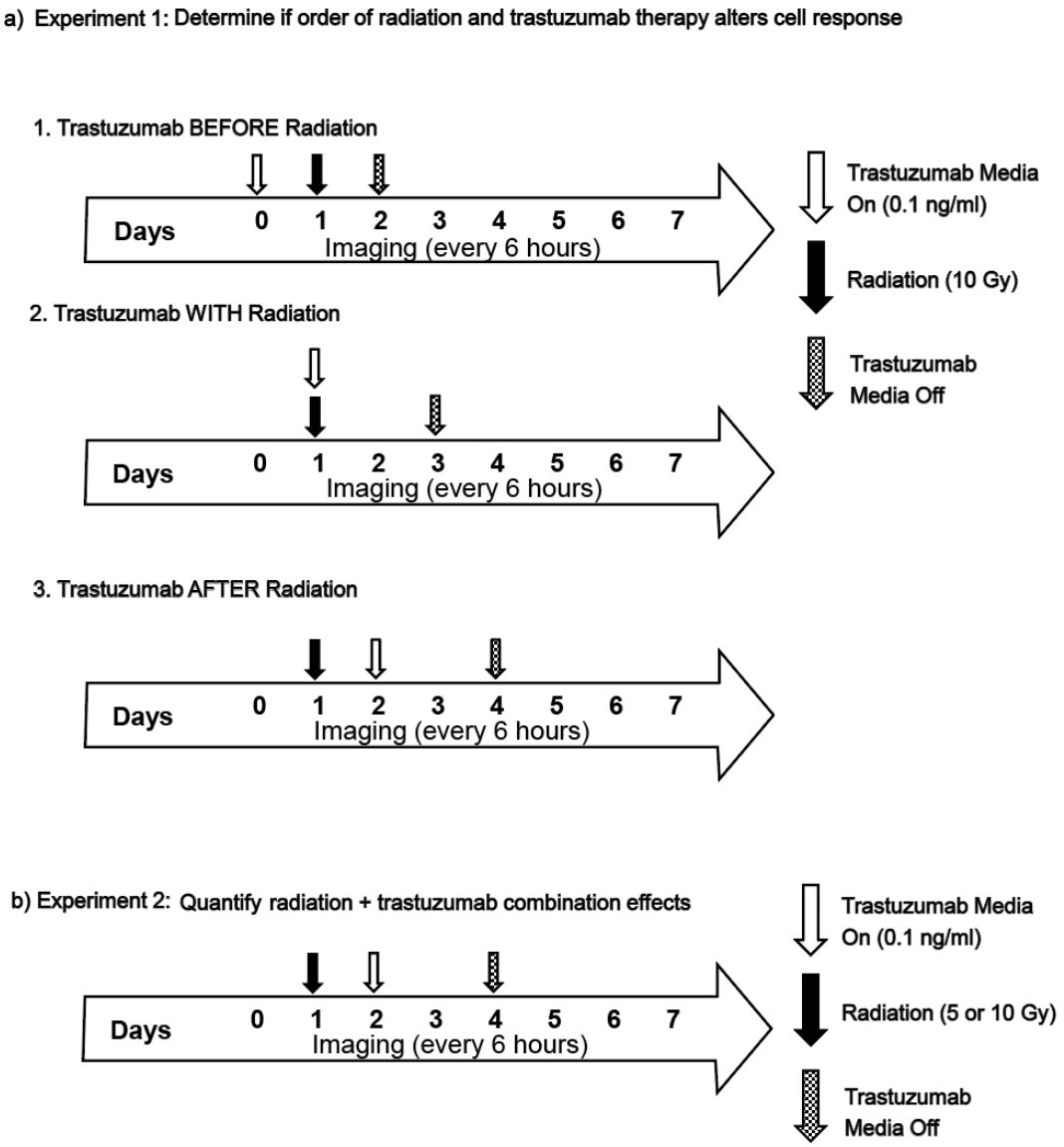

Figure 5.1: Treatment plans for *in vitro* experiments. a) Cells were treated with either trastuzumab (0.1 ng/ml) from 0-48 hours (1, before radiation), 24-72 hours (2, with radiation) or 48-96 hours (3, after radiation). All groups received radiation (10 Gy) at 24 hours. All groups were imaged every 6 hours for seven days. b) Cells were treated with trastuzumab (0.1 ng/ml) and radiation (5 or 10 Gy) at the start of the experiment (Day 0). Trastuzumab was removed 48 hours later. Cells were imaged every six hours for seven days.

5.2.5 Image Analysis

Images were analyzed using the IncuCyte S3 Live-Cell Analysis System (Essen BioScience, Ann Arbor, MI) to segment green fluorescent objects (cell counts). Background signal was estimated in 100 μm segments and subtracted from the image. Edgse of clumped cells were determined at the dimmest point between two objects. Objects greater than 1000 μm^2 were filtered out of analysis. Cell growth was normalized to initial seeding density (0 hours).

5.2.6 Bliss Interaction Index Calculation

The Bliss Interaction Index [215] was used to determine effects of combination radiation and trastuzumab treatment *in vitro*. To calculate the effects of radiation (*A*), trastuzumab (*B*) and combination treatment *(AB*) compared to the control (*C*), let (*f*) represent the difference in normalized cell growth (*N*):

$$(1) \qquad f_i = \frac{N_C - N_i}{N_C} \quad i = A, B, AB$$

The Bliss Interaction Index (I) can be calculated by Eq. (2):

$$(2) \qquad I = f_{AB} - f_A - f_B + f_A f_B$$

and the value of *I* determines the effect of combination therapy:

$$(3) \qquad I = \begin{cases} Synergistic & I > 0 \\ Additive & I = 0 \\ Antagonistic & I < 0 \end{cases}$$

5.2.7 Animal Procedures

All procedures were approved by our institution's animal care and use committee. Female nude athymic mice (N = 46) were purchased from The Jackson Laboratory (Bar

Harbor, ME) at 3-4 weeks of age. Mice were then subcutaneously implanted with a 0.72 mg, 60-day release, 17β-estradiol pellet (Innovative Research of America, Sarasota, FL) in the nape of the neck. One day later, 10^7 BT474 cells were implanted subcutaneously in 100 μl of serum-free IMEM media with 30% growth factor-reduced Matrigel. Tumors were grown to approximately 250 mm^3 (8-10 weeks) and entered into the study. Animals were randomly sorted into treatment groups: 1) Control: 100 μl saline on Days 0, 3 (N = 6), 2) Trastuzumab alone: 10 mg/kg on Days 0, 3 (N = 7), 3) Radiation 5 Gy alone: Day 0 (N = 6) + 100 μl saline on Day 3, 4) Radiation 10 Gy alone: Day 0 (N = 5) + 100 μl saline on Day 3, 5) Radiation 5 Gy on Day 0 + Trastuzumab 10 mg/kg on Days 0, 3 (N = 5), 6) Radiation 10 Gy on Day 0 + Trastuzumab 10 mg/kg on Days 0, 3 (N = 5). Trastuzumab and saline were administered *via* intraperitoneal (IP) injection. Radiation treatments were given with the MultiRad 350 Irradiation System (Faxitron, Tucson, AZ). Tumor measurements were taken three times per week using calipers for four weeks at which point mice were euthanized. Mice in the immunohistochemistry cohort were divided into three treatment groups: 1) Radiation 5 Gy on Day 0 (N = 4) + 100 μl saline on Day 3, 2) Trastuzumab 10 mg/kg on Days 0, 3 (N = 4), 3) Radiation 5 Gy on Day 0 + Trastuzumab 10 mg/kg on Days 0, 3 (N = 4). Tumor growth was measured three times with calipers for one week at which point mice were euthanized and tumors were extracted. One hour prior to sacrifice, mice were intravenously injected with 60 mg/kg of pimonidazole (Hypoxyprobe, Inc., Burlington, MA) in 100 μl of saline. Tumors were cut at the longest cross-section and half was fixed in 10% neutral buffered formalin (Fisher Scientific International Inc., Pittsburgh, PA) for 48 hours where it was then placed in 70% ethanol.

5.2.8 Immunohistochemistry

Formalin fixed tumor sections were embedded in paraffin and sliced into 4 μM sections. Sections were stained for hematoxylin and eosin (H&E), mouse anti-CD31, mouse anti-α-smooth muscle actin (α-SMA, Abcam, Cambridge, UK), mouse anti-CD45 (Invitrogen, Carlsbad, CA) and anti-pimonidazole (Hypoxyprobe, Inc., Burlington, MA). Immuno-stained slides were scanned (20×, 0.495 μm/pixel) with the Aperio ScanScope (Leica Microsystems, Wetzlar, Germany). Regions of necrosis were determined using manual segmentation. All other stains were segmented based on thresholds determined from positive and negative controls using in house MATLAB (MathWorks Inc., Natick, MA) routines. Images were converted to grayscale for registration to the corresponding tumor H&E. Then, transformations consisting of translation, rotation and scale (similarity) based on intensity were applied. A viable tissue mask was defined as total tumor area minus necrotic area. Inflammation (CD45), hypoxia (pimonidazole), and apoptosis (caspase3) were defined as the percent of positive stain per viable tissue area. Microvessel density (CD31) and vascular smooth muscle coverage (α-SMA) were calculated as the number of vessels per mm^2 of tumor tissue. The vessel maturation index [40] was evaluated as the ratio of α-SMA coverage to microvessel density. All codes are available upon request.

5.2.9 Statistical Analysis

Statistical analysis was conducted using MATLAB (MathWorks Inc., Natick, MA). A two-way analysis of variance (ANOVA), adjusting for multiple comparisons with Dunn's, was used to determine longitudinal differences in order of dosing experiments. All *in vitro* data is presented as mean ± 95% confidence interval with $P < 0.05$ indicating significance. Statistical differences between *in vivo* tumor growth at each

time point and *ex vivo* immunohistochemistry samples were determined using a nonparametric Wilcoxon rank sum test. All *in vivo* and *ex vivo* data is presented as mean ± standard error with $P < 0.05$ indicating significance. The Friedman's test adjusting for multiple comparisons with Dunn's was used to assess longitudinal changes in tumor growth between treatment groups.

5.3 RESULTS

5.3.1 HER2 expression in BT474, SKBR3 and MDA-MB-231 cell lines

Quantification of HER2 protein expression in BT474, SKBR3, and MDA-MB-231 cells confirmed reported HER2 status in each cell line (Figure 5.2). Western blot revealed visible bands of HER2 protein in BT474 and SKBR3 HER2+ cell lines at 185 kDa, and showed little to no expression in MDA-MB-231 cells, a HER2- cell line (Figure 5.2a). β-actin was used as an internal control for normalization of HER2 expression. Ratios of HER2:β-actin in BT474 and SKBR3 cells were 1.41 and 1.46, respectively, confirming HER2 overexpression. MDA-MB-231 cells had a HER2:β-actin ratio of 0.08, confirming no HER2 overexpression (Figure 5.2b).

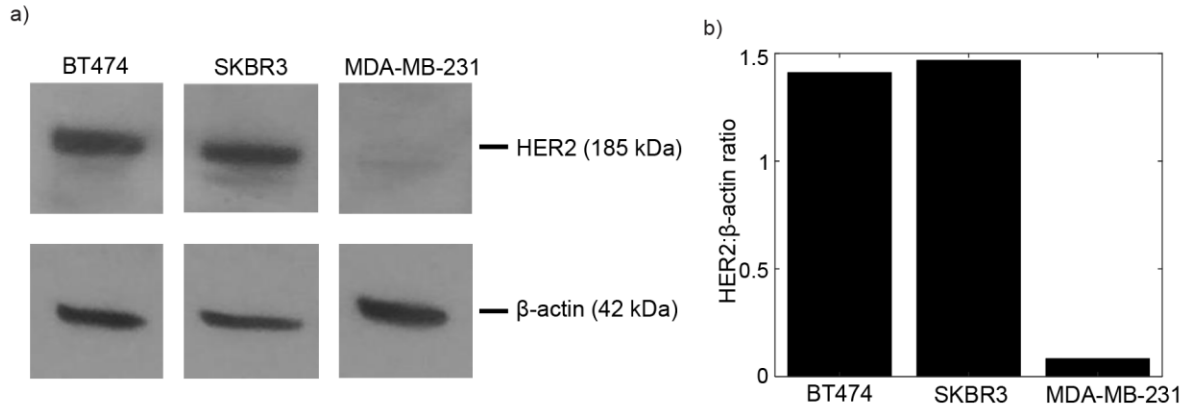

Figure 5.2: HER2 quantification in BT474, SKBR3 and MDA-MB-231 cells. a) Expression of HER2 protein (185 kDa) in each cell line. β-actin (42 kDa) was used as an internal control. Visible protein bands are seen in the BT474 and SKBR3 HER2+ cell lines while MDA-MB-231 shows little to no expression. B) HER2:β-actin ratio in each cell line. BT474 and SKBR3 cells have ratios of 1.41 and 1.46, respectively. MDA-MB-231 has a ratio of 0.08, confirming no HER2 amplification.

5.3.2 Order of radiation and trastuzumab therapy does not affect cell death response *in vitro*

Cells were administered single agent trastuzumab controls from 24-48 hours, 24-72 hours and 48-96 hours. No significant differences were observed between these groups (Figure 5.3). In combination regimens, cells were treated with trastuzumab (0.1 ng/ml) 24 hours before radiation (10 Gy) treatment, at the same time as radiation treatment, and 24 hours after radiation. No significant differences were seen in cell growth over time when comparing trastuzumab treatment before with treatment at the same time ($P = 1.00$) or treatment after ($P = 0.98$). Additionally, treatment with trastuzumab at the same time as radiation did not alter cell response over time compared to treatment after radiation ($P = 0.93$) (Figure 5.3). From these results, it was determined that order of dosing did not affect cell response to therapy and further experiments were conducted administering trastuzumab and radiation at the same time (Figure 5.1b).

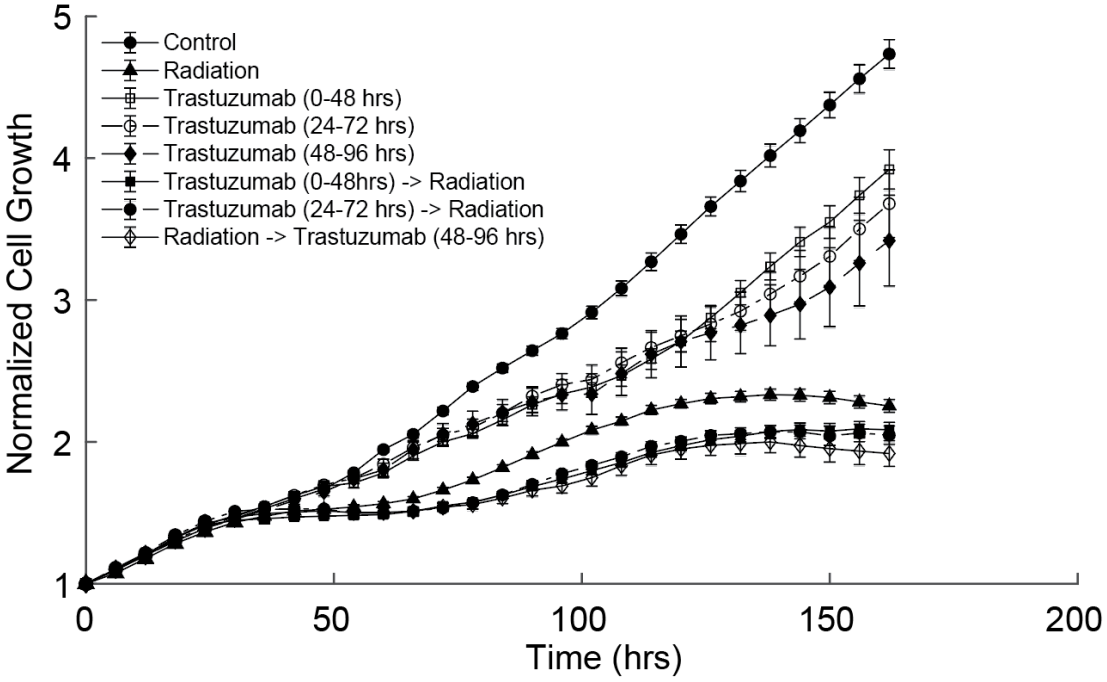

Figure 5.3: Differences in BT474 cell growth with trastuzumab given before, at the same time, and after radiation therapy. Treatment with trastuzumab before radiation did not significantly alter cell response to therapy compared to treatment of trastuzumab at the same time (P = 1.00) or treatment after radiation (P = 0.98). Treatment with trastuzumab at the same time did not significantly alter cell response to therapy compared to treatment after radiation (P = 0.93). Altering the order of dosing of trastuzumab and radiation did not alter cell response to treatment *in vitro*.

5.3.3 Quantification of longitudinal cell growth after combination therapy reveals additive effects *in vitro*

Figure 5.4 displays BT474, SKBR3 and MDA-MB-231 cell proliferation after being treated with trastuzumab (0.01 ng/ml), radiation (5 or 10 Gy), or combination treatment over one week. No significant differences were observed through time in MDA-MB-231 cell proliferation between the control and trastuzumab single agent treatment groups (P = 0.88, panels e and f of Figure 5.4), which is to be expected in a

HER2- cell line not responsive with trastuzumab. There were also no significant differences in proliferation between the radiation single agent or combination treatment groups as expected ($P = 0.84$, Figure 5.4e and $P = 0.80$, Figure 5.4f). Eq. (2) was used to calculate the Bliss Interaction Index of combination treatment effects from radiation and trastuzumab. Figure 5.5 displays interaction index over time for each treatment group in Figure 5.4. No group had an interaction index that fell significantly above or below 0 at any time point ($P < 0.05$), indicating additive treatment effects.

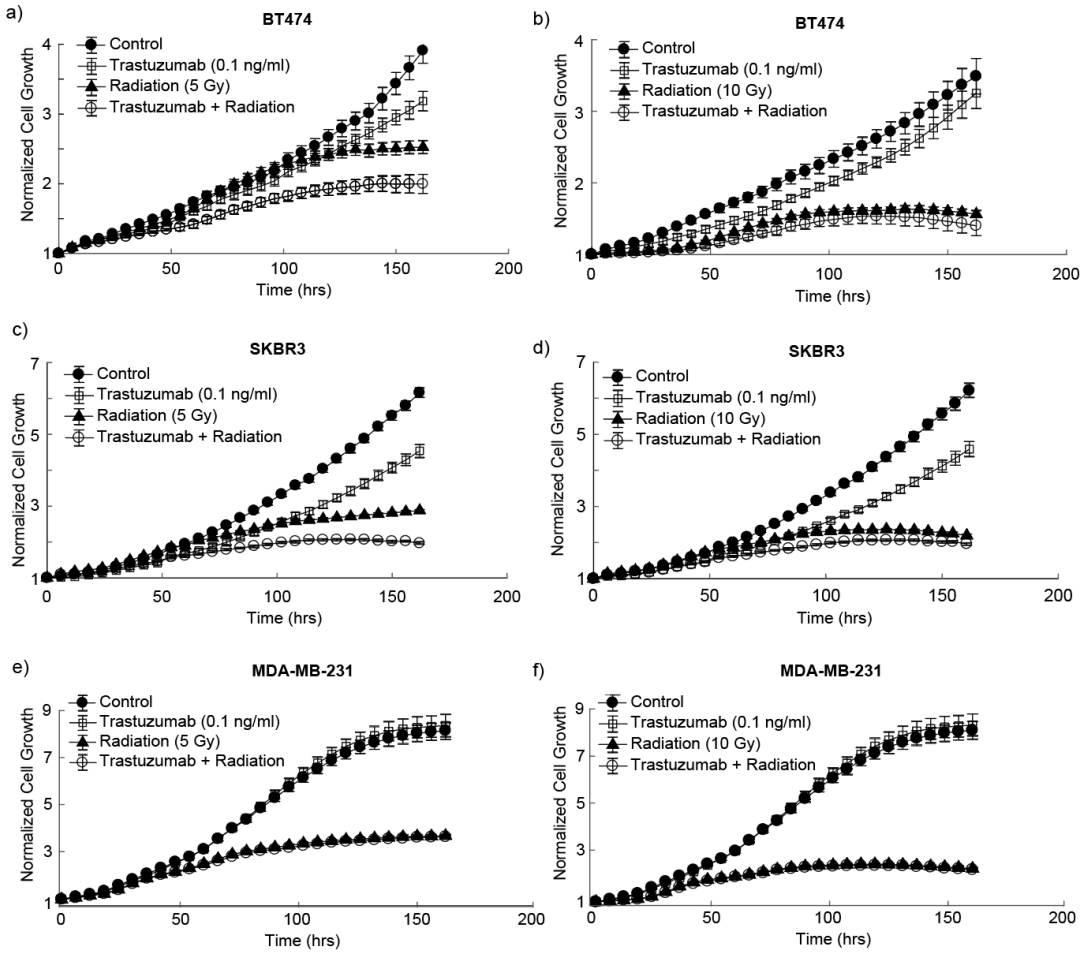

Figure 5.4: Cell proliferation over one week after radiation, trastuzumab or combination treatment. All trastuzumab single agent and combination groups were treated with 0.1 ng/ml of trastuzumab from 0-48 hours. All radiation single agent and combination groups were treated with 5 or 10 Gy radiation on Day 0. Graphs display proliferation of: a) BT474 cells after trastuzumab, 5 Gy radiation and combination treatment, b) BT474 cells after trastuzumab, 10 Gy radiation and combination treatment, c) SKBR3 cells after trastuzumab, 5 Gy radiation and combination treatment, d) SKBR3 cells after trastuzumab, 10 Gy radiation and combination treatment, e) MDA-MB-231 cells after trastuzumab, 5 Gy radiation and combination treatment, f) MDA-MB-231 cells after trastuzumab, 10 Gy radiation and combination treatment. No significant difference was observed in control MDA-MB-231 cell proliferation and cells treated with single agent trastuzumab ($P = 0.88$, e & f). No significant difference in cell proliferation was observed between cells treated with single agent radiation and cells treated with combination treatment ($P = 0.84$, e & $P = 0.80$, f).

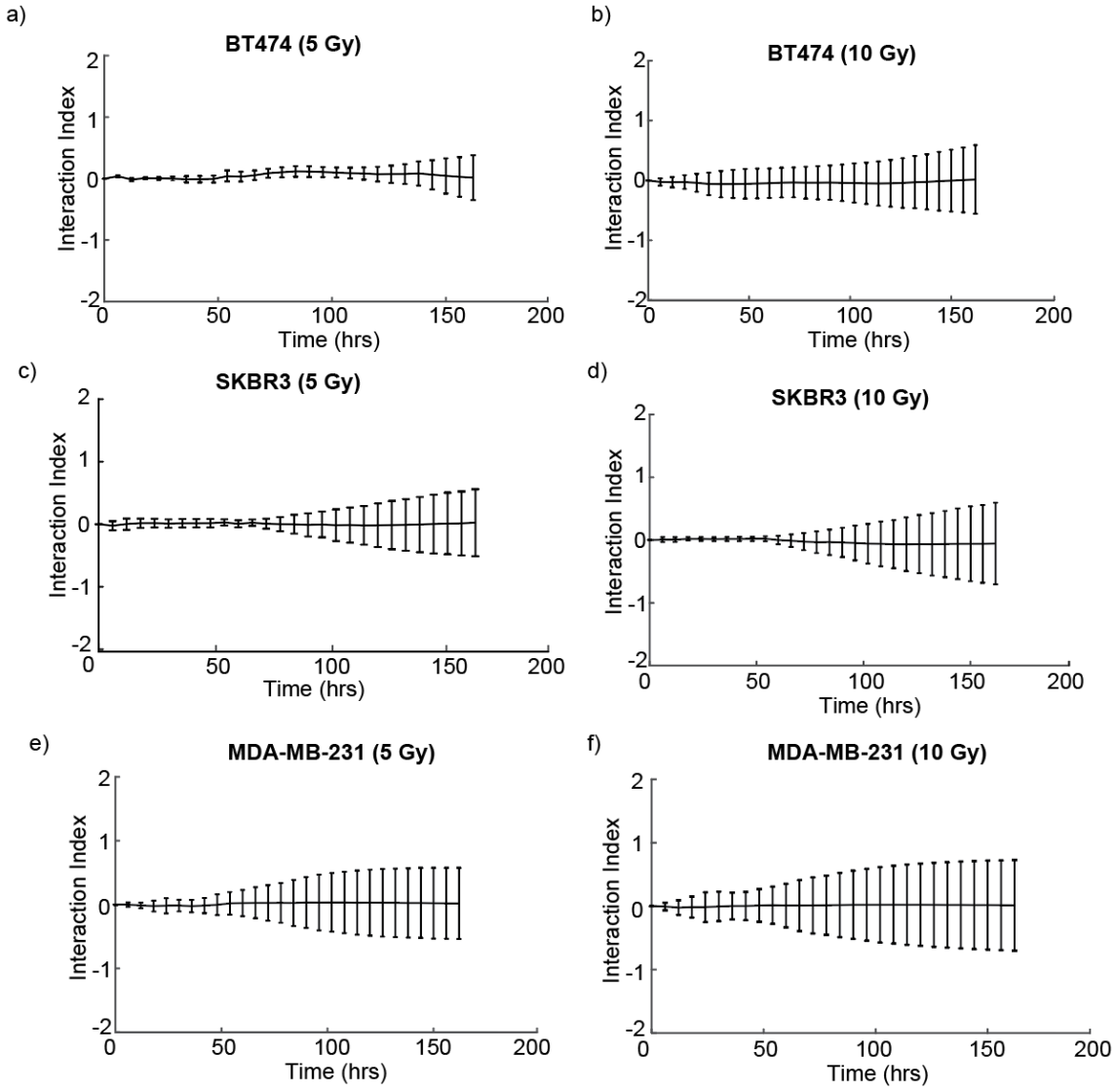

Figure 5.5: Bliss interaction index calculated per time point over one week of treatment. All groups were treated with 0.01 ng/ml of trastuzumab. Graphs display interaction index of a) BT474 cells, 5 Gy radiation + trastuzumab, b) BT474 cells, 10 Gy radiation + trastuzumab, c) SKBR3 cells, 5 Gy radiation + trastuzumab, d) SKBR3 cells, 10 Gy radiation + trastuzumab, e) MDA-MB-231 cells, 5 Gy radiation + trastuzumab and f) MDA-MB-231 cells, 10 Gy radiation + trastuzumab. No group had an interaction index significantly above or below 0 at any time point, indicating additive treatment affects.

5.3.4 Tumor size decreases faster with combination therapy than either single therapy *in vivo*

Figure 5.6a displays tumor volume changes in response to trastuzumab, radiation and combination regimens over four weeks. Mice treated with 10 Gy radiation had a significantly greater decrease in tumor size than mice treated with 5 Gy radiation over time ($P < 0.001$). However, mice treated with trastuzumab + 5 Gy radiation revealed no statistical differences in tumor response over time compared to mice treated with trastuzumab + 10 Gy radiation ($P = 0.56$). Mice treated with trastuzumab + 5 Gy radiation had significantly smaller tumors than mice treated with trastuzumab alone on day 7 onwards ($P < 0.05$) with the exception of day 9 ($P = 0.11$) (Figure 5.6b). Mice treated with trastuzumab + 5 Gy radiation had significantly smaller tumors than mice treated with 5 Gy alone on day 2 onwards ($P < 0.05$) with the exception of day 25 ($P = 0.25$) (Figure 5.6c). Mice treated with trastuzumab + 5 Gy radiation had significantly smaller tumors than mice treated with 10 Gy radiation on days 2-17 ($P < 0.05$) (Figure 5.6d).

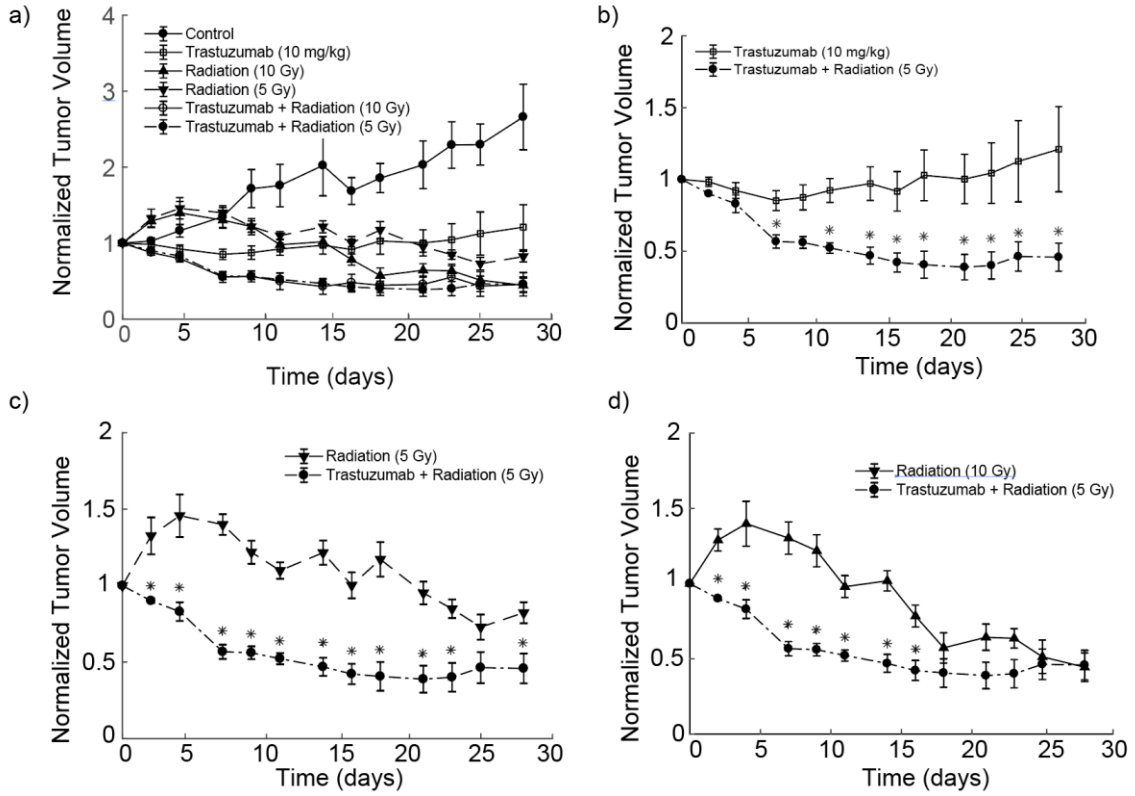

Figure 5.6: *In vivo* tumor growth response to single agent and combination trastuzumab and radiation therapy. All mice were treated with radiation on Day 0 and trastuzumab on Days 0 and 3. a) Displays all groups. There was a significant difference between groups treated with single agent 5 Gy and single agent 10 Gy radiation ($P < 0.001$). There was no significant difference when adding trastuzumab to the regimen; Trastuzumab + Radiation (10 Gy) vs. Trastuzumab + Radiation (5 Gy) ($P = 0.56$). b) Displays trastuzumab single agent therapy compared to trastuzumab + 5 Gy radiation. Significant differences between tumor response are observed on days 7-28, excluding day 9. c) Displays single agent radiation therapy (5 Gy) compared to trastuzumab + 5 Gy radiation. Significant differences are observed in tumor response on days 2-28, excluding day 25. d) Displays single agent radiation (10 Gy) compared to trastuzumab + 5 Gy radiation. Significant differences are observed in tumor response on days 2-17.

5.3.5 Tumor immune infiltration was higher in mice that received trastuzumab treatment

Figure 5.7a displays representative images of CD45+ staining in mice treated with radiation (5 Gy) on Day 0, trastuzumab (10 mg/kg) on Days 0 and 3, or combination radiation and trastuzumab. Mice treated with trastuzumab alone had significantly higher CD45+ staining (2.63 ± 0.73%) than mice treated with radiation alone (0.77 ± 0.13%) ($P = 0.03$) on Day 7. Mice treated with combination therapy also had significantly higher CD45+ staining (2.48 ± 0.44%) than mice treated with radiation alone ($P = 0.03$). No significant differences were observed between mice treated with trastuzumab alone and combination treatment ($P = 1.00$) (Figure 5.7b). No significant differences were observed between treatment groups ($P > 0.05$) in percent pimonidazole or vascular maturation index (Figure 5.8).

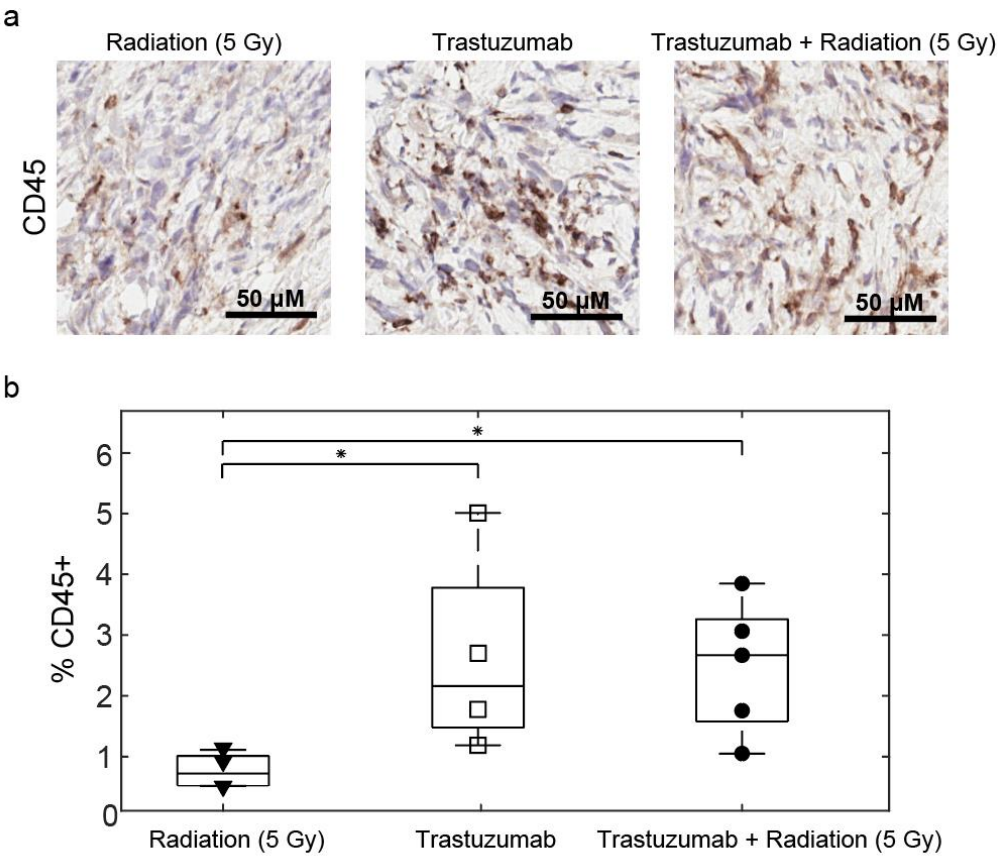

Figure 5.7: Percent CD45+ in single agent radiation, trastuzumab and combination treated tumors on Day 7. All radiation single agent and combination groups were treated with 5 Gy of radiation on Day 0. All trastuzumab single agent and combination groups were treated with 10 mg/kg of trastuzumab on Days 0 and 3. a) Representative images of CD45 staining in single agent and combination treatment groups. b) Percent CD45+ staining from central slice of tumors in single agent and combination treatment groups, revealing significant increases in CD45+ in trastuzumab single agent and trastuzumab + radiation (5 Gy) compared to radiation alone ($P = 0.03$). No significant difference was seen in mice treated with single agent trastuzumab and trastuzumab + radiation ($P = 1.00$).

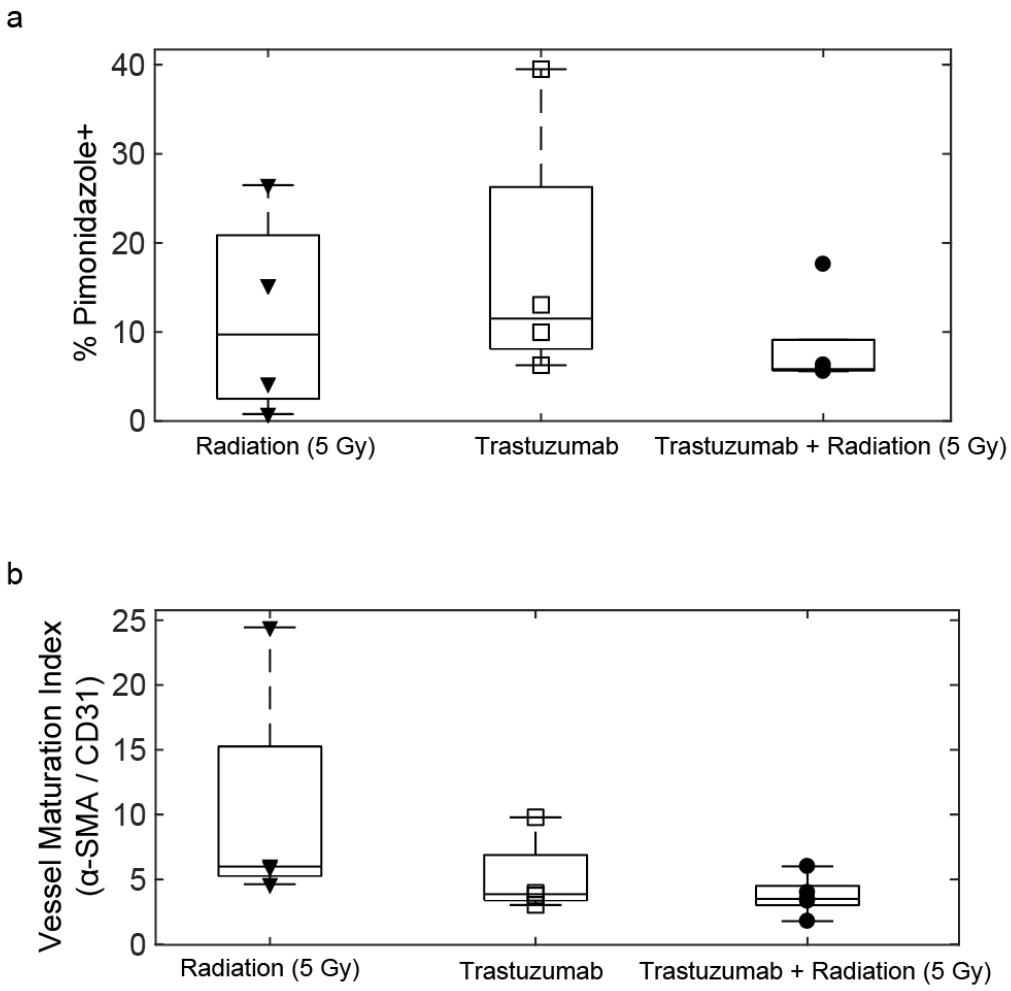

Figure 5.8: Hypoxia and vascular staining in single agent radiation, trastuzumab and combination treated tumors. All radiation single agent and combination groups were treated with 5 Gy of radiation on Day 0. All trastuzumab single agent and combination groups were treated with 10 mg/kg of trastuzumab on Days 0 and 3. a) Percent pimonidazole staining revealing no significant differences between treatment groups ($P > 0.05$). B) Vascular maturation index revealing no significant differences between treatment groups ($P > 0.05$).

5.4 DISCUSSION

Trastuzumab and radiation are commonly used as adjuvant therapies in clinical treatment of HER2+ breast cancer. Radiation therapy can reduce recurrence rates in patients by eradicating remaining cancer cells after surgical removal of tumors, however, HER2+ patients have greater chances of recurrence than HER2- patients [24, 26, 127]. *In vitro* evidence suggests trastuzumab can sensitize HER2+ breast cancer cells to radiation through inhibition of signaling pathways involved in DNA repair mechanisms [27, 131], although, systematic evaluation of the order of therapies and longitudinal data of cell response are limited. This study demonstrates the order of therapy does not alter cell proliferation after treatment and longitudinal treatment effects are additive *in vitro*. *In vivo*, tumors regress faster when treated with combination therapy than either single agent therapy and there is evidence that immune modulation may impact treatment response.

The Bliss Interaction Index calculations (Figure 5.5) revealed additive effects from combination radiation and trastuzumab treatment across all cell types. This contrasts with others who have evaluated cell response to radiation and trastuzumab using end point assays [27, 31]. For example, Liang *et al.* found a synergistic effect from trastuzumab and radiation treatment with BT474 and SKBR3 cells 24 hours after therapy using an ELISA to evaluate apoptosis (cytoplasmic histone-associated DNA fragments) [27]. In their study, cells were pre-incubated with trastuzumab for 16 hours before radiation treatment; however, our results did not indicate pre-treatment with trastuzumab alters cell response to radiation (Figure 3). Rao *et al.* found a similar synergistic effect using SUM-149PT cells treated with a HER2 tyrosine-kinase inhibitor in combination with radiation therapy; though, this study used a longer pre-incubation time with trastuzumab (7 days) and evaluated cell growth two weeks after radiation treatment using a clonogenic assay [31]. Differences in results could arise from the alternate methods

used to detect cell response to treatment and differences in timing of evaluation after treatment. We believe our study accurately quantifies longitudinal cell growth after treatment and provides a better understanding of cellular dynamics after combination treatment than traditional end point assays.

In vivo tumor growth data shows significant differences in longitudinal tumor response between groups that were treated with 5 Gy and 10 Gy of radiation, however, no significant difference in longitudinal tumor response was observed between doses of radiation when trastuzumab was added to the treatment regimen (Figure 5.6a). This finding suggests a smaller dose of radiation could be used in combination with trastuzumab without decreasing efficacy. Additionally, results show a faster rate of tumor regression in groups treated with combination therapy compared to either single therapy (Figure 5.6b-d).

To evaluate if microenvironmental alterations could be impacting treatment response, immune infiltration, hypoxia, and vascular maturation index were evaluated in tumors treated with 5 Gy radiation, trastuzumab and 5 Gy radiation in combination with trastuzumab seven days after treatment. CD45 histology staining revealed an increase in immune infiltration in treatment groups receiving trastuzumab (Figure 5.7b). Previously collected data revealed trastuzumab has the potential to reprogram the immunosuppressive components of the tumor microenvironment and could contribute to anti-tumor responses (Chapter 4). Evaluation of immune cell characterization and impact on tumor regression in this treatment regimen is needed to further elucidate mechanisms contributing to enhanced tumor regression in the combination treatment group. Although no significant differences were shown in hypoxia and vascular maturation index, previous studies using longitudinal imaging have revealed trastuzumab can reduce hypoxia and increase vascular perfusion [21, 208]. It is possible by employing longitudinal imaging

methods, windows of heightened oxygenation could be revealed and alternate order of dosing could enhance treatment response *in vivo*.

Limitations of this study include the lack of longitudinal data evaluating microenvironmental changes corresponding with tumor growth dynamics. As previously discussed in Chapter 4, immuno-PET imaging, is an alternative method that could longitudinally evaluate immune infiltration after treatment. ^{18}F-Fluoromisonidazole positron emission tomography is one method used to monitor tumor oxygenation levels and dynamic contrast enhanced magnetic resonance imaging is an alternative method to quantitatively assess vascularity. Neither of these methods would allow for histological validation at every time point, however, they would offer finely time resolved data of tumor status over the course of treatment. This study used a single dose of radiation and provided preliminary data showing a lesser dose of radiation could be used in combination with trastuzumab to achieve the same therapeutic efficacy as a higher dose of radiation, however, additional studies should be conducted evaluating efficacy with a clinical treatment regimen which uses fractionated dosing. Additional trastuzumab treatment doses were investigated for the *in vitro* experiments in this study. Doses higher than 0.01 ng/ml exhibited greater decreases in cell proliferation in single agent treatment groups, however, did not affect combination treatment response. Doses lower than 0.01 ng/ml had no significant effect on HER2+ cell growth, which is not biologically observed *in vivo*; therefore, 0.01 ng/ml was chosen as the appropriate treatment condition. It is possible using a higher seeding density would allow for evaluation of cell proliferation with a higher trastuzumab dose, although when cells become confluent, the IncuCyte system is less accurate in quantifying cell number [212].

5.5 CONCLUSION

This study demonstrates longitudinal assessment of growth dynamics can result in different conclusions than end point assays and differences in methodologies should be taken into consideration when evaluating cellular response to treatment. Furthermore, this study yielded preliminary data that using trastuzumab in combination with radiation has the potential to decrease the dose of radiation administered without affecting therapeutic efficacy. Histology data revealed treatment with trastuzumab increased immune infiltration compared to radiation alone. Further assessment of immune changes in single agent and combination regimens could identify mechanistic reasoning for differences in therapeutic efficacies.

Chapter 6: Conclusion

6.1 Summary

The goal of this dissertation was to characterize treatment-induced alterations of the tumor microenvironment for the use of guiding future combination regimens that will optimize treatment response in cancer. Specifically, the aims of this work achieved an improved understanding of NF-κB signal dynamics and gene expression for investigating small molecule therapies inhibiting the NF-κB transcription factor (Chapter 3). Secondly, revealed a mechanistic understanding of anti-HER2 induced vascular changes and identified windows of reduced immune suppression in HER2+ breast cancer (Chapter 4). Lastly, quantified combination treatment effects of radiation and trastuzumab therapy in HER2+ breast cancer, revealing enhanced tumor regression using combination treatment *in vivo*. The results presented provide valuable insight of how the tumor microenvironment can dictate treatment response and the potential to modulate the tumor microenvironment to enhance therapeutic efficacy.

6.2 Future Directions

6.2.1 NF-κB Targeted Therapies

The experimental data collected in Chapter 3 indicates that pathway analyses are needed to accurately assess the effects of targeted drugs. Further studies should be focused in high throughput analyses of gene expression patterns. Analyzing which genes are activated early vs. late would increase understanding of inflammatory processes in cancer. Additionally, the gene expression patterns could identify genes that have steady state expression patterns vs. fluctuating expression patterns; furthering understanding of

cellular decision making in disease. This dataset is currently deposited on the NIH Sequence Read Archive.

6.2.2 Immune Response in HER2+ Breast Cancer

Chapter 4 evaluated innate immune alterations after treatment with trastuzumab. Further studies should evaluate immune infiltration after trastuzumab treatment in a mouse with a full immune system including T-cells. This would be valuable to determine any differences in trastuzumab vascular remodeling as well as conducting studies to guide immunotherapy treatment regimens. This work will be continued under the direction of Dr. Anna Sorace at the University of Alabama – Birmingham. Additionally, further systematic evaluation of cytokines contributing to the reprogramming of macrophages towards an M1 phenotype would be beneficial in identifying potential small molecule therapies that could be used in cancer to reprogram immunosuppressive innate immune components of the tumor microenvironment.

6.2.3 Radiation and Trastuzumab Combination Treatment

The results detailed in Chapter 5 revealed the potential of trastuzumab to increase the efficacy of radiation therapy in a combination regimen. Further studies should investigate this phenomenon using a dosing regimen similar to that in the clinic (fractionated radiation), as well as if order of trastuzumab and radiation effect treatment response *in vivo*. Furthermore, longitudinal analysis of vascular and immune alterations coinciding with therapeutic dosing could identify mechanisms of enhanced tumor regression and possible windows of radiosensitization.

References

1. Hanahan D, Weinberg RA (2000) The Hallmarks of Cancer. Cell 100:57–70

2. Hanahan D, Weinberg RA (2011) Hallmarks of Cancer: The Next Generation. Cell 144:646–674

3. Adjei IM, Blanka S (2015) Modulation of the Tumor Microenvironment for Cancer Treatment: A Biomaterials Approach. J Funct Biomater 6:81–103

4. Hinshaw DC, Shevde LA (2019) The Tumor Microenvironment Innately Modulates Cancer Progression. Cancer Res. https://doi.org/10.1158/0008-5472.CAN-18-3962

5. Giancotti FG (2014) Deregulation of Cell Signaling in Cancer. FEBS Lett 588:2558–2570

6. Hanahan D, Folkman J (1996) Patterns and Emerging Mechanisms of the Angiogenic Switch during Tumorigenesis. Cell 86:353–364

7. Helmlinger G, Yuan F, Dellian M, Jain RK (1997) Interstitial pH and pO 2 gradients in solid tumors in vivo : High-resolution measurements reveal a lack of correlation. Nat Med 3:177–182

8. Engblom C, Pfirschke C, Pittet MJ (2016) The role of myeloid cells in cancer therapies. Nature Reviews Cancer 16:447–462

9. Schmid MC, Varner JA (2010) Myeloid Cells in the Tumor Microenvironment: Modulation of Tumor Angiogenesis and Tumor Inflammation. Journal of Oncology. https://doi.org/10.1155/2010/201026

10. Poh AR, Ernst M (2018) Targeting Macrophages in Cancer: From Bench to Bedside. Front Oncol. https://doi.org/10.3389/fonc.2018.00049

11. Medina PJ, Goodin S (2008) Lapatinib: A dual inhibitor of human epidermal growth factor receptor tyrosine kinases. Clinical Therapeutics 30:1426–1447

12. Schettino C, Bareschino MA, Ricci V, Ciardiello F (2008) Erlotinib: an EGF receptor tyrosine kinase inhibitor in non-small-cell lung cancer treatment. Expert Rev Respir Med 2:167–178

13. (2018) Angiogenesis and Angiogenesis Inhibitors to Treat Cancer. In: Cancer.Net. https://www.cancer.net/navigating-cancer-care/how-cancer-treated/personalized-and-targeted-therapies/angiogenesis-and-angiogenesis-inhibitors-treat-cancer. Accessed 17 Oct 2019

14. Dudley ME, Wunderlich JR, Shelton TE, Even J, Rosenberg SA (2003) Generation of Tumor-infiltrating Lymphocyte Cultures for Use in Adoptive Transfer Therapy for Melanoma Patients. Journal of Immunotherapy 26:332–342

15. Callahan MK, Wolchok JD (2013) At the Bedside: CTLA-4- and PD-1-blocking antibodies in cancer immunotherapy. J Leukoc Biol 94:41–53

16. Dougherty GJ, Dougherty ST (2009) Exploiting the tumor microenvironment in the development of targeted cancer gene therapy. Cancer Gene Therapy 16:279–290

17. Behar M, Barken D, Werner SL, Hoffmann A (2013) The Dynamics of Signaling as a Pharmacological Target. Cell 155:448–461

18. DiDonato JA, Mercurio F, Karin M (2012) NF-κB and the link between inflammation and cancer. Immunol Rev 246:379–400

19. Berger SI, Iyengar R (2011) Role of systems pharmacology in understanding drug adverse events. Wiley Interdiscip Rev Syst Biol Med 3:129–135

20. Behar M, Hoffmann A (2010) Understanding the Temporal Codes of Intra-cellular Signals. Curr Opin Genet Dev 20:684–693

21. Sorace AG, Quarles CC, Whisenant JG, Hanker AB, McIntyre JO, Sanchez VM, Yankeelov TE (2016) Trastuzumab improves tumor perfusion and vascular delivery of cytotoxic therapy in a murine model of HER2+ breast cancer: preliminary results. Breast Cancer Res Treat 155:273–284

22. Izumi Y, Xu L, di Tomaso E, Fukumura D, Jain RK (2002) Tumour biology: Herceptin acts as an anti-angiogenic cocktail. Nature 416:279–280

23. Nahta R, Esteva FJ (2006) HER2 therapy: molecular mechanisms of trastuzumab resistance. Breast Cancer Res 8:215

24. NCCN Guidelines for Patients® | Invasive Breast Cancer. https://www.nccn.org/patients/guidelines/breast-invasive/46/index.html. Accessed 29 Oct 2019

25. (2011) Effect of radiotherapy after breast-conserving surgery on 10-year recurrence and 15-year breast cancer death: meta-analysis of individual patient data for 10 801 women in 17 randomised trials. Lancet 378:1707–1716

26. Gonzalez-Angulo AM, Litton JK, Broglio KR, et al (2009) High risk of recurrence for patients with breast cancer who have human epidermal growth factor receptor 2-positive, node-negative tumors 1 cm or smaller. J Clin Oncol 27:5700–5706

27. Liang K, Lu Y, Jin W, Ang KK, Milas L, Fan Z (2003) Sensitization of breast cancer cells to radiation by trastuzumab. Mol Cancer Ther 2:1113–1120

28. Pietras RJ, Poen JC, Gallardo D, Wongvipat PN, Lee HJ, Slamon DJ (1999) Monoclonal antibody to HER-2/neureceptor modulates repair of radiation-induced DNA damage and enhances radiosensitivity of human breast cancer cells overexpressing this oncogene. Cancer research 59:1347–1355

29. Guo G, Wang T, Gao Q, Tamae D, Wong P, Chen T, Chen W-C, Shively JE, Wong JY, Li JJ (2004) Expression of ErbB2 enhances radiation-induced NF- κ B activation. Oncogene 23:535–545

30. Hou J, Zhou Z, Chen X, et al (2016) HER2 reduces breast cancer radiosensitivity by activating focal adhesion kinase in vitro and in vivo. Oncotarget 7:45186–45198

31. Rao GS, Murray S, Ethier SP (2000) Radiosensitization of human breast cancer cells by a novel ErbB family receptor tyrosine kinase inhibitor. International Journal of Radiation Oncology*Biology*Physics 48:1519–1528

32. Hayden MS, Ghosh S (2012) NF-κB, the first quarter-century: remarkable progress and outstanding questions. Genes Dev 26:203–234

33. Lawrence T (2009) The Nuclear Factor NF-κB Pathway in Inflammation. Cold Spring Harb Perspect Biol. https://doi.org/10.1101/cshperspect.a001651

34. Xia L, Tan S, Zhou Y, et al (2018) Role of the NFκB-signaling pathway in cancer. Onco Targets Ther 11:2063–2073

35. Sun S-C, Chang J-H, Jin J (2013) Regulation of NF-κB in Autoimmunity. Trends Immunol 34:282–289

36. Hayden MS, Ghosh S (2004) Signaling to NF-κB. Genes Dev 18:2195–2224

37. Basak S, Kim H, Kearns JD, et al (2007) A fourth IkappaB protein within the NF-kappaB signaling module. Cell 128:369–381

38. Madge LA, May MJ (2010) Classical NF-κB Activation Negatively Regulates Noncanonical NF-κB-dependent CXCL12 Expression. Journal of Biological Chemistry 285:38069–38077

39. Sun S-C (2011) Non-canonical NF-κB signaling pathway. Cell Res 21:71–85

40. Barnes SE, Wang Y, Chen L, Molinero LL, Gajewski TF, Evaristo C, Alegre M-L (2015) T cell-NF-κB activation is required for tumor control in vivo. J Immunother Cancer. https://doi.org/10.1186/s40425-014-0045-x

41. Scheidereit C (2006) IkappaB kinase complexes: gateways to NF-kappaB activation and transcription. Oncogene 25:6685–6705

42. Brown K, Park S, Kanno T, Franzoso G, Siebenlist U (1993) Mutual regulation of the transcriptional activator NF-kappa B and its inhibitor, I kappa B-alpha. Proc Natl Acad Sci U S A 90:2532–2536

43. Sun SC, Ganchi PA, Ballard DW, Greene WC (1993) NF-kappa B controls expression of inhibitor I kappa B alpha: evidence for an inducible autoregulatory pathway. Science 259:1912–1915

44. Liu T, Zhang L, Joo D, Sun S-C (2017) NF-κB signaling in inflammation. Signal Transduct Target Ther 2:17023

45. Ham B, Fernandez MC, D'Costa Z, Brodt P (2016) The diverse roles of the TNF axis in cancer progression and metastasis. Trends Cancer Res 11:1–27

46. Lewis AM, Varghese S, Xu H, Alexander HR (2006) Interleukin-1 and cancer progression: the emerging role of interleukin-1 receptor antagonist as a novel therapeutic agent in cancer treatment. J Transl Med 4:48

47. Xia Y, Shen S, Verma IM (2014) NF-κB, an active player in human cancers. Cancer Immunol Res 2:823–830

48. Biswas DK, Shi Q, Baily S, Strickland I, Ghosh S, Pardee AB, Iglehart JD (2004) NF-κB activation in human breast cancer specimens and its role in cell proliferation and apoptosis. Proc Natl Acad Sci U S A 101:10137–10142

49. Sakamoto K, Maeda S, Hikiba Y, Nakagawa H, Hayakawa Y, Shibata W, Yanai A, Ogura K, Omata M (2009) Constitutive NF-κB Activation in Colorectal Carcinoma Plays a Key Role in Angiogenesis, Promoting Tumor Growth. Clin Cancer Res 15:2248–2258

50. Bredel M, Scholtens DM, Yadav AK, et al (2011) NFKBIA Deletion in Glioblastomas. N Engl J Med 364:627–637

51. Lake A, Shield LA, Cordano P, et al (2009) Mutations of NFKBIA, encoding IκBα, are a recurrent finding in classical Hodgkin lymphoma but are not a unifying feature of non-EBV-associated cases. International Journal of Cancer 125:1334–1342

52. Jungnickel B, Staratschek-Jox A, Bräuninger A, Spieker T, Wolf J, Diehl V, Hansmann M-L, Rajewsky K, Küppers R (2000) Clonal Deleterious Mutations in the Iκbα Gene in the Malignant Cells in Hodgkin's Lymphoma. J Exp Med 191:395–402

53. Cabannes E, Khan G, Aillet F, Jarrett RF, Hay RT (1999) Mutations in the IkBa gene in Hodgkin's disease suggest a tumour suppressor role for IκBα. Oncogene 18:3063–3070

54. Cao Y, Bonizzi G, Seagroves TN, Greten FR, Johnson R, Schmidt EV, Karin M IKK␣ Provides an Essential Link between RANK Signaling and Cyclin D1 Expression during Mammary Gland Development. 13

55. Sau A, Lau R, Cabrita MA, Nolan E, Crooks PA, Visvader JE, Pratt MAC (2016) Persistent Activation of NF-κB in BRCA1-Deficient Mammary Progenitors Drives Aberrant Proliferation and Accumulation of DNA Damage. Cell Stem Cell 19:52–65

56. Chu Z-L, McKinsey TA, Liu L, Gentry JJ, Malim MH, Ballard DW (1997) Suppression of tumor necrosis factor-induced cell death by inhibitor of apoptosis c-IAP2 is under NF-κB control. Proc Natl Acad Sci U S A 94:10057–10062

57. Deveraux QL, Roy N, Stennicke HR, Van Arsdale T, Zhou Q, Srinivasula SM, Alnemri ES, Salvesen GS, Reed JC (1998) IAPs block apoptotic events induced by caspase-8 and cytochrome c by direct inhibition of distinct caspases. EMBO J 17:2215–2223

58. Ahmed KM, Li JJ (2008) NF-κB-mediated adaptive resistance to ionizing radiation. Free Radic Biol Med 44:1–13

59. Chuang S-E, Yeh P-Y, Lu Y-S, Lai G-M, Liao C-M, Gao M, Cheng A-L (2002) Basal levels and patterns of anticancer drug-induced activation of nuclear factor-κB (NF-κB), and its attenuation by tamoxifen, dexamethasone, and curcumin in carcinoma cells. Biochemical Pharmacology 63:1709–1716

60. Bentires-Alj M, Barbu V, Fillet M, Chariot A, Relic B, Jacobs N, Gielen J, Merville M-P, Bours V (2003) NF- κ B transcription factor induces drug resistance through MDR1 expression in cancer cells. Oncogene 22:90–97

61. Paul A, Edwards J, Pepper C, Mackay S (2018) Inhibitory-κB Kinase (IKK) α and Nuclear Factor-κB (NFκB)-Inducing Kinase (NIK) as Anti-Cancer Drug Targets. Cells. https://doi.org/10.3390/cells7100176

62. Godwin P, Baird AM, Heavey S, Barr MP, O'Byrne KJ, Gately K (2013) Targeting Nuclear Factor-Kappa B to Overcome Resistance to Chemotherapy. Front Oncol. https://doi.org/10.3389/fonc.2013.00120

63. Orlowski RZ, Baldwin AS (2002) NF-κB as a therapeutic target in cancer. Trends in Molecular Medicine 8:385–389

64. Matsumoto G, Namekawa J, Muta M, Nakamura T, Bando H, Tohyama K, Toi M, Umezawa K (2005) Targeting of Nuclear Factor κB Pathways by Dehydroxymethylepoxyquinomicin, a Novel Inhibitor of Breast Carcinomas: Antitumor and Antiangiogenic Potential In vivo. Clin Cancer Res 11:1287–1293

65. Bednarski BK, Baldwin AS, Kim HJ (2009) Addressing Reported Pro-Apoptotic Functions of NF-κB: Targeted Inhibition of Canonical NF-κB Enhances the Apoptotic Effects of Doxorubicin. PLoS One. https://doi.org/10.1371/journal.pone.0006992

66. Miraghazadeh B, Cook MC (2018) Nuclear Factor-kappaB in Autoimmunity: Man and Mouse. Front Immunol. https://doi.org/10.3389/fimmu.2018.00613

67. Hayden MS, West AP, Ghosh S (2006) NF-kappaB and the immune response. Oncogene 25:6758–6780

68. Aronica MA, Mora AL, Mitchell DB, Finn PW, Johnson JE, Sheller JR, Boothby MR (1999) Preferential Role for NF-κB/Rel Signaling in the Type 1 But Not Type 2 T Cell-Dependent Immune Response In Vivo. The Journal of Immunology 163:5116–5124

69. Hagemann T, Lawrence T, McNeish I, Charles KA, Kulbe H, Thompson RG, Robinson SC, Balkwill FR (2008) "Re-educating" tumor-associated macrophages by targeting NF-κB. J Exp Med 205:1261–1268

70. Shen J, Sun X, Pan B, Cao S, Cao J, Che D, Liu F, Zhang S, Yu Y (2018) IL-17 induces macrophages to M2-like phenotype via NF-κB. Cancer Manag Res 10:4217–4228

71. Street W Breast Cancer Facts & Figures 2017-2018. 44

72. Gutierrez C, Schiff R (2011) HER 2: Biology, Detection, and Clinical Implications. Arch Pathol Lab Med 135:55–62

73. Press MF, Cordon-Cardo C, Slamon DJ (1990) Expression of the HER-2/neu proto-oncogene in normal human adult and fetal tissues. Oncogene 5:953–962

74. Yarden Y, Sliwkowski MX (2001) Untangling the ErbB signalling network. Nat Rev Mol Cell Biol 2:127–137

75. Citri A, Yarden Y (2006) EGF–ERBB signalling: towards the systems level. Nat Rev Mol Cell Biol 7:505–516

76. Slamon DJ, Clark GM, Wong SG, Levin WJ, Ullrich A, McGuire WL (1987) Human breast cancer: correlation of relapse and survival with amplification of the HER-2/neu oncogene. Science 235:177–182

77. Wu Q, Li J, Zhu S, Wu J, Chen C, Liu Q, Wei W, Zhang Y, Sun S (2017) Breast cancer subtypes predict the preferential site of distant metastases: a SEER based study. Oncotarget 8:27990–27996

78. Arvold ND, Oh KS, Niemierko A, Taghian AG, Lin NU, Abi-Raad RF, Sreedhara M, Harris JR, Alexander BM (2012) Brain metastases after breast-conserving therapy and systemic therapy: incidence and characteristics by biologic subtype. Breast Cancer Res Treat 136:153–160

79. Cancer of the Breast (Female) - Cancer Stat Facts. In: SEER. https://seer.cancer.gov/statfacts/html/breast.html. Accessed 12 Oct 2019

80. Cortazar P, Zhang L, Untch M, et al (2014) Pathological complete response and long-term clinical benefit in breast cancer: the CTNeoBC pooled analysis. The Lancet 384:164–172

81. Tykerb (lapatinib ditosylate) FDA Approval History. In: Drugs.com. https://www.drugs.com/history/tykerb.html. Accessed 12 Oct 2019

82. Clynes RA, Towers TL, Presta LG, Ravetch JV (2000) Inhibitory Fc receptors modulate in vivo cytoxicity against tumor targets. Nat Med 6:443–446

83. Klapper LN, Waterman H, Sela M, Yarden Y (2000) Tumor-inhibitory Antibodies to HER-2/ErbB-2 May Act by Recruiting c-Cbl and Enhancing Ubiquitination of HER-2. Cancer Res 60:3384–3388

84. Yamashita-Kashima Y, Shu S, Yorozu K, Moriya Y, Harada N (2017) Mode of action of pertuzumab in combination with trastuzumab plus docetaxel therapy in a HER2-positive breast cancer xenograft model. Oncol Lett 14:4197–4205

85. Research C for DE and (2019) FDA approves ado-trastuzumab emtansine for early breast cancer. FDA

86. Barok M, Joensuu H, Isola J (2014) Trastuzumab emtansine: mechanisms of action and drug resistance. Breast Cancer Research 16:209

87. von Minckwitz G, Procter M, de Azambuja E, et al (2017) Adjuvant Pertuzumab and Trastuzumab in Early HER2-Positive Breast Cancer. New England Journal of Medicine 377:122–131

88. Swain SM, Baselga J, Kim S-B, et al (2015) Pertuzumab, Trastuzumab, and Docetaxel in HER2-Positive Metastatic Breast Cancer. New England Journal of Medicine 372:724–734

89. von Minckwitz G, Huang C-S, Mano MS, et al (2019) Trastuzumab Emtansine for Residual Invasive HER2-Positive Breast Cancer. New England Journal of Medicine 380:617–628

90. (2017) Breast Cancer - Metastatic - Types of Treatment. In: Cancer.Net. https://www.cancer.net/cancer-types/breast-cancer-metastatic/types-treatment. Accessed 12 Oct 2019

91. Xin Y, Guo WW, Huang Q, Zhang P, Zhang L, Jiang G, Tian Y (2016) Effects of lapatinib or trastuzumab, alone and in combination, in human epidermal growth factor receptor 2-positive breast cancer: a meta-analysis of randomized controlled trials. Cancer Med 5:3454–3463

92. Petrelli F, Ghidini M, Lonati V, Tomasello G, Borgonovo K, Ghilardi M, Cabiddu M, Barni S (2017) The efficacy of lapatinib and capecitabine in HER-2 positive breast cancer with brain metastases: A systematic review and pooled analysis. European Journal of Cancer 84:141–148

93. Kawamoto H, Minato N (2004) Myeloid cells. Int J Biochem Cell Biol 36:1374–1379

94. Weiskopf K, Schnorr PJ, Pang WW, Chao MP, Chhabra A, Seita J, Feng M, Weissman IL (2016) Myeloid cell origins, differentiation, and clinical implications. Microbiol Spectr. https://doi.org/10.1128/microbiolspec.MCHD-0031-2016

95. Charles A Janeway J, Travers P, Walport M, Shlomchik MJ (2001) The components of the immune system. Immunobiology: The Immune System in Health and Disease. 5th edition

96. Arandjelovic S, Ravichandran KS (2015) Phagocytosis of apoptotic cells in homeostasis. Nat Immunol 16:907–917

97. Chakrabarty S, Snyder JT, Shen J, Azmi H, Hu PQ, Chen Q, Ragheb JA (2011) Human CD14hi monocytes and myeloid dendritic cells provide a cell contact–

dependent costimulatory signal for early CD40 ligand expression. Blood 117:1585–1594

98. Merad M, Sathe P, Helft J, Miller J, Mortha A (2013) The Dendritic Cell Lineage: Ontogeny and Function of Dendritic Cells and Their Subsets in the Steady State and the Inflamed Setting. Annu Rev Immunol. https://doi.org/10.1146/annurev-immunol-020711-074950

99. Théry C, Amigorena S (2001) The cell biology of antigen presentation in dendritic cells. Current Opinion in Immunology 13:45–51

100. Hirayama D, Iida T, Nakase H (2017) The Phagocytic Function of Macrophage-Enforcing Innate Immunity and Tissue Homeostasis. Int J Mol Sci. https://doi.org/10.3390/ijms19010092

101. Mantovani A, Sozzani S, Locati M, Allavena P, Sica A (2002) Macrophage polarization: tumor-associated macrophages as a paradigm for polarized M2 mononuclear phagocytes. Trends Immunol 23:549–555

102. Biswas SK, Mantovani A (2010) Macrophage plasticity and interaction with lymphocyte subsets: cancer as a paradigm. Nature Immunology 11:889–896

103. Kodelja V, Müller C, Tenorio S, Schebesch C, Orfanos CE, Goerdt S (1997) Differences in angiogenic potential of classically vs alternatively activated macrophages. Immunobiology 197:478–493

104. Sun T, Yang Y, Luo X, Cheng Y, Zhang M, Wang K, Ge C (2014) Inhibition of tumor angiogenesis by interferon-γ by suppression of tumor-associated macrophage differentiation. Oncol Res 21:227–235

105. Jetten N, Verbruggen S, Gijbels MJ, Post MJ, De Winther MPJ, Donners MMPC (2014) Anti-inflammatory M2, but not pro-inflammatory M1 macrophages promote angiogenesis in vivo. Angiogenesis 17:109–118

106. Ostrand-Rosenberg S, Sinha P (2009) Myeloid-Derived Suppressor Cells: Linking Inflammation and Cancer. J Immunol 182:4499–4506

107. Hanson EM, Clements VK, Sinha P, Ilkovitch D, Ostrand-Rosenberg S (2009) Myeloid-Derived Suppressor Cells Down-Regulate L-Selectin Expression on CD4+ and CD8+ T Cells. J Immunol 183:937–944

108. Lindenberg JJ, Fehres CM, van Cruijsen H, Oosterhoff D, de Gruijl TD (2011) Cross-talk between tumor and myeloid cells: how to tip the balance in favor of antitumor immunity. Immunotherapy 3:77–96

109. Ricciardi A, Elia AR, Cappello P, et al (2008) Transcriptome of Hypoxic Immature Dendritic Cells: Modulation of Chemokine/Receptor Expression. Mol Cancer Res 6:175–185

110. Fricke I, Gabrilovich DI (2006) Dendritic cells and tumor microenvironment: a dangerous liaison. Immunol Invest 35:459–483

111. Stanley ER, Guilbert LJ, Tushinski RJ, Bartelmez SH (1983) CSF-1—A mononuclear phagocyte lineage-specific hemopoietic growth factor. Journal of Cellular Biochemistry 21:151–159

112. Aharinejad S, Paulus P, Sioud M, Hofmann M, Zins K, Schäfer R, Stanley ER, Abraham D (2004) Colony-Stimulating Factor-1 Blockade by Antisense Oligonucleotides and Small Interfering RNAs Suppresses Growth of Human Mammary Tumor Xenografts in Mice. Cancer Res 64:5378–5384

113. Brana I, Calles A, LoRusso PM, Yee LK, Puchalski TA, Seetharam S, Zhong B, de Boer CJ, Tabernero J, Calvo E (2015) Carlumab, an anti-C-C chemokine ligand 2 monoclonal antibody, in combination with four chemotherapy regimens for the treatment of patients with solid tumors: an open-label, multicenter phase 1b study. Targ Oncol 10:111–123

114. Gomez-Roca CA, Italiano A, Le Tourneau C, et al (2019) Phase I study of emactuzumab single agent or in combination with paclitaxel in patients with advanced/metastatic solid tumors reveals depletion of immunosuppressive M2-like macrophages. Ann Oncol 30:1381–1392

115. Edwards JP, Emens LA (2010) The multikinase inhibitor Sorafenib reverses the suppression of IL-12 and enhancement of IL-10 by PGE2 in murine macrophages. International Immunopharmacology 10:1220–1228

116. Georgoudaki A-M, Prokopec KE, Boura VF, et al (2016) Reprogramming Tumor-Associated Macrophages by Antibody Targeting Inhibits Cancer Progression and Metastasis. Cell Rep 15:2000–2011

117. Deng Y-R, Liu W-B, Lian Z-X, Li X, Hou X (2016) Sorafenib inhibits macrophage-mediated epithelial-mesenchymal transition in hepatocellular carcinoma. Oncotarget 7:38292–38305

118. Mach N, Gillessen S, Wilson SB, Sheehan C, Mihm M, Dranoff G (2000) Differences in Dendritic Cells Stimulated in Vivo by Tumors Engineered to Secrete Granulocyte-Macrophage Colony-stimulating Factor or Flt3-Ligand. Cancer Res 60:3239–3246

119. Lee J-H, Roh M-S, Lee Y-K, Kim M-K, Han J-Y, Park B-H, Trown P, Kirn DH, Hwang T-H (2010) Oncolytic and immunostimulatory efficacy of a targeted oncolytic poxvirus expressing human GM-CSF following intravenous administration in a rabbit tumor model. Cancer Gene Ther 17:73–79

120. Nemunaitis J (2005) Vaccines in cancer: GVAX, a GM-CSF gene vaccine. Expert Rev Vaccines 4:259–274

121. (2017) Intervention Dynamic Trial Listing Page. In: National Cancer Institute. https://www.cancer.gov/about-cancer/treatment/clinical-trials/intervention/gvax-pancreatic-cancer-vaccine. Accessed 14 Oct 2019

122. Cancer Immunotherapy | PROVENGE | Science Of Dendreon. https://www.dendreon.com/Our-Science#PROVENGEsipuleucelT. Accessed 14 Oct 2019

123. Fujio K, Watanabe M, Ueki H, Li S-A, Kinoshita R, Ochiai K, Futami J, Watanabe T, Nasu Y, Kumon H (2015) A vaccine strategy with multiple prostatic acid phosphatase-fused cytokines for prostate cancer treatment. Oncol Rep 33:1585–1592

124. Pipeline. Northwest Biotherapeutics

125. Patient education: Treatment of early HER2-positive breast cancer (Beyond the Basics) - UpToDate. https://www.uptodate.com/contents/treatment-of-early-her2-positive-breast-cancer-beyond-the-basics/print. Accessed 29 Oct 2019

126. Omission of Radiation in Patients With Her-2 Positive Breast Cancer - Full Text View - ClinicalTrials.gov. https://clinicaltrials.gov/ct2/show/NCT03460067. Accessed 29 Oct 2019

127. Holleczek B, Stegmaier C, Radosa JC, Solomayer E-F, Brenner H (2019) Risk of loco-regional recurrence and distant metastases of patients with invasive breast cancer up to ten years after diagnosis – results from a registry-based study from Germany. BMC Cancer 19:520

128. Desouky O, Ding N, Zhou G (2015) Targeted and non-targeted effects of ionizing radiation. Journal of Radiation Research and Applied Sciences 8:247–254

129. Baskar R, Dai J, Wenlong N, Yeo R, Yeoh K-W (2014) Biological response of cancer cells to radiation treatment. Front Mol Biosci. https://doi.org/10.3389/fmolb.2014.00024

130. Shen C, Oswald D, Phelps D, Cam H, Pelloski CE, Pang Q, Houghton PJ (2013) Regulation of FANCD2 by the mTOR pathway contributes to the resistance of cancer cells to DNA double strand breaks. Cancer Res 73:3393–3401

131. Wang Z, Huang Y, Zhang J (2014) Molecularly targeting the PI3K-Akt-mTOR pathway can sensitize cancer cells to radiotherapy and chemotherapy. Cell Mol Biol Lett 19:233–242

132. Tang G, Minemoto Y, Dibling B, Purcell NH, Li Z, Karin M, Lin A (2001) Inhibition of JNK activation through NF- κ B target genes. Nature 414:313–317

133. Baltimore D (2011) NF-κB is 25. Nat Immunol 12:683–685

134. Hoffmann A, Levchenko A, Scott ML, Baltimore D (2002) The IκB-NF-κB Signaling Module: Temporal Control and Selective Gene Activation. Science 298:1241–1245

135. (1999) Activators and target genes of Rel/NF-κB transcription factors. , Published online: 22 November 1999; | doi:101038/sj.onc1203239. https://doi.org/10.1038/sj.onc.1203239

136. Guo B, Fu S, Zhang J, Liu B, Li Z (2016) Targeting inflammasome/IL-1 pathways for cancer immunotherapy. Scientific Reports 6:srep36107

137. Hoesel B, Schmid JA (2013) The complexity of NF-κB signaling in inflammation and cancer. Mol Cancer 12:86

138. Kishore N, Sommers C, Mathialagan S, et al (2003) A Selective IKK-2 Inhibitor Blocks NF-κB-dependent Gene Expression in Interleukin-1β-stimulated Synovial Fibroblasts. J Biol Chem 278:32861–32871

139. Liu Q, Wu H, Chim SM, et al (2013) SC-514, a selective inhibitor of IKKβ attenuates RANKL-induced osteoclastogenesis and NF-κB activation. Biochemical Pharmacology 86:1775–1783

140. Cheong R, Bergmann A, Werner SL, Regal J, Hoffmann A, Levchenko A (2006) Transient IκB Kinase Activity Mediates Temporal NF-κB Dynamics in Response to a Wide Range of Tumor Necrosis Factor-α Doses. J Biol Chem 281:2945–2950

141. Krishnan RK, Nolte H, Sun T, Kaur H, Sreenivasan K, Looso M, Offermanns S, Krüger M, Swiercz JM (2015) Quantitative analysis of the TNF-α-induced phosphoproteome reveals AEG-1/MTDH/LYRIC as an IKKβ substrate. Nat Commun 6:6658

142. Lee REC, Walker SR, Savery K, Frank DA, Gaudet S (2014) Fold-change of nuclear NF-κB determines TNF-induced transcription in single cells. Mol Cell 53:867–879

143. Carpenter AE, Jones TR, Lamprecht MR, et al (2006) CellProfiler: image analysis software for identifying and quantifying cell phenotypes. Genome Biol 7:R100

144. Lamprecht MR, Sabatini DM, Carpenter AE (2007) CellProfiler: free, versatile software for automated biological image analysis. BioTechniques 42:71–75

145. Bray M-A, Vokes MS, Carpenter AE (2015) Using CellProfiler for Automatic Identification and Measurement of Biological Objects in Images. Curr Protoc Mol Biol 109:14.17.1-14.17.13

146. Lohman BK, Weber JN, Bolnick DI Evaluation of TagSeq, a reliable low-cost alternative for RNAseq. Molecular Ecology Resources 16:1315–1321

147. Meyer E, Aglyamova GV, Matz MV (2011) Profiling gene expression responses of coral larvae (Acropora millepora) to elevated temperature and settlement inducers using a novel RNA-Seq procedure. Molecular Ecology 20:3599–3616

148. Hannon lab FASTX Toolkit.

149. Langmead B, Salzberg SL (2012) Fast gapped-read alignment with Bowtie 2. Nature Methods 9:357–359

150. Love MI, Huber W, Anders S (2014) Moderated estimation of fold change and dispersion for RNA-seq data with DESeq2. Genome Biology 15:550

151. R Development Core Team (2011) R: A Language and Environment for Statistical Computing. Vienna, Austria : the R Foundation for Statistical Computing.

152. Rousseeuw PJ (1987) Silhouettes: A graphical aid to the interpretation and validation of cluster analysis. Journal of Computational and Applied Mathematics 20:53–65

153. Castoreno AB, Eggert US (2011) Small Molecule Probes of Cellular Pathways and Networks. ACS Chem Biol 6:86–94

154. Ewan K, Pajak B, Stubbs M, et al (2010) A useful approach to identify novel small-molecule inhibitors of Wnt-dependent transcription. Cancer Res 70:5963–5973

155. Kanters E, Pasparakis M, Gijbels MJJ, et al (2003) Inhibition of NF-κB activation in macrophages increases atherosclerosis in LDL receptor–deficient mice. J Clin Invest 112:1176–1185

156. Li Z-W, Chu W, Hu Y, Delhase M, Deerinck T, Ellisman M, Johnson R, Karin M (1999) The IKKβ Subunit of IκB Kinase (IKK) is Essential for Nuclear Factor κB Activation and Prevention of Apoptosis. Journal of Experimental Medicine 189:1839–1845

157. Burke JR, Pattoli MA, Gregor KR, et al (2003) BMS-345541 Is a Highly Selective Inhibitor of IκB Kinase That Binds at an Allosteric Site of the Enzyme and Blocks NF-κB-dependent Transcription in Mice. J Biol Chem 278:1450–1456

158. Yamamoto Y, Yin M-J, Lin K-M, Gaynor RB (1999) Sulindac Inhibits Activation of the NF-κB Pathway. J Biol Chem 274:27307–27314

159. Alberts B, Johnson A, Lewis J, Raff M, Roberts K, Walter P (2002) General Principles of Cell Communication.

160. Werner SL, Barken D, Hoffmann A (2005) Stimulus Specificity of Gene Expression Programs Determined by Temporal Control of IKK Activity. Science 309:1857–1861

161. Culig Z (2011) Cytokine disbalance in common human cancers. Biochimica et Biophysica Acta (BBA) - Molecular Cell Research 1813:308–314

162. Mateen S, Moin S, Shahzad S, Khan AQ (2017) Level of inflammatory cytokines in rheumatoid arthritis patients: Correlation with 25-hydroxy vitamin D and reactive oxygen species. PLOS ONE 12:e0178879

163. Ménard S, Pupa SM, Campiglio M, Tagliabue E (2003) Biologic and therapeutic role of HER2 in cancer. Oncogene 22:6570–6578

164. Zhang A, Shen G, Zhao T, Zhang G, Liu J, Song L, Wei W, Bing L, Wu Z, Wu Q (2010) Augmented inhibition of angiogenesis by combination of HER2 antibody chA21 and trastuzumab in human ovarian carcinoma xenograft. J Ovarian Res 3:20

165. Klos KS, Zhou X, Lee S, Zhang L, Yang W, Nagata Y, Yu D (2003) Combined trastuzumab and paclitaxel treatment better inhibits ErbB-2-mediated angiogenesis in breast carcinoma through a more effective inhibition of Akt than either treatment alone. Cancer 98:1377–1385

166. Jain RK (2013) Normalizing tumor microenvironment to treat cancer: bench to bedside to biomarkers. J Clin Oncol 31:2205–2218

167. Goel S, Wong AH-K, Jain RK (2012) Vascular Normalization as a Therapeutic Strategy for Malignant and Nonmalignant Disease. Cold Spring Harb Perspect Med. https://doi.org/10.1101/cshperspect.a006486

168. Ebos JML, Kerbel RS (2011) Antiangiogenic therapy: impact on invasion, disease progression, and metastasis. Nat Rev Clin Oncol 8:210–221

169. Gianni L, Romieu GH, Lichinitser M, et al (2013) AVEREL: a randomized phase III Trial evaluating bevacizumab in combination with docetaxel and trastuzumab as first-line therapy for HER2-positive locally recurrent/metastatic breast cancer. J Clin Oncol 31:1719–1725

170. Research C for DE and (2019) Avastin (bevacizumab) Information. FDA

171. Anonymous (2018) European Medicines Agency completes its review of Avastin used in breast cancer. In: European Medicines Agency. https://www.ema.europa.eu/en/news/european-medicines-agency-completes-its-review-avastin-used-breast-cancer. Accessed 17 Sep 2019

172. Bergers G, Hanahan D (2008) Modes of resistance to anti-angiogenic therapy. Nat Rev Cancer 8:592–603

173. Rivera LB, Bergers G (2015) Myeloid cell-driven angiogenesis and immune regulation in tumors. Trends Immunol 36:240–249

174. Schmid M, Varner JA (2007) Myeloid cell trafficking and tumor angiogenesis. Cancer Lett 250:1–8

175. Murdoch C, Muthana M, Coffelt SB, Lewis CE (2008) The role of myeloid cells in the promotion of tumour angiogenesis. Nature Reviews Cancer 8:618–631

176. Jain RK (2005) Normalization of Tumor Vasculature: An Emerging Concept in Antiangiogenic Therapy. Science 307:58–62

177. Murdoch C, Giannoudis A, Lewis CE (2004) Mechanisms regulating the recruitment of macrophages into hypoxic areas of tumors and other ischemic tissues. Blood 104:2224–2234

178. Naldini A, Morena E, Pucci A, Miglietta D, Riboldi E, Sozzani S, Carraro F (2012) Hypoxia affects dendritic cell survival: Role of the hypoxia-inducible factor-1α and lipopolysaccharide. Journal of Cellular Physiology 227:587–595

179. Huang Y, Yuan J, Righi E, et al (2012) Vascular normalizing doses of antiangiogenic treatment reprogram the immunosuppressive tumor microenvironment and enhance immunotherapy. PNAS 109:17561–17566

180. Rolny C, Mazzone M, Tugues S, et al (2011) HRG Inhibits Tumor Growth and Metastasis by Inducing Macrophage Polarization and Vessel Normalization through Downregulation of PlGF. Cancer Cell 19:31–44

181. Tian X, Wei F, Wang L, Yu W, Zhang N, Zhang X, Han Y, Yu J, Ren X (2017) Herceptin Enhances the Antitumor Effect of Natural Killer Cells on Breast Cancer Cells Expressing Human Epidermal Growth Factor Receptor-2. Front Immunol. https://doi.org/10.3389/fimmu.2017.01426

182. Arnould L, Gelly M, Penault-Llorca F, et al (2006) Trastuzumab-based treatment of HER2-positive breast cancer: an antibody-dependent cellular cytotoxicity mechanism? Br J Cancer 94:259–267

183. Jarrett AM, Bloom MJ, Godfrey W, Syed AK, Ekrut DA, Ehrlich LI, Yankeelov TE, Sorace AG Mathematical modelling of trastuzumab-induced immune response in an in vivo murine model of HER2+ breast cancer. Math Med Biol. https://doi.org/10.1093/imammb/dqy014

184. De Palma M, Lewis CE (2013) Macrophage Regulation of Tumor Responses to Anticancer Therapies. Cancer Cell 23:277–286

185. Qian B, Pollard JW (2010) Macrophage Diversity Enhances Tumor Progression and Metastasis. Cell 141:39–51

186. Movahedi K, Laoui D, Gysemans C, et al (2010) Different Tumor Microenvironments Contain Functionally Distinct Subsets of Macrophages Derived from Ly6C(high) Monocytes. Cancer Res 70:5728–5739

187. Vangestel C, Van de Wiele C, Van Damme N, Staelens S, Pauwels P, Reutelingsperger CPM, Peeters M (2011) (99)mTc-(CO)(3) His-annexin A5 micro-SPECT demonstrates increased cell death by irinotecan during the vascular normalization window caused by bevacizumab. J Nucl Med 52:1786–1794

188. Amici SA, Young NA, Narvaez-Miranda J, Jablonski KA, Arcos J, Rosas L, Papenfuss TL, Torrelles JB, Jarjour WN, Guerau-de-Arellano M (2018) CD38 Is Robustly Induced in Human Macrophages and Monocytes in Inflammatory Conditions. Front Immunol. https://doi.org/10.3389/fimmu.2018.01593

189. Martinez FO, Helming L, Milde R, et al (2013) Genetic programs expressed in resting and IL-4 alternatively activated mouse and human macrophages: similarities and differences. Blood 121:e57–e69

190. Huang Y, Goel S, Duda DG, Fukumura D, Jain RK (2013) Vascular Normalization as an Emerging Strategy to Enhance Cancer Immunotherapy. Cancer Res 73:2943–2948

191. Huang Y, Snuderl M, Jain RK (2011) Polarization of tumor-associated macrophages: A novel strategy for vascular normalization and anti-tumor immunity. Cancer Cell 19:1–2

192. Xuan W, Qu Q, Zheng B, Xiong S, Fan G-H (2015) The chemotaxis of M1 and M2 macrophages is regulated by different chemokines. J Leukoc Biol 97:61–69

193. Liu Y, Cai Y, Liu L, Wu Y, Xiong X (2018) Crucial biological functions of CCL7 in cancer. PeerJ. https://doi.org/10.7717/peerj.4928

194. Räihä MR, Puolakkainen PA (2018) Tumor-associated macrophages (TAMs) as biomarkers for gastric cancer: A review. Chronic Dis Transl Med 4:156–163

195. Brown JM, Recht L, Strober S (2017) The Promise of Targeting Macrophages in Cancer Therapy. Clinical Cancer Research 23:3241–3250

196. Campbell MJ, Tonlaar NY, Garwood ER, et al (2011) Proliferating macrophages associated with high grade, hormone receptor negative breast cancer and poor clinical outcome. Breast Cancer Res Treat 128:703–711

197. Feng Q, Chang W, Mao Y, et al (2019) Tumor-associated Macrophages as Prognostic and Predictive Biomarkers for Postoperative Adjuvant Chemotherapy in Patients with Stage II Colon Cancer. Clin Cancer Res 25:3896–3907

198. Shi Y, Fan X, Deng H, Brezski RJ, Rycyzyn M, Jordan RE, Strohl WR, Zou Q, Zhang N, An Z (2015) Trastuzumab Triggers Phagocytic Killing of High HER2 Cancer Cells In Vitro and In Vivo by Interaction with Fcγ Receptors on Macrophages. The Journal of Immunology 194:4379–4386

199. Jablonski KA, Amici SA, Webb LM, Ruiz-Rosado J de D, Popovich PG, Partida-Sanchez S, Guerau-de-Arellano M (2015) Novel Markers to Delineate Murine M1 and M2 Macrophages. PLoS One. https://doi.org/10.1371/journal.pone.0145342

200. Orecchioni M, Ghosheh Y, Pramod AB, Ley K (2019) Macrophage Polarization: Different Gene Signatures in M1(LPS+) vs. Classically and M2(LPS–) vs. Alternatively Activated Macrophages. Front Immunol. https://doi.org/10.3389/fimmu.2019.01084

201. Mignot F, Ajgal Z, Xu H, Geraud A, Chen JY, Mégnin-Chanet F, Kirova Y (2017) Concurrent administration of anti-HER2 therapy and radiotherapy: Systematic review. Radiotherapy and Oncology 124:190–199

202. Spector NL, Blackwell KL (2009) Understanding the Mechanisms Behind Trastuzumab Therapy for Human Epidermal Growth Factor Receptor 2–Positive Breast Cancer. JCO 27:5838–5847

203. Vaupel P, Kelleher DK, Höckel M (2001) Oxygen status of malignant tumors: pathogenesis of hypoxia and significance for tumor therapy. Semin Oncol 28:29–35

204. Liu Z, Semenza GL, Zhang H (2015) Hypoxia-inducible factor 1 and breast cancer metastasis. J Zhejiang Univ Sci B 16:32–43

205. Lundgren K, Holm C, Landberg G (2007) Hypoxia and breast cancer: prognostic and therapeutic implications. Cell Mol Life Sci 64:3233–3247

206. Diehn M, Cho RW, Lobo NA, et al (2009) Association of Reactive Oxygen Species Levels and Radioresistance in Cancer Stem Cells. Nature 458:780–783

207. Godet I, Shin YJ, Ju JA, Ye IC, Wang G, Gilkes DM (2019) Fate-mapping post-hypoxic tumor cells reveals a ROS-resistant phenotype that promotes metastasis. Nat Commun 10:1–18

208. Sorace AG, Syed AK, Barnes SL, Quarles CC, Sanchez V, Kang H, Yankeelov TE (2017) Quantitative [18F]-FMISO- PET imaging shows reduction of hypoxia following trastuzumab in a murine model of HER2+ breast cancer. Mol Imaging Biol 19:130–137

209. Tsoutsou PG, Belkacemi Y, Gligorov J, Kuten A, Boussen H, Bese N, Koukourakis MI, area (AROME) on behalf of the A of R and O in the M (2010) Optimal Sequence of Implied Modalities in the Adjuvant Setting of Breast Cancer Treatment: An Update on Issues To Consider. The Oncologist 15:1169–1178

210. Jakštys B, Ruzgys P, Tamošiūnas M, Šatkauskas S (2015) Different Cell Viability Assays Reveal Inconsistent Results After Bleomycin Electrotransfer In Vitro. J Membrane Biol 248:857–863

211. Menyhárt O, Harami-Papp H, Sukumar S, Schäfer R, Magnani L, de Barrios O, Győrffy B (2016) Guidelines for the selection of functional assays to evaluate the hallmarks of cancer. Biochimica et Biophysica Acta (BBA) - Reviews on Cancer 1866:300–319

212. Single A, Beetham H, Telford BJ, Guilford P, Chen A (2015) A Comparison of Real-Time and Endpoint Cell Viability Assays for Improved Synthetic Lethal Drug Validation. J Biomol Screen 20:1286–1293

213. Mátés L, Chuah MKL, Belay E, et al (2009) Molecular evolution of a novel hyperactive Sleeping Beauty transposase enables robust stable gene transfer in vertebrates. Nat Genet 41:753–761

214. Kowarz E, Löscher D, Marschalek R (2015) Optimized Sleeping Beauty transposons rapidly generate stable transgenic cell lines. Biotechnol J 10:647–653

215. Bliss CI (1956) The calculation of microbial assays. Bacteriol Rev 20:243–258

216. Jiang W, Chan CK, Weissman IL, Kim BYS, Hahn SM (2016) Immune Priming of the Tumor Microenvironment by Radiation. Trends in Cancer 2:638–645

217. Schaue D, Micewicz ED, Ratikan JA, Xie MW, Cheng G, McBride WH (2015) Radiation & Inflammation. Semin Radiat Oncol 25:4–10

Vita

Meghan Jean Bloom was raised in Shavertown, Pennsylvania. She completed her Bachelor of Science in Biomedical Engineering from the University of Virginia in Charlottesville, Virginia in May 2015. As an undergraduate researcher, she conducted metabolic research of infectious diseases. To pursue her passion in medical research, she enrolled in graduate school in the Department of Biomedical Engineering at the University of Texas at Austin in August 2015. For her doctoral studies, she was focused on characterizing inflammatory and immunological aspects of the tumor microenvironment after treatment to inform on anti-tumor mechanisms. The results of her work were presented at numerous conferences and resulted in several first and co-authored publications. She completed her Ph.D. in Biomedical Engineering in December 2019.

Email: meghanjbloom@gmail.com

This dissertation was typed by Meghan Jean Bloom